

# **Multi-Scale Modelling of Electrode-Electrolyte Interface: A Case Study on the Electrochemical Carboxylation of Benzyl Chloride**

Zur Erlangung des akademischen Grades eines

**DOKTORS DER NATURWISSENSCHAFTEN**

(Dr. rer. nat.)

von der KIT-Facultät für Chemie und Biowissenschaften  
des Karlsruher Instituts für Technologie (KIT)

genehmigte

**DISSERTATION**

von

Aleksandr Kramarenko

1. Referent: Prof. Dr. Felix Studt

2. Referent: PD Sebastian Höfener

Tag der mündlichen Prüfung: 07.02.2025



## Table of contents

|  |    |
|--|----|
| Abstract.....  | 5  |
| Zusammenfassung.....   | 7  |
| 1. Introduction .....  | 9  |
| 1.1 Motivation.....  | 9  |
| 1.2 CO <sub>2</sub> capture.....   | 10 |
| 1.3 Electrochemical approach.....  | 12 |
| 1.4 CO <sub>2</sub> fixation by Benzyl Halides.....  | 14 |
| 1.5 Electrode/Solution Interface and Heterogeneous Electron Transfer .....   | 16 |
| 1.6 Scope of this Thesis .....   | 18 |
| 2. Computational methods.....  | 20 |
| 2.1 Electronic Structure Methods .....   | 20 |
| 2.2 Cyclic Voltammetry Simulation .....  | 22 |
| 2.2.1 Finite Difference Method .....   | 22 |
| 2.2.2 Finite Elements Method .....   | 23 |
| 2.3 Thermodynamics.....  | 25 |
| 2.4 Kinetics .....   | 25 |
| 2.5 Computational Details for this Thesis.....   | 28 |
| 3. Ferrocene/Ferrocenium Reference for Cyclic Voltammetry Simulation .....   | 30 |
| 3.1 Benchmark Calculations of Absolute reduction potential of Fc <sup>0</sup> /Fc <sup>+</sup> Electrode.....                                | 30 |
| 3.2 Redox Potentials of Organic Molecules in Non-aqueous solvents.....   | 36 |
| 3.3 Electron Transfer Kinetics on Inert Glassy Carbon Electrode Surface .....  | 40 |
| 3.4 Summary and Conclusion .....   | 46 |
| 4. Dissociative Electron Transfer Kinetics in Benzyl Halides Electrocboxylation.....   | 48 |
| 4.1 Electrochemical reduction of Benzyl Halides.....   | 48 |
| 4.2 Cyclic voltammetry simulation of Benzyl Chloride Electrocboxylation.....   | 59 |
| 4.4 Summary and Conclusion .....   | 62 |
| 5. Surface Charging Effect on Outer-Sphere Electron Transfer: A Strong Dependence on Supporting Electrolyte Concentration.....               | 64 |
| 5.1 Model of Electric Double Layer Formation and Electron Transfer Kinetics simulation .<br>.....  | 64 |
| 5.2 Electrode surface charge and Potential of Zero Charge.....   | 68 |
| 5.3 Supporting Electrolyte Influence on the Thermodynamics of Fc <sup>0</sup> /Fc <sup>+</sup> Oxidation on the Glassy Carbon Electrode..... | 74 |

|     |  |    |
|-----|--|----|
| 5.4 | Supporting Electrolyte Influence on the Electron Transfer Kinetics of $\text{Fc}^0/\text{Fc}^+$ Oxidation Process on the Glassy Carbon Electrode ..... | 76 |
| 5.5 | Supporting Electrolyte Influence to the Electron Transfer in the Reference Reactions on the Glassy Carbon Electrode.....                               | 83 |
| 5.6 | Summary and Conclusion .....   | 86 |
| 6.  | Outlook .....  | 88 |
| A   | Complete List of Publications .....  | 90 |
| B   | Publication Associated with the Thesis .....   | 91 |
| C   | List of Conferences Associated with the Thesis.....  | 92 |
| D   | Abbreviations.....   | 93 |
| E   | Acknowledgements .....   | 94 |
| F   | Eidesstattliche Versicherung .....   | 95 |
|     | Bibliography .....   | 96 |

## Abstract

This study investigates the complex mechanisms underlying the heterogeneous electron transfer in electrode-solution interface, with the main goal of advancing electrochemical modelling and the accurate prediction of electron transfer kinetics. The research is focused on the three key objectives: establishing a robust reference model for electron transfer based on the  $\text{Fc}^0/\text{Fc}^+$  system that is adaptable across diverse solvents and electrochemical environments; developing a density functional theory (DFT)-based kinetic model that minimizes reliance on experimental data through cyclic voltammetry (CV) simulations; and examining how supporting electrolytes influence electron transfer kinetics and thermodynamics, particularly with regard to solvent interactions.

Our study begins with the detailed examination of the electrode potentials, standard equilibrium potentials, and reaction kinetics in the ferrocene/ferrocenium ( $\text{Fc}^0/\text{Fc}^+$ ) redox system. Analysis of various DFT functionals revealed that unrestricted Kohn-Sham (UKS) calculations often underestimate ionization energies, especially in functionals with high Hartree-Fock exchange. A refinement with restricted open-shell Kohn-Sham (ROKS) adjustments improved these predictions, aligning calculated ionization energies more closely with experimental results, especially using PBE and M06 functionals. The M06 functional emerged as particularly effective for the equilibrium potentials predictions and activation energy calculations via the Marcus-Hush model, highlighting its accuracy and potential for broader electrochemical applications.

Further, in Chapter 4 we utilize our approach for calculating energetics and kinetic barriers in electron transfer, applied specifically to the electrochemical carboxylation of benzyl chloride ( $\text{BnCl}$ ) in acetonitrile ( $\text{MeCN}$ ). Built upon the computational hydrogen electrode (CHE) model approximation, this approach uses the  $\text{Fc}^0/\text{Fc}^+$  reference couple as a standard for consistent comparative analysis. The application of Marcus theory for determining electron transfer barriers at the electrode's double layer (EDL) provided insights into the mechanisms of electrochemical transformations. The model showed strong alignment with experimental results, demonstrating its validity and potential for adaptation to other electrochemical processes. Suggested improvements for this approach include incorporating dynamic solvent effects and accounting for electrode-molecule interactions, which could further refine the model's accuracy.

In exploring the influence of solvents and supporting electrolytes, Chapter 5 utilizes solvation models, the Marcus-Hush model and our modified model to assess how non-aqueous

solvents and variations in electrolyte concentration impact electron transfer thermodynamics and kinetics, particularly for the  $\text{Fc}^0/\text{Fc}^+$  redox couple. The computational  $\text{Fc}^0/\text{Fc}^+$  electrode (CFE) served as a reference point, comparable to the computational hydrogen electrode, and demonstrated strong agreement with experimental data, underscoring its effectiveness in predicting current peaks, half-wave potential shifts and enhancing understanding of electrochemical processes under varied conditions.

Our research proposes that the potential of zero charge (PZC) could serve as a benchmark for optimizing electrode material selection, offering new possibilities for understanding reaction kinetics and selectivity. Future studies are encouraged to extend this model to include detailed electrode surface characteristics, such as atomic structure and electronic properties, as well as to explore coupled proton-electron transfers, broadening its applications in electrocatalysis and energy storage. Altogether, this study provides a comprehensive framework for advancing electrochemical transformation models and offers tools and insights that support the development of next-generation materials and processes for sustainable chemistry and energy conversion applications.

## Zusammenfassung

Diese Studie untersucht die komplexen Mechanismen, die dem heterogenen Elektronentransfer in der Elektroden-Lösungs-Grenzfläche zugrunde liegen, mit dem Hauptziel, die elektrochemische Modellierung und genaue Vorhersage der Elektronentransferkinetik voranzutreiben. Die Forschung konzentriert sich auf die drei Hauptziele: Etablierung eines robusten Referenzmodells für den Elektronentransfer auf der Grundlage des  $\text{Fc}^0/\text{Fc}^+$ -Systems, das an verschiedene Lösungsmittel und elektrochemische Umgebungen angepasst werden kann; Entwicklung eines auf Dichtefunktionaltheorie (DFT) basierenden kinetischen Modells, das die Abhängigkeit von experimentellen Daten durch zyklische Voltammetrie (CV) -Simulationen minimiert; und Untersuchen, wie unterstützende Elektrolyte die Elektronentransferkinetik und -Thermodynamik beeinflussen, insbesondere im Hinblick auf Lösungsmittelwechselwirkungen.

Unsere Studie beginnt mit der detaillierten Untersuchung der Elektrodenpotentiale, Standardgleichgewichtspotentiale und Reaktionskinetik im Ferrocen / Ferrocenium ( $\text{Fc}^0/\text{Fc}^+$ ) -Redoxsystem. Die Analyse verschiedener DFT-Funktionale ergab, dass uneingeschränkte Kohn-Sham (UKS) -Berechnungen Ionisationsenergien häufig unterschätzen, insbesondere bei Funktionalen mit hohem Hartree-Fock-Austausch. Eine Verfeinerung mit eingeschränkten Open-Shell-Kohn-Sham-Anpassungen (ROKS) verbesserte diese Vorhersagen und passte die berechneten Ionisationsenergien enger an die experimentellen Ergebnisse an, insbesondere unter Verwendung von PBE- und M06-Funktionalen. Das M06-Funktional erwies sich als besonders effektiv für die Vorhersage von Gleichgewichtspotentialen und Aktivierungsenergieberechnungen über das Marcus-Hush-Modell, was seine Genauigkeit und sein Potenzial für breitere elektrochemische Anwendungen unterstreicht.

Darüber hinaus verwenden wir in Kapitel 4 unseren Ansatz zur Berechnung energetischer und kinetischer Barrieren beim Elektronentransfer, der speziell auf die elektrochemische Carboxylierung von Benzylchlorid ( $\text{BnCl}$ ) in Acetonitril ( $\text{MeCN}$ ) angewendet wird. Aufbauend auf der rechnergestützten Näherung des Wasserstoffelektrodenmodells (CHE) verwendet dieser Ansatz das  $\text{Fc}^0/\text{Fc}^+$ -Referenzpaar als Standard für konsistente Vergleichsanalysen. Die Anwendung der Marcus-Theorie zur Bestimmung von Elektronentransportbarrieren an der Doppelschicht (EDL) der Elektrode lieferte Einblicke in die Mechanismen elektrochemischer Umwandlungen. Das Modell zeigte eine starke Übereinstimmung mit experimentellen Ergebnissen und demonstrierte seine Gültigkeit und sein Potenzial für die Anpassung an andere elektrochemische Prozesse.

Verbesserungsvorschläge für diesen Ansatz umfassen die Einbeziehung dynamischer Lösungsmittelleffekte und die Berücksichtigung von Elektroden-Molekül-Wechselwirkungen, die die Genauigkeit des Modells weiter verfeinern könnten.

Bei der Untersuchung des Einflusses von Lösungsmitteln und unterstützenden Elektrolyten verwendet Kapitel 5 Solvatationsmodelle, das Marcus-Hush-Modell und unser modifiziertes Modell, um zu bewerten, wie sich nichtwässrige Lösungsmittel und Schwankungen der Elektrolytkonzentration auf die Thermodynamik und Kinetik des Elektronentransfers auswirken, insbesondere für das  $\text{Fc}^0/\text{Fc}^+$ -Redoxpaar. Die rechnergestützte  $\text{Fc}^0/\text{Fc}^+$ -Elektrode (CFE) diente als Referenzpunkt, vergleichbar mit der rechnergestützten Wasserstoffelektrode, und zeigte eine starke Übereinstimmung mit experimentellen Daten, was ihre Wirksamkeit bei der Vorhersage von Stromspitzen, Halbwellenpotentialverschiebungen und der Verbesserung des Verständnisses elektrochemischer Prozesse unter verschiedenen Bedingungen unterstreicht.

Unsere Forschung legt nahe, dass das Potenzial der Nullladung (PZC) als Maßstab für die Optimierung der Auswahl des Elektrodenmaterials dienen könnte und neue Möglichkeiten zum Verständnis der Reaktionskinetik und Selektivität bietet. Zukünftige Studien werden ermutigt, dieses Modell um detaillierte Elektrodenoberflächeneigenschaften wie Atomstruktur und elektronische Eigenschaften zu erweitern sowie gekoppelte Protonen-Elektronen-Transfers zu untersuchen und seine Anwendungen in der Elektrokatalyse und Energiespeicherung auszuweiten. Insgesamt bietet diese Studie einen umfassenden Rahmen für die Weiterentwicklung elektrochemischer Transformationsmodelle und bietet Werkzeuge und Erkenntnisse, die die Entwicklung von Materialien und Prozessen der nächsten Generation für nachhaltige Chemie- und Energieumwandlungsanwendungen unterstützen.



## 1. Introduction

### 1.1 Motivation

The steady increase in anthropogenic carbon dioxide (CO<sub>2</sub>) emissions is a big problem for the world and despite the numerous climate change mitigation efforts in recent years, carbon dioxide emissions rose at an average rate of 2.6% per year from 2000 to 2014, compared to 1.72% per year from 1970 to 2000.<sup>1</sup> Specifically, emissions grew from about 31.9 to 35.5 Gt of CO<sub>2</sub> per year between 2010 and 2014, averaging an increase of 2.75% per year (Figure 1).<sup>2</sup> Apart from two small declines from 2008 to 2009 and 2019 to 2020, every year in this century has experienced a year-on-year rise in anthropogenic CO<sub>2</sub> emissions.<sup>1,3,4</sup>

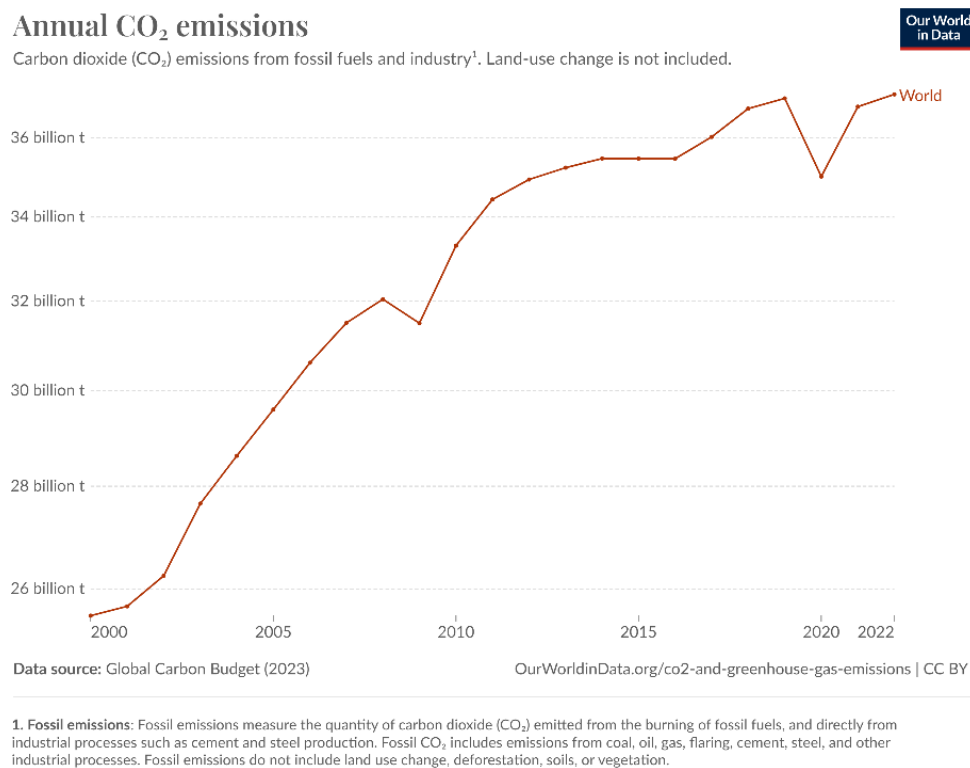


**Figure 1.** Annual carbon dioxide emissions from all types of sources in the world for the past 24 years. Reproduced from ref. 2. Available under a CC-BY 4.0 license. Copyright 2024 Ritchie, H.; Rosado, P.; Roser, M.

Future mitigation pathways are often discussed using the concepts of enhancement of natural carbon sinks, and the development of technologies for CO<sub>2</sub> capture, storage, and utilization. Carbon dioxide utilization refers to the process of converting captured CO<sub>2</sub> into valuable products, reducing carbon dioxide presence in the atmosphere and simultaneously creating economic opportunities. This approach not only mitigates the environmental impact of CO<sub>2</sub> but also adds value to what is often considered as a waste. The potential applications

of CO<sub>2</sub> utilization are diverse, ranging from the production of chemicals, fuels, and materials to its use in biological processes and enhanced oil recovery.<sup>1,3,5-8</sup> One of the primary trajectory for CO<sub>2</sub> utilization is its electrocatalytic conversion into valuable chemical derivatives.<sup>6,9-17</sup> This approach represents a promising technological frontier for sustainable and environmentally friendly solutions to reduce greenhouse gas emissions. By converting CO<sub>2</sub> into valuable products using renewable energy, this process not only tackles climate change but also promotes the development of the closed carbon-cycle economy. Ongoing research and innovation in this field are crucial for overcoming the current challenges and realizing full potential of carbon-efficient cycle.

## **1.2 CO<sub>2</sub> capture**

Capture and separation of CO<sub>2</sub> can be performed through various techniques. However, existing technologies still meet many challenges in capacity, stability and toxicity of the utilized reagents including the total efficiency of these processes. Typical procedures of carbon dioxide capture and separation include absorption, adsorption, electrochemical CO<sub>2</sub> fixation, membrane separation, and cryogenic distillation (Figure 2).

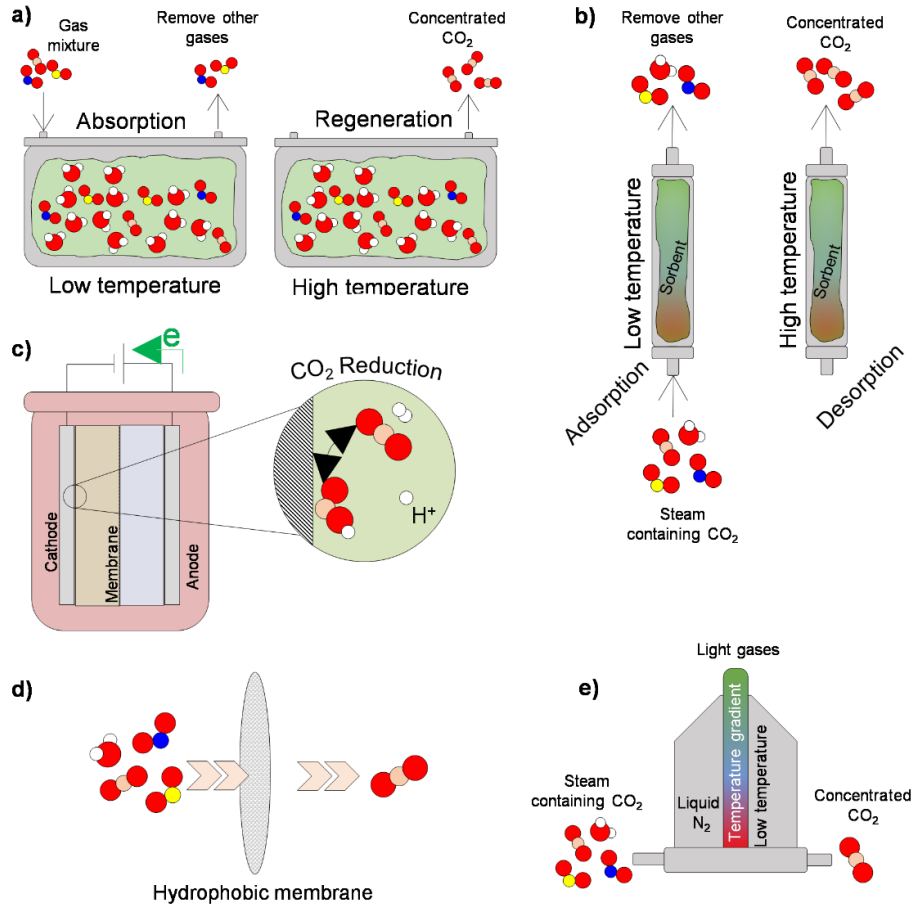
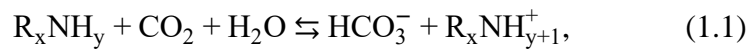
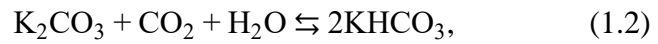


**Figure 2.** Schematic representation of the typical carbon dioxide capture technologies: a) absorption, b) adsorption, c) electrochemical capture, d) membrane-based separation, e) cryogenic distillation.

The absorption process involves usage of amine-substituted organic compounds or electrolyte solutions in aqueous or organic solvents (Figure 2a).<sup>18,19</sup>



where  $x = \{1, 2, 3\}$  and  $y = \{0, 1, 2\}$ .



The usage of amines or carbonates increases solubility of  $CO_2$  in the liquid sorbents and at the same time makes their regeneration more complicated demanding lower pressure and higher temperature. Moreover, one of the challenges in these procedures is the production of harmful side products such as nitramines and nitrosamines.<sup>19</sup> Additional obstacles are coming from the parallel absorption of accompanying gases such as  $SO_x$  and  $N_xO_y$  which are common products in many industrial processes. They decrease selectivity of the solvents towards  $CO_2$ , reducing the overall efficiency of the process. For aqueous absorbents, the strong interaction

between CO<sub>2</sub> and the solution, raises the energy costs for the regeneration process. Adding a catalyst to an absorption column increases the reaction rate, which in turn allows for a reduction in the size of the column and the solvent flow rate. This has a great impact on the industrial application of the process.<sup>20–23</sup>

The capture of carbon dioxide<sup>18,24–26</sup> by solid sorbents<sup>27–29</sup> has become a sustainable strategy to manage anthropogenic CO<sub>2</sub> emission. The easiest way to capture and store CO<sub>2</sub> by solid substances is to use cheap and wide-spread minerals<sup>27,28,30–33</sup> or specifically designed metal-organic frameworks (MOFs)<sup>34–39</sup> (Figure 2b). A simple example of this process is CO<sub>2</sub> fixation through the reaction of carbon dioxide with calcium or magnesium in rocks, forming stable carbonates:



This process is the most efficient technique due to the wide distribution of these adsorbents in the nature. Moreover, many material researchers and engineers are working to develop new materials with higher selectivity and CO<sub>2</sub> capacity, combining with energy efficient and yield efficient setups. Overall, solid-state adsorption techniques are proposed to be a superior alternative to their liquid-phase counterparts.

Membrane separation (Figure 2d) is widely employed compared to other methods due to its simplicity, ease of implementation, energy efficiency, and cost-effectiveness.<sup>40,41</sup> It is also commonly used as a practical approach for separating light components from the atmosphere. In such processes, the membrane plays a crucial role in the separation mechanism. Membranes can be made from a single polymer<sup>42</sup>, composite polymers<sup>43</sup>, ceramics<sup>44,45</sup>, carbon<sup>46</sup>, metal-based minerals<sup>47</sup>, or metal-organic framework membranes<sup>48</sup>, all of which are typically stacked on mechanical supports.

Cryogenic distillation (Figure 2e) relies on the differences in boiling points of gas components under high pressure (100–200 atm) and low temperatures ( $\approx -195$  °C) to achieve CO<sub>2</sub> condensation.<sup>49,50</sup> This allows CO<sub>2</sub> to be separated from other lighter gases. However, the efficiency of this method is debatable, and it requires further refinement and development.

### 1.3 Electrochemical approach

Electrochemical conversion (Figure 2d) uses electrical energy to reduce or capture CO<sub>2</sub> into various useful products. This process employs electrocatalysts that aid in the transfer of electrons to electrochemically active molecules, transforming them into hydrocarbons,

alcohols, and other compounds.<sup>6,9–17,51,52</sup> This technology has significant potential for sustainable energy production, as it can be powered by renewable energy sources like solar or wind power (Figure 3).<sup>53–56</sup>

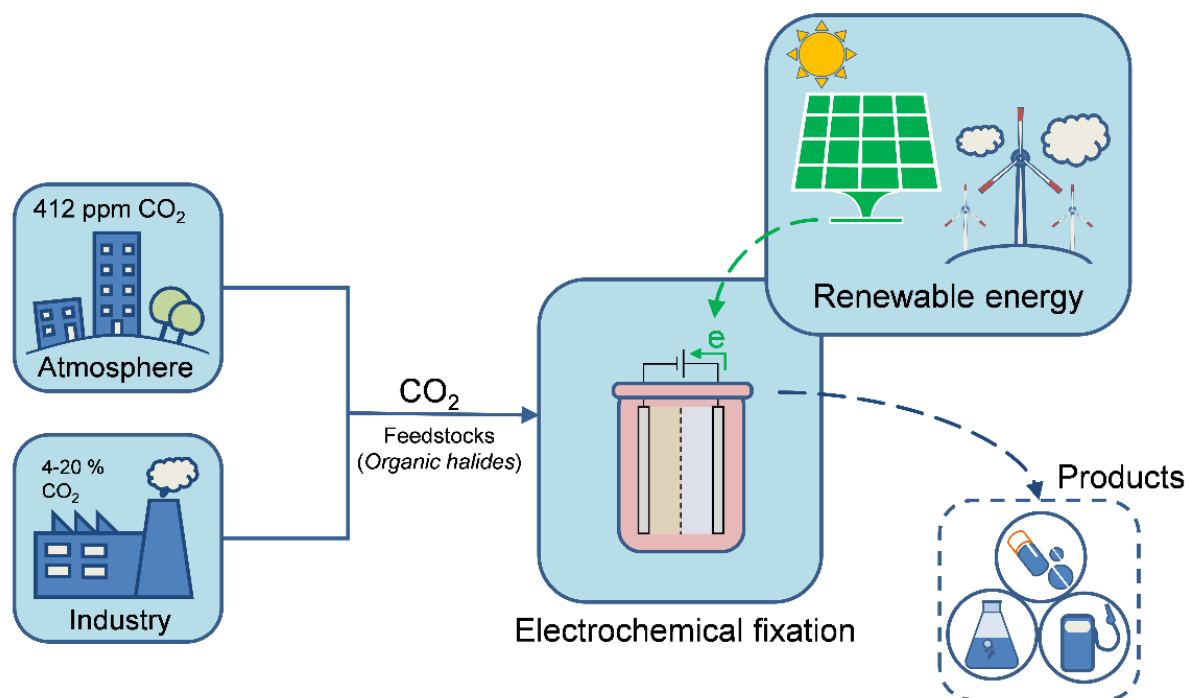
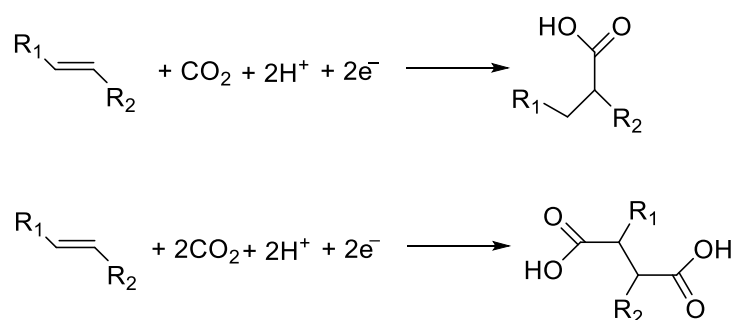


**Figure 3.** Schematic representation of green-powered electrochemical conversion of atmospheric and industrially produced CO<sub>2</sub> by fixation on organic halides for fuel, polymers and drugs production.

The electrocatalytic conversion process takes place in an electrochemical cell, which typically consists of two main components: anode and cathode, separated by an electrolyte. The core of this technology is the electrocatalyst, which is usually placed on the cathode. Commonly researched materials include metals like copper, silver, and gold, as well as various alloys and metal-organic frameworks.<sup>9,12,57–62</sup> These catalysts play a crucial role in lowering the energy barrier for the electron transfer.<sup>62–64</sup> The electrochemical cell is designed to optimize the contact between the electrocatalyst, electroactive species, and the electrolyte. The anode, is typically made of materials such as platinum or iridium, facilitating the oxidation reaction necessary to balance the reduction process occurring at the cathode. The efficiency and selectivity of CO<sub>2</sub> capture are influenced by factors such as applied electrode potential, current density, and electrolyte composition. Careful control of these parameters is essential to maximize conversion efficiency and direct the reaction pathway towards the desired products.

The use of carbon dioxide as an elementary chemical brick is a logical strategy to get economic benefit from its capture. However, high thermodynamic stability of the CO<sub>2</sub>

molecule ( $\Delta G_f^0 = -396 \frac{\text{kJ}}{\text{mol}}$ )<sup>52</sup> demands application of high temperature and pressure, or very negative applied potentials in order to activate  $\text{CO}_2$ .<sup>65,66</sup> Therefore, the optimal approach for sustainable mitigation of the  $\text{CO}_2$  problem is the  $\text{CO}_2$  fixation by organic chemicals with a lower activation barrier, followed by the production of carboxylic acids. The advantage of this approach is that it needs only a couple of electrons per  $\text{CO}_2$  molecule with formation of C-C bond (Scheme 1).



**Scheme 1.** Schematic representation of electrochemical  $\text{CO}_2$  fixation by olefins in aqueous solution producing organic acids.

Overall, electrochemical fixation of  $\text{CO}_2$  is an efficient approach to activate thermodynamically stable  $\text{CO}_2$  under relatively mild and safe conditions. However, this technology still meets many challenges, such as the choice of reactor setup<sup>67–69</sup>, electrode type<sup>58,70–72</sup> and reaction pathway<sup>63,73–75</sup>, which not only affect the cost of implementation, but also control operation characteristics.

#### 1.4 $\text{CO}_2$ fixation by Benzyl Halides

Besides the direct  $\text{CO}_2$  electroreduction to single- and multi-carbon small molecules,  $\text{CO}_2$  can be electrochemically coupled with various precursors (alkynes<sup>76–81</sup>, olefins<sup>82–84</sup> etc.) to produce numerous carboxylic acids.<sup>52,85–90</sup> The reactivity and product selectivity of electrocarboxylation (EC) are highly dependent on the cathodic behavior, which involves a series of electron transfers and chemical reactions (Figure 4). Therefore, understanding the cathodic reaction mechanisms is essential for optimizing reaction performance and product distribution.

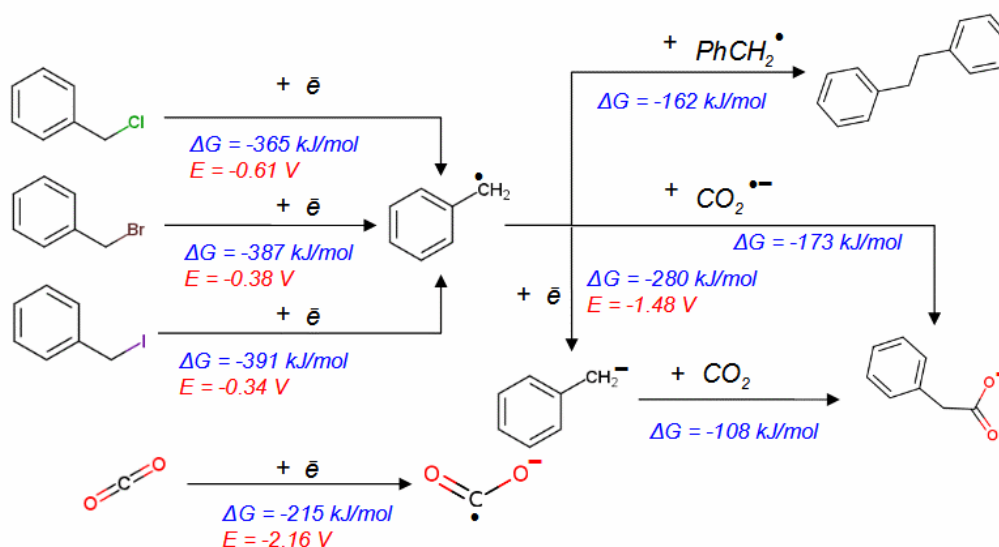


**Figure 4.** Possible pathway of benzyl halides electrochemical carboxylation and thermodynamic effects of elementary steps. Reduction potentials are referenced to the saturated calomel electrode (SCE) 4.422 V. Reproduced from ref. 91. Available under a CC-BY 4.0 license. Copyright 2024 A.S. Kramarenko, I. Yu. Chernyshov and E. A. Pidko.

The EC of organic halides (R–X) catches the eye as an environmentally friendly method for synthesizing nonsteroidal anti-inflammatory drugs like ibuprofen<sup>92</sup>, as well as key precursor for many industrial processes.<sup>52,93–95</sup> It was shown that EC of organohalides with different cathode materials<sup>52,58,93,96–98</sup> in undivided cells with sacrificial Mg or Al anodes generally yields the corresponding carboxylic acids as magnesium or aluminum salts, with moderate or high efficiency.<sup>58,98–103</sup> Although the formation of these salts simplifies the work-up procedure, it negatively impacts atom economy due to anode consumption. Additionally, the formation of insoluble products during EC reactions causes electrode passivation, leading to significant current fluctuations (potentiostatic electrolysis)<sup>104</sup> or increased cell voltage (constant current electrolysis), and hindering reaction yield.<sup>105</sup> Using non-sacrificial anodes with alternative anodic reactions could potentially overcome these issues. While divided cells with non-sacrificial anodes have been reported for EC of various organic substrates<sup>106–108</sup>, attempts with halides have generally been unsuccessful. Despite high yields from EC reactions of organic halides with Mg or Al anodes, the exact formation mechanism remains unclear.

Previous experimental studies propose two possible mechanisms of electron transfer (Figure 5).

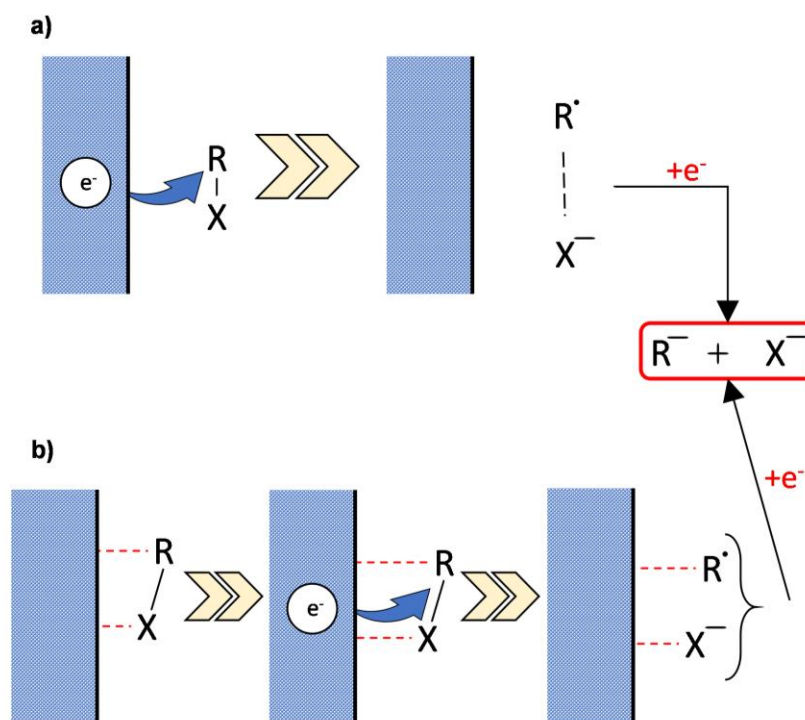


**Figure 5.** Two possible schemes of electrochemical reduction mechanism of organic halides (RX) on a) electrochemically inert electrodes such as glassy carbon (GC), or b) electrocatalytic electrodes such as Ag, Cu, Au etc.

In the first case (Figure 5a), there is no specific interaction between electrode and electroactive specie (e.g. Glassy carbon electrode), therefore the electron transfer happens through the tunneling from a state in the electrode near the Fermi level to the electronic state in the reduced molecule.<sup>109–112</sup> The second mechanism (Figure 5b) assumes a direct interaction of benzyl halides on the electrode surface. However, recent computational study showed that this mechanism is hindered by the tight EDL formation on the electrode surface.<sup>91</sup> Therefore, in this thesis, we focus on the first mechanism (Figure 5a) which we will discuss in details in Chapter 5.

## 1.5 Electrode/Solution Interface and Heterogeneous Electron Transfer

Previously, we analyzed chemical and electrochemical methods and technologies for  $CO_2$  conversion and established that the electrochemical approach is a powerful tool for the production of carboxylic acids. In this section we will discuss the electrode-electrolyte interface, the formation of EDL and its influence on the electron transfer.

Electron transfer (ET) usually occurs between the electrode and electroactive agents in the solution when the electrode's applied potential ( $E$ ), which is equal to the electrochemical



potential of the electrons in the electrode, reaches the equilibrium potential ( $E^0$ ) of the solution species.<sup>113,114</sup> The ET process processes modulate charges at the electrode surface and in the meantime, there is accumulation of solution ions near the electrode due to the electrostatic interaction, forming an EDL, which is featured by the gradient distributions of the electrostatic potential and the concentration of ions (Figure 6).

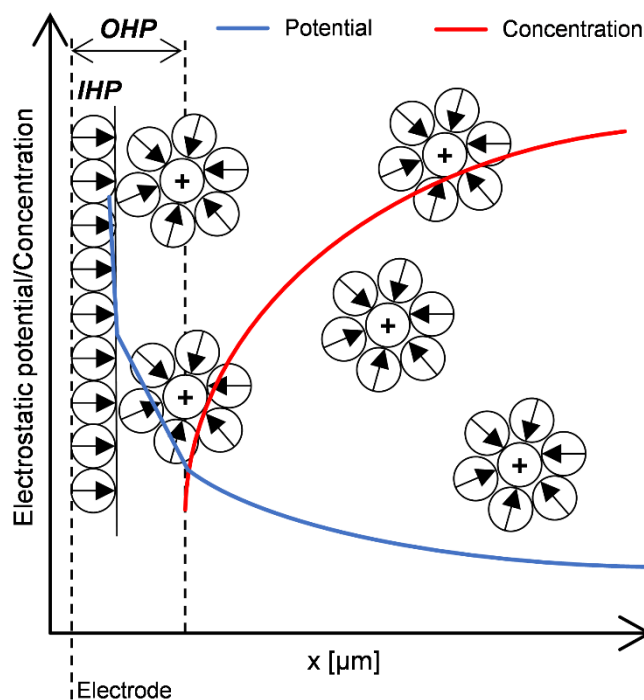


**Figure 6.** A schematic diagram of the structure of an electrode/electrolyte interface. The blue and red solid lines illustrate the distribution of the electrostatic potential and the concentration of the reactant respectively. Arrows denote the dipole moment of the solvent molecules adsorbed on the electrode surface and in solvation atmosphere of the ions. The outer-Helmholtz plane (OHP) denote the distance of the closest approach for the solvated ions. The inner-Helmholtz plane shows the solvation shell of the electrode.

The EDL can be divided into a compact part and a diffuse part with the boundaries at the outer-Helmholtz plane (OHP), which is the approximated distance of the closest approach of the solvated ions to the solvated electrode surface. If there is no direct adsorption of ions on the electrode surface, the electrostatic potential should change linearly inside the OHP. The electrostatic potential at the electrode surface ( $\phi_M$ ) and at the OHP ( $\phi_{OHP}$ ) depend on the electrode electrochemical potential, electronic structure of electrode material and dielectric permittivity of the solvent in the EDL.<sup>115–118</sup>

Equation 1.4 connects electrostatic potential with the electrochemical potential of electrons via following relation

$$E = -\mu_e + \phi_M, \quad (1.4)$$

where  $\mu_e$  is the chemical potential of electrons in the electrode, which represent the non-electrostatic contribution of the electronic work function of the electrode and depends on the electrode material nature. For ordinary bulk metals electrodes, which are usually used in the electrochemical setups, the density of electronic states (DOS) near the Fermi level is high. Therefore, the electron transfer/injection is hardly modifying  $\mu_e$ . Hence, the potential difference between two similar electrodes originates from the difference of  $\phi_M$  rather than from that of chemical potentials. Moreover, in experiments, the electrochemical potential is usually referenced to a known reference value (e.g Standard Hydrogen Electrode, Saturated Calomel Electrode etc.).

## 1.6 Scope of this Thesis

In this context, the effects of electrode material and electroactive species are still not fully understood. Improving the selectivity and yield in electrochemical processes demands a thorough understanding of the complex interactions occurring at the electrode-electrolyte interface, as well as a deep dive into the rate-determining steps that control the process. To address these gaps in knowledge, this thesis focuses on uncovering the fundamental aspects of electron transfer kinetics and thermodynamics through a detailed, multi-scale approach.

In Chapter 3, this research establishes a reliable benchmarking procedure for the electrochemical  $\text{Fc}^0/\text{Fc}^+$  reference electrode via DFT calculations, offering a robust computational reference for diverse electrochemical processes across various solvents. This approach enhances the accuracy and consistency of electrochemical measurements and theoretical predictions, setting a new standard for computational references.

Moving into Chapter 4, we examine the benzyl chloride electrocarboxylation reaction to further clarify the mechanisms of electron transfer at the electrode-solution interplay. This work aims to bridge the gap between theoretical predictions and practical applications by establishing a methodology for direct comparison between experimental data and simulation results. Such comparison is crucial for validating theoretical models and ensuring they accurately capture the electron-transfer phenomena.

Additionally, Chapter 5 investigates how the local solution structure within the EDL affects anion and cation radical formation, with particular emphasis on the impact of varying supporting electrolyte concentrations on the electrochemical behavior of systems. This analysis

seeks to find the connections between electrolyte concentration, radical formation, and potential-dependent activation energies that drive the overall efficiency of electrochemical reactions. These insights are essential for optimizing conditions in various electrochemical applications.

Through this comprehensive investigation, we aspire to contribute to the development of more accurate and predictive models for electrochemical processes. This, in turn, can inform the design of more effective systems and materials, advancing sustainable practices in applications from energy storage to catalysis. Ultimately, this thesis strives to offer valuable insights that bolster the sustainability, efficiency, and functionality of technologies reliant on electrochemical processes.

## 2. Computational methods

### 2.1 Electronic Structure Methods

The quantum chemical approach relies on the fundamental properties of the material. The ultimate goal of this approach is to solve the time independent non-relativistic Schrödinger equation and compute the total energy for a given atomic configuration.<sup>119–121</sup>

$$\hat{H}\Psi_k(\{\vec{r}_i\};\{\vec{R}_I\})=E_k\Psi_k(\{\vec{r}_i\};\{\vec{R}_I\}), \quad (2.1)$$

here  $\hat{H}$  is Hamiltonian,  $\Psi_k(\{\vec{r}_i\};\{\vec{R}_I\})$  is the many-body wave function and  $E_k$  is the total energy of the system. For a system consisting of  $n$  electrons and  $N$  nuclei the complex many bodies wave function depends on all the atomic ( $r$ ) and electronic positions ( $R$ )  $\Psi_k(r_1, r_2, \dots, r_n; R_1, R_2, \dots, R_n)$  and the Hamiltonian of the system consists of a sum of four terms as 2.2.

$$\hat{H}=\hat{T}_{\text{elec}}+\hat{V}_{\text{elec-elec}}+\hat{V}_{\text{elec-nuc}}+\hat{V}_{\text{nuc-nuc}}, \quad (2.2)$$

where  $\hat{T}_{\text{elec}}$  is the total kinetic energy of the electrons,  $\hat{V}_{\text{elec-elec}}$  and  $\hat{V}_{\text{nuc-nuc}}$  represent the repulsive potential energies due to the electron-electron and nucleus-nucleus interaction, while  $\hat{V}_{\text{elec-nuc}}$  in between corresponds to the attractive electrostatic interaction between the electrons and the nuclei.<sup>122</sup>

To further reduce computational complexity, only the ground state solution,  $\Psi_0$ , can be considered, which corresponds to the state with the lowest energy. For the system of  $n$  electrons and any given external potential ( $V_{\text{ext}}$ ) and for the electron-nuclei interaction, the variational principle defines a procedure to determine the ground state wave function, the ground state energy  $E_0$ , and any other properties of interest. In other words the ground state energy is a function of the number of electrons and the external potential:  $E_0 = E[n, V_{\text{ext}}]$ .

An analytical solution of equation 2.1 is feasible only for very small systems. Moreover, the exact solution is only available for the homogeneous electron gas, solving Equation 2.1. And, for the real materials, where the number of electrons is on the order of  $10^{23}$ , it becomes a formidable task and is essentially impossible to achieve analytically.<sup>120</sup>

Therefore, to reduce computational complexity it is suggested to employ a density functional theory (DFT). This approach utilizes certain state properties of a many-electrons system in an external field. Conventional approaches use the wave function  $\Psi_k$  as the central quantity, which contains full information of the system. The prime feature of the DFT approach is that it resolves the ground state electronic density of the system  $\rho^0(r_i)$  in order to replace the

many-body wave function and, therefore, reduce the dimensionality of the problem to 3 degrees of freedom rather than  $3N$  with  $N$  being number of electrons in the system. In that case, the electronic density is defined as the integral 2.3.

$$\rho_0(\vec{r}) = N \int \dots \int \Psi_0^*(\vec{r}_1, \vec{r}_2, \dots, \vec{r}_N) \Psi_0(\vec{r}_1, \vec{r}_2, \dots, \vec{r}_N) d\vec{r}_2 \dots d\vec{r}_N, \quad (2.3)$$

and determines the probability of finding any of the  $N$  electrons within volume element  $dr$ .

Now, the Hamiltonian is specified by the external potential and the total number of electrons, which can be computed from density by integration over all space. Therefore, the electronic wave function  $\Psi_k(\{r_i\})$  is a unique functional of the electronic density  $\Psi_k[\rho(r)]$  and, thus, all the ground state properties of the system can be obtained from its density. Consequently, the energy of the system can be written as a functional of the electronic density  $\rho(r)$  via Equation 2.4.

$$\begin{aligned} E[\rho(\vec{r})] &= \langle \Psi_k[\rho(\vec{r})] | \hat{H}_{\text{elec}} | \Psi_k[\rho(\vec{r})] \rangle = \\ &= T_{\text{elec}}[\rho(\vec{r})] + V_{\text{elec-elec}}[\rho(\vec{r})] + V_{\text{elec-nuc}}[\rho(\vec{r})] =, \\ &= F[\rho(\vec{r})] + \int V_{\text{ext}}(\vec{r}) \rho(\vec{r}) \end{aligned} \quad (2.4)$$

where the functional  $F[\rho(\vec{r})]$  contains the functional for the kinetic energy of the electrons  $T_{\text{elec}}[\rho(\vec{r})]$  and that for the potential energy due to the electron-electron interaction  $V_{\text{elec-elec}}[\rho(\vec{r})]$ .

However, it needs a confirmation that a certain electronic density is the desirable ground state density  $\rho_0(\vec{r})$ . Thus, the functional  $F[\rho(\vec{r})]$  that delivers the ground state energy of the system, delivers the lowest energy if the input density is the true ground state density (Equation 2.5).

$$E_0 = E[\rho_0(\vec{r})] \leq E[\rho(\vec{r})], \quad (2.5)$$

This means that for any trial density  $\rho(\vec{r})$ , which is associated with some external potential  $V_{\text{ext}}(\vec{r})$ , the energy obtained from the functional  $F[\rho(\vec{r})]$  in the equation 2.4 represents an upper bound to the true ground state energy.<sup>123–127</sup> The  $E_0$  results from the minimization of the functional  $F[\rho(\vec{r})]$  at the exact ground state density  $\rho_0(\vec{r})$ . Hence, the functional  $F[\rho(\vec{r})]$  is the essential part of the DFT, which can be approximated via equation 2.6.

$$F[\rho(\vec{r})] = T_s[\rho(\vec{r})] + J[\rho(\vec{r})] + E_{\text{XC}}[\rho(\vec{r})], \quad (2.6)$$

where  $T_s[\rho(\vec{r})]$  is the kinetic energy of non-interacting reference system and  $J[\rho(\vec{r})]$  is the Coulomb repulsion with  $E_{XC}[\rho(\vec{r})]$  being the exchange-correlation energy. Here,  $T_s[\rho(\vec{r})]$  can be computed by equation 2.7.

$$T_s[\rho(\vec{r})] = \sum_{i=1}^N \left\langle \phi_i \left| -\frac{1}{2} \nabla^2 \right| \phi_i \right\rangle, \quad (2.7)$$

where  $\phi_i$  is a one-electron wave-function.

Exchange-correlation energy  $E_{XC}[\rho(\vec{r})]$  is defined as

$$E_{XC}[\rho(\vec{r})] \equiv T_e[\rho(\vec{r})] - T_s[\rho(\vec{r})] + V_{\text{elec-elec}}[\rho(\vec{r})] - J[\rho(\vec{r})]. \quad (2.8)$$

Now, one-electron wave functions can be determined by one-particle equations under the constraint to reproduce the density of the interacting system.

## 2.2 Cyclic Voltammetry Simulation

### 2.2.1 Finite Difference Method

Computer simulation of cyclic voltammograms (CVs) can be helpful in obtaining additional information about a redox couple and drawing comparison of theoretical approaches with the experimental results<sup>128</sup>.

Reaction at the electrode surface generates concentration gradients resulting in diffusion. One of the approaches is to use the finite difference method<sup>129</sup> for solving differential equations based on a diffusion grid where each line represents a concentration array. The total time of a CV simulation equals twice the potential range scan divided by the scan rate. The increment ( $\Delta t$ ) equals to the total simulation time divided by the number of the time increments in the grid. Total length of the simulation cell is calculated as  $x_{\text{total}} = 6\sqrt{D_i t_{\text{total}}}$ . This corresponds to about four times the root-mean-square distance a species diffuses throughout the course of an experiment<sup>113,130</sup>. The distance increment ( $\Delta x$ ) equals the total distance divided by the number of distance increments in the grid. The main variable to be predicted is the concentration gradient that is computed from Fick's second law of diffusion in discrete form.

$$\frac{dC}{dt} = D_1 \frac{d^2C}{dx^2}, \quad (2.9)$$

$$\frac{C_j - C_i}{\Delta t} = \frac{D_1 [C_{i-1} - 2C_i + C_{i+1}]}{\Delta x^2}, \quad (2.10)$$

$$C_j = C_i + \frac{D_1 \Delta t [C_{i-1} - 2C_i + C_{i+1}]}{\Delta x^2}, \quad (2.11)$$

where  $D_i$  is the diffusion coefficient of the reaction species,  $\Delta t$  and  $\Delta x$  are the time and distance increments, whereas  $C_i$  and  $C_j$  denotes concentration in  $i$ -th and  $j$ -th segment on the grid.

However, equation 2.11 cannot be used for the first simulation box where the electrochemical reaction occurs. The rate and mass transfer to the electrode surface is then described in the simulation using the following flux equations:

$$J_{ox} = -J_{red} = \frac{k_f C_{ox,1} - k_b C_{red,1}}{1 + \frac{k_f \Delta x}{D_l} + \frac{k_b \Delta x}{D_l}}, \quad (2.12)$$

where  $J_{ox}$  and  $J_{red}$  are fluxes,  $C_{ox,1}$  and  $C_{red,1}$  are concentrations of the oxidized and reduced forms in the first simulation box at the distance from the electrode surface, whereas  $k_f$  and  $k_b$  are forward and backward rate constants. The surface concentrations of the oxidized and reduced forms can now be calculated using the two equations below:

$$C_{ox,0} = C_{ox,1} + \frac{J_{ox} \Delta x}{D_l}, \quad (2.13)$$

$$C_{red,0} = C_{red,1} + \frac{J_{red} \Delta x}{D_l}, \quad (2.14)$$

where  $C_{ox,0}$  and  $C_{red,0}$  are concentrations at the electrode surface.

The total faradic current density that corresponds to each time increments can be finally calculated as:

$$\frac{i_{total}}{A} = -nFJ_{ox}, \quad (2.15)$$

where  $n$  denotes the number of electrons participating in the process and  $A$  is the electrode surface area.

## 2.2.2 Finite Elements Method

To compute the concentration gradients of dilute species we use the Poisson-Nernst-Plank model<sup>118,131–134</sup> (PNP) in one-dimensional formulation to simulate the electric double layer (EDL) formation and determine potentials on the outer-Helmholtz plane. For planar electrodes this model can be written as a system of equations in the following way.<sup>118,130,132,134</sup>

$$\begin{cases} \frac{\partial}{\partial x} \left( \epsilon_0 \epsilon_r \frac{\partial V}{\partial x} \right) = -F \sum_{i=1}^n z_i C_i \\ \frac{\partial C_i}{\partial t} = -\frac{\partial N_i}{\partial x} \end{cases}, \quad (2.16)$$

where  $\epsilon_0$  and  $\epsilon_r$  are vacuum and solution dielectric permittivity,  $V$  represents the electrostatic potential across the simulation domain,  $F$  denotes Faraday's constant,  $C_i$  shows the concentration of  $i$ -th specie, whereas  $z_i$  shows the electric charge of  $i$ -th specie. Here,  $N_i$  denotes the mass flux of dilute specie.

$$N_i(x,t) = -D_i \frac{\partial C_i}{\partial x} - \frac{D_i F z_i C_i}{RT} \frac{\partial V}{\partial x} + \frac{D_i N_A C_i \sum_{i=1}^N a_i^3 \frac{\partial C_i}{\partial x}}{1 - N_A \sum_{i=1}^N a_i^3 C_i}, \quad (2.17)$$

where  $D_i$  is a diffusion coefficient of  $i$ -th specie and  $a_i$  is the radius of the specie represented as the solid sphere with the molecular volume of the specie.

The Stern layer can be accounted for via the boundary conditions relating the potential drop across the Stern layer with the potential gradient at the Stern/diffuse layer interface. Then it suffices to simulate only the condensed and diffuse layers in the computational domain. It was also shown that the surface charge boundary condition influences the potential drop on the OHP<sup>118,131</sup>. This boundary condition specifies the relationship between the potential ( $\phi$ ) and the potential gradient ( $\frac{\partial \phi}{\partial x}$ ) at the OHP. For planar electrodes, the boundary condition accounting the Stern layer is given by<sup>134</sup>:

$$\frac{\partial \phi}{\partial x} = \frac{\epsilon_0 \epsilon_r}{H} [\phi_{\text{ohp}} - \phi_{\text{surf}}], \quad (2.18)$$

where  $H$  is the EDL width,  $V_{\text{ohp}}$  is the potential at OHP, and  $V_{\text{surf}}$  is the potential at the electrode surface. In this study EDL width equals to the radius of the biggest specie in the system, which is  $\text{TBA}^+$  cation in this case. To account for the reduction in relative permittivity due to higher electrolyte concentration we use the following equation<sup>118,131</sup>.

$$\epsilon_r = \epsilon_r^{\text{bulk}} \left( \frac{C_{\text{solv}} \cdot \sum C_i}{C_{\text{solv}}} \right) + \epsilon_r^{\text{min}} \left( \frac{\sum C_i}{C_{\text{solv}}} \right), \quad (2.19)$$

where  $\epsilon_r^{\text{bulk}}$  is the dielectric permittivity of the pure solvent and  $C_{\text{solv}}$  is the number of moles in one liter of pure solvent (~19 M for MeCN at 25 °C).  $\epsilon_r^{\text{min}}$  shows drop in dielectric permittivity due to the supporting electrolyte concentration effect.

**Table 1.** Summary of the experimental<sup>135</sup> dielectric permittivity of the saturated EDL solutions near the electrode surface ( $\epsilon_r^{\text{min}}$ ) and the molar concentration of some pure solvent ( $C_{\text{solv}}$ ) used in our study.  $C_{\text{solv}}$  was calculated as a relation of the solvent density ( $\rho$ ) to the solvent molar mass (M).

| Solvent | $\epsilon_r^{\text{min}}$ | $C_{\text{solv}}$ [M] |
|---------|---------------------------|-----------------------|
| MeCN    | 5.0                       | 19.15                 |
| DCM     | 4.5                       | 15.62                 |
| NMF     | 10.2                      | 17.12                 |
| EtOH    | 4.0                       | 17.14                 |
| H2O     | 6.3                       | 55.55                 |



The zero flux boundary condition was set at the Stern/diffuse layer due to the absence of species insertion in the electrode material. The initial conditions in the diffuse layer satisfy the electroneutrality condition and were set to zero for electrostatic potential, and bulk concentrations for all chemical species in the system.

## 2.3 Thermodynamics

Calculations of reaction free energies require thermodynamic contributions in addition to the energies obtained from the electronic structure theory. This requires to know a partition function that comprises of rotational, vibrational and translational degrees of freedom which can be computed within the rigid rotator<sup>136,137</sup>, free translator<sup>137,138</sup> and harmonic oscillator<sup>137</sup> approximations, respectively. We note that the rotational partition function is different for linear and non-linear molecules.

$$q = q_{\text{rot}} \cdot q_{\text{trans}} \cdot q_{\text{vib}}, \quad (2.21)$$

$$q_{\text{rot}}^{\text{linear}} = \frac{8\pi^2 k_B T}{h^2}, \quad (2.22)$$

$$q_{\text{rot}}^{\text{non-linear}} = \left( \frac{8\pi^2 k_B T}{h^2} \right)^{3/2} \cdot \frac{(I_A I_B I_C \pi)^{1/2}}{\sigma}, \quad (2.23)$$

$$q_{\text{trans}} = \frac{V(2\pi M k_B T)^{3/2}}{h^3}, \quad (2.24)$$

$$q_{\text{vib}} = \prod_i \frac{e^{-\frac{h\nu_i}{2k_B T}}}{1 - e^{-\frac{h\nu_i}{k_B T}}}, \quad (2.25)$$

where  $k_B$  is the Boltzmann constant,  $h$  is the Plank constant,  $T$  is the temperature,  $M$  is the molecular mass,  $V$  is the volume of 1 mol of ideal gas,  $\sigma$  is the symmetry number,  $I$  are moments of inertia, and  $\nu$  are the vibrational frequencies.<sup>139</sup> The entropy ( $S$ ) and heat capacity ( $C_p$ ) are calculated from the partition function.

$$H(T) = E + E_{\text{ZPE}} + \int_0^T C_p dT, \quad (2.26)$$

$$G(T, p) = H(T) - TS(T, p), \quad (2.27)$$

Thus, enthalpy and Gibbs free energy can be calculated using the electronic energy ( $E$ ) and the zero-point vibration energy ( $E_{\text{ZPE}}$ ).

## 2.4 Kinetics

The classical Marcus-Hush model (CMH) assumes the Gibbs free surfaces of reduced (Red) and oxidized (Ox) species to be parabolic and have equal curvature (Figure 7).<sup>110,140–142</sup>

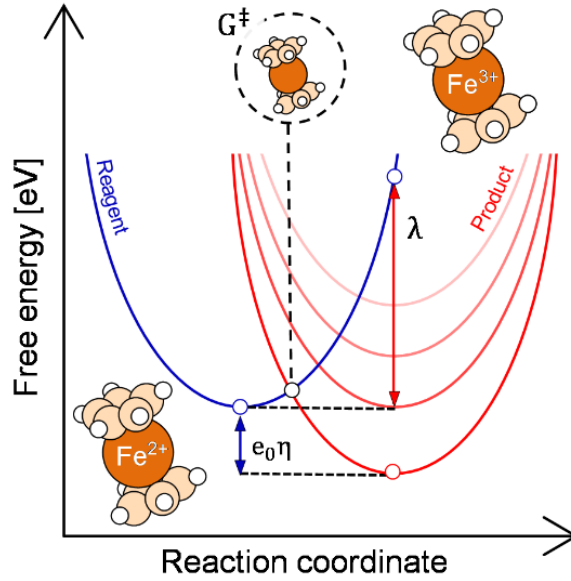


**Figure 7.** Standard free energy diagram vs. reaction coordinate for an electron-transfer reaction in a precursor complex e.g.  $\text{Fc}^0/\text{Fc}^+$ . The curve for a reagent (the blue line, the product electronic state is represented by the red line) includes the energy of an electron on the electrode at the Fermi level corresponding to potential  $E$ . Interception on two parabolas (electronic states) denote the activation energy for the electron transfer controlled by overpotential  $\eta$ .

The energy of the transition state, and hence the activation energy ( $\Delta G^\ddagger$ ), is therefore determined by the intersection of these two curves and can be calculated through equation 2.28.

$$\Delta G^\ddagger = \frac{(\lambda_0 + \lambda_i)}{4} \left[ 1 + \frac{F(E - E^0)}{(\lambda_0 + \lambda_i)} \right]^2, \quad (2.28)$$

where  $\lambda_0$  represents inner-sphere reorganization energy and  $\lambda_i$  denotes outer-sphere reorganization energy. The reaction activation energy is introduced by the difference of the electrode potential ( $E$ ) and the standard equilibrium potential ( $E^0$ , SEP).

The standard reduction potential refers to the reaction free Gibbs energy change at equilibrium and can be calculated by Equation 2.30.

$$E^0 = -\frac{\Delta G_r}{nF} - E_{\text{ref}}, \quad (2.29)$$

where  $\Delta G_r$  is the reaction free energy change,  $n$  shows the number of electrons participating in the process and  $F$  is the Faraday's constant. SRP is computed with respect to the reference electrode<sup>143</sup>.  $\lambda_{\text{solv}}$  is related to the reorganization of the solvation shell around the reductant due to the electron transfer process and can be computed via Equation 2.30.<sup>144,145</sup>

$$\lambda_{\text{solv}} = \frac{e^2}{8\pi\epsilon_0} \left( \frac{1}{a_0} - \frac{1}{R} \right) \left( \frac{1}{\epsilon_{\text{op}}} - \frac{1}{\epsilon_s} \right), \quad (2.30)$$

where  $e$  denotes elementary electron charge,  $\epsilon_0$  represents vacuum dielectric permittivity, whereas  $\epsilon_s$  and  $\epsilon_{op}$  are static dielectric permittivity of a solvent and corresponding to the optical dielectric permittivity.  $a_0$  and  $R$  show the molecular radius of reductant and its position from the electrode surface.  $R$  is usually taken as  $2a_0$ <sup>113</sup>.  $\lambda_i$  represents the inner-sphere reorganization energy related to the change of bonds length and angles due to the charge transfer. This term can be computed by the following Equation 2.31:

In the given equation,  $\lambda_i$  represents the reorganization energy associated with alterations in bond lengths and angles between atoms during the electron charge transfer process. This parameter for the case of ferrocene/ferrocenium system can be calculated as

$$\lambda_i = G_{Fc}(Q_{Fc^+}) - G_{Fc}(Q_{Fc}), \quad (2.31)$$

where  $G_{Fc}$  denotes the Gibbs Free energy of the reduced state, and  $Q$  represents the equilibrium geometries of ferrocenium and ferrocene.

According to this model, a reaction is considered probable when the free energy associated with the reaction step is, at a minimum, thermoneutral. Having knowledge of the activation energies for the electron transfer, one can easily compute the potential-dependent forward and backward rate constants by<sup>71,75,146–148</sup>

$$k_f = k^0 e^{-\alpha \frac{F(E-E^0)}{RT}}, \quad (2.32)$$

$$k_b = k^0 e^{(1-\alpha) \frac{F(E-E^0)}{RT}}, \quad (2.33)$$

where  $k^0$  is the standard rate constant, which is dependent on the total reorganization energy and  $\alpha$  is a potential dependent symmetry factor. This parameter can be evaluated by the following equation

$$\alpha = \frac{1}{2} + \frac{F(E-E^0)}{4\lambda}, \quad (2.34)$$

This parameter can be calculated from the following equation

$$k^0 = Z e^{\frac{-\lambda F}{4RT}}, \quad (2.35)$$

where  $Z$  is the collision frequency with the electrode surface which depends on the molar mass of the target molecule.

In the early development of Marcus theory<sup>111,149–154</sup>, the reactants were encountered the electrode surface by hard-sphere Brownian motion and the pre-exponential factor for the rate constant were written in terms of collision frequency.<sup>71,148</sup> The collision frequency ( $Z$ ) can be assessed by the Equation 2.36:

$$Z = \sqrt{\frac{RT}{2\pi M}}, \quad (2.36)$$

where R and T are gas constant and temperature. M denotes the molar mass of the reactant.

## 2.5 Computational Details for this Thesis

Here, we provide a summary and additional information of the methodology used in this thesis.

We start our investigation of electron transfer kinetics and thermodynamics by analyzing the performance of popular DFT methods using ORCA (version 5.0.3) code.<sup>155–157</sup> We considered a wide selection of popular exchange-correlation functionals (BHANDLYP, B3LYP, BLYP, M06-2X, M06, M06-L, PBE, PBE0) together with the ma-def2-TZVPP basis set to accurately represent the electronic structure of all atomic species<sup>158,159</sup>. Geometries of chemical species were fully relaxed using the unrestricted Kohn-Sham approach for pure and hybrid functionals. Frequency calculations were performed at the same level of theory to calculate Gibbs free energies at 298.15 K.

Our starting point is the redox couple ferrocene/ferrocenium ( $\text{Fc}^0/\text{Fc}^+$ ) that is widely applied as a reference system in electrochemical reactions.<sup>160–180</sup> The solvation effects of acetonitrile (MeCN), dimethyl formamide (DMF) and acetone (ACE) have been taken into account by using the CPCM solvation model<sup>181</sup> implemented in ORCA. Implicit solvation was modeled using the CPCM continuum solvation model in acetonitrile ( $\epsilon = 36.6$ , Chapter 3, Chapter 4).

In Section 5, we investigated the influence of the solvent and the supporting electrolyte concentration on the electron transfer thermodynamics. We computed the equilibrium potentials of the computational ferrocene/ferrocenium electrode (CFE) and test the molecules (Chapter 5) with the BP86 functional and the def2-TZVP basis set by the Gaussian 16C quantum chemical package.<sup>182</sup>

To account for the solvation effects of a solvent and supporting electrolyte mixture, we employed the PCM and COSMO-RS<sup>183–192</sup> solvation models. For COSMO-RS calculations, we used the COSMOTermX computational tool (version 19.0.5). We selected the BP86 functional because the COSMO-RS solvation model is parametrized to perform well with this functional. The calculated  $\text{Fc}^0/\text{Fc}^+$  absolute potential in gas phase is 6.74 V which is in line with the experimental value 6.71 V.<sup>173</sup>

For periodic calculations of the electrode materials, the spin-polarized electronic structure was calculated using the PBE functional<sup>193</sup>, with an energy cutoff of 450 eV for the plane-wave basis set. The interactions between electrons and ions were described using the PAW method.<sup>194,195</sup> All calculations were conducted using the VASP software (version 5.4).<sup>195,196</sup> Solvation effects were included by applying the implicit solvation model<sup>197,198</sup> developed by Hennig and colleagues, known as VASPsol.<sup>199,200</sup> In this model, the electrostatic interaction with the implicit solvent is determined based on a linear polarization approach, where the medium's relative permittivity varies continuously with electron density. A switching function around a specified isodensity value adjusts the relative permittivity from 1 near the surface to the bulk solvent value farther away. This modified Hartree potential is derived by solving the modified Poisson equation. The dielectric constant of acetonitrile (MeCN) was set to 54.4, corresponding to a supporting electrolyte (n-NBu<sub>4</sub>PF<sub>6</sub>) concentration of 100 mM (Section 5.1). All geometries were optimized to achieve a gradient less than 0.05 eV/Å, with wave functions converged to within  $5 \times 10^{-6}$  eV. The precision setting in VASP was adjusted to “accurate,” and the automatic optimization of the real-space projection operators was enabled. The Debye length was set to 8.08 Å, reflecting an electrolyte concentration of 100 mM. The surface charge was modelled according to the previously reported procedure.<sup>64,201</sup>

### 3. Ferrocene/Ferrocenium Reference for Cyclic Voltammetry Simulation

This chapter is based on [Kramarenko, A. S.; Sharapa, D. I.; Pidko, E. A.; Studt, F. Ab Initio Kinetics of Electrochemical Reactions Using the Computational  $\text{Fc}^0/\text{Fc}^+$  Electrode. J. Phys. Chem. A 2024].

Determining the equilibrium potential of a particular compound under experimental conditions is crucial, due to the difficulties of obtaining the absolute equilibrium potential of a half-cell, experimentally. Therefore, when discussing the equilibrium potential ( $E^0$ ), the relative potential to the reference half-cell is often used. The most popular reference electrode for electrochemical measurements in aqueous solution is the standard hydrogen electrode (SHE). The International Union of Theoretical and Applied Chemistry (IUPAC) recommends the SHE potential value of 4.44 V, which was reported by Trasatti in 1986.<sup>143</sup> While the SHE potential is often used in computational research, problems arise due to its dependence on the models<sup>112,202,203</sup>, computational methods, and differences in reported experimental SHE potentials (ranging from 4.05 to 4.73 V).<sup>126,127,204,205</sup> The problems are particularly noticeable in non-aqueous media, which prompted IUPAC to propose the  $\text{Fc}^+/\text{Fc}^0$  (ferrocenium/ferrocene) redox pair as an alternative reference frame.<sup>180</sup> Despite the fact that ferrocene usually serves as an internal reference, its redox potential is influenced by specific solvation effects, which casts doubt on the "ferrocene assumption". The equilibrium potential of ferrocene can vary up to 0.56 V depending on the solvent under the influence of ion pairing between the ferrocenium cation and the anion of the supporting electrolyte in certain solvents.<sup>177,178</sup> Numerous studies have focused on regulating the reduction potential of ferrocene using substitutions and linkers in the ferrocene core.<sup>160,161,163,173,175,178,206,207</sup> Setting up the equilibrium potential of ferrocene is a time-consuming and resource-intensive process that leads to the integration of quantum chemical calculations to facilitate this work.

#### 3.1 Benchmark Calculations of the Absolute reduction potential of $\text{Fc}^0/\text{Fc}^+$ Electrode

Electrode materials play a crucial role in electrochemical processes and their electronic structure is a fundamental factor that controls the efficiency and dynamics of electron transfer processes in electrochemical systems.<sup>63,72,75,208</sup> Electron transfer kinetics, which control the rate and mechanism of electrochemical reactions, is highly sensitive to the electronic properties of

the electrode, such as density of states (DOS), electrochemical potential of electrons, and band structure. These properties influence the alignment of energy levels between the electrode and the redox species in the electrolyte, thereby affecting the ease with which electrons can be transferred across the electrode-electrolyte interface.<sup>59,112,113,149,201,209,210</sup>

The density of states at the Fermi level is particularly critical, as it determines the availability of electrons for transfer in a metallic or semiconducting electrode. A high DOS at the Fermi level typically facilitates a faster electron transfer, as seen in materials like platinum and other transition metals, which are known for their excellent catalytic activity and low overpotentials.<sup>75,148,211,212</sup> In contrast, materials with lower DOS or wider band gaps, such as certain semiconductors, can present higher energy barriers to electron transfer, leading to slower kinetics.

The electrochemical potential of the electrode electrons, which defines the energy required to extract/inject an electron from/to the bulk to the surface, also plays a crucial role. A well-matched electrochemical potential of electrons in the electrode and the redox species ensures efficient charge transfer with minimal energy loss. Additionally, surface states and defects within the electrode material can introduce localized electronic states that either facilitate or hinder electron transfer, depending on their nature and distribution. In this section we make some assumptions stating that the density of states for the electrode material we are studying (GC) is high and therefore DOS does not have large influence on the overall process kinetics and the electrode's applied potential ( $E$ ) is approximated by manual modulation of the value without explicit calculation of the material properties.

Overall, electrochemical process can be expressed using a simple scheme which is shown in Figure 8.

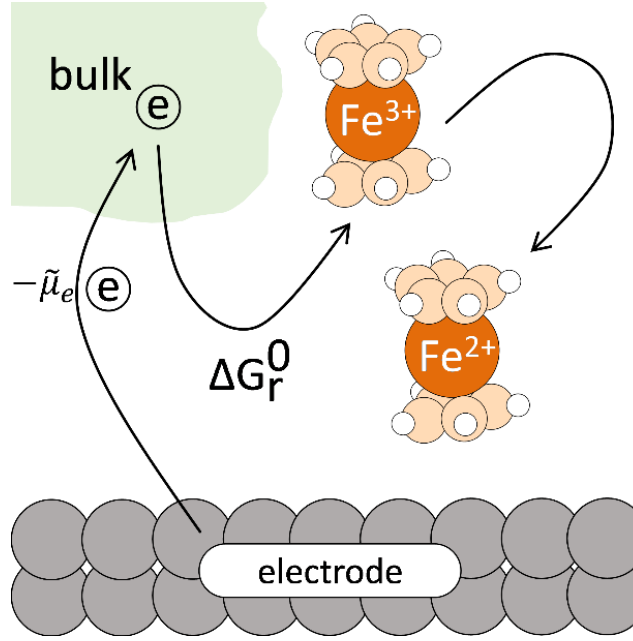


**Figure 8.** Schematic representation of the electron transfer from the electrode material to the reduced state in the electrode-electrolyte interface. Here, the solvated work function of the electrode ( $-\tilde{\mu}_e$ ) shows the difference in electronic state energy in the electrode material and the bulk solution, where the energy of electrons is zero and  $\Delta G_r^0$  is the free Gibbs energy of the respective electrochemical reaction (here we show the case for ferrocenium/ferrocene reduction process).

Now, the applied potential can be stated in the following way:

$$E = -\tilde{\mu}_e - E_{\text{ref}}, \quad (3.1)$$

where  $E_{\text{ref}}$  is the Gibbs free energy of the reference reaction (for example: hydrogen evolution for SHE).

Usually in the electrochemical studies, electrochemical potential of electrons is referenced to a system with known thermodynamic parameters (Figure 9). Therefore, the electron transfer energy (ET) can be calculated through the Equation 3.2.

$$ET = E - \Delta G_r^0, \quad (3.2)$$

At the equilibrium electron transfer energy is zero, therefore  $\Delta G_r^0 = \tilde{\mu}_e$ .



### Electrochemical potential

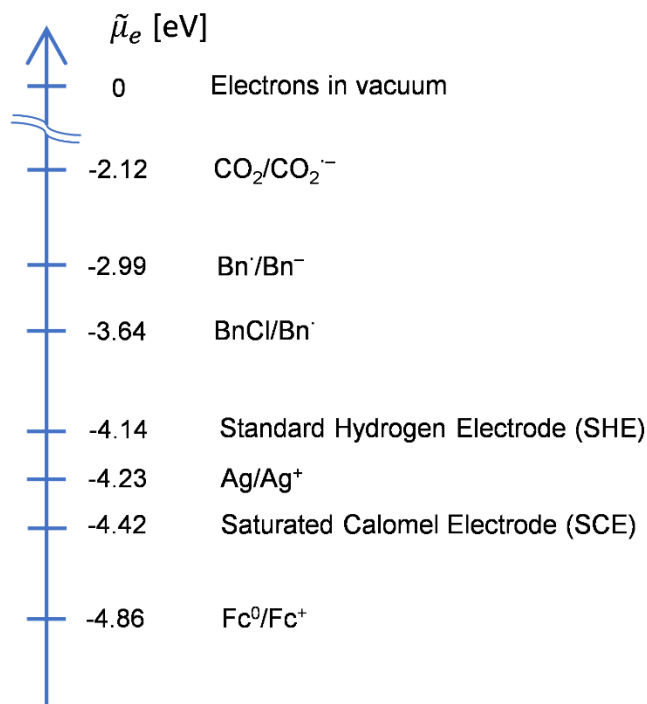


**Figure 9.** DFT computed electrochemical potentials of reference reactions and the experimentally obtained electrochemical potential of reference electrodes in acetonitrile solutions.<sup>58,143,213</sup>

In this section, we assessed the reliability of the functionals by comparing calculated reaction Gibbs free energies ( $\Delta G_r^0$ ) of  $\text{Fc}^0/\text{Fc}^+$  couple with experimental results.

$$\Delta G_r^0 = (G_{\text{red}} - G_{\text{ox}}) - E_{\text{ref}}, \quad (3.2)$$

where  $G_{\text{red}}$  is the Gibbs free energy of the corresponding  $\text{Fc}^0$  state and  $G_{\text{ox}}$  is the free energy of the  $\text{Fc}^+$  cation radical.

The  $\text{Fc}^0/\text{Fc}^+$  couple was chosen due to its wide applicability in experimental electrochemistry as a well-studied reference, thus, there are many experimental ionization potentials obtained by the photoelectron and the electron impact spectroscopy.<sup>160,175</sup> In this thesis, we choose as the experimental reference, the value ( $6.71 \pm 0.08$  eV) recommended by the National Institute of Standards and Technology (NIST).<sup>175</sup>

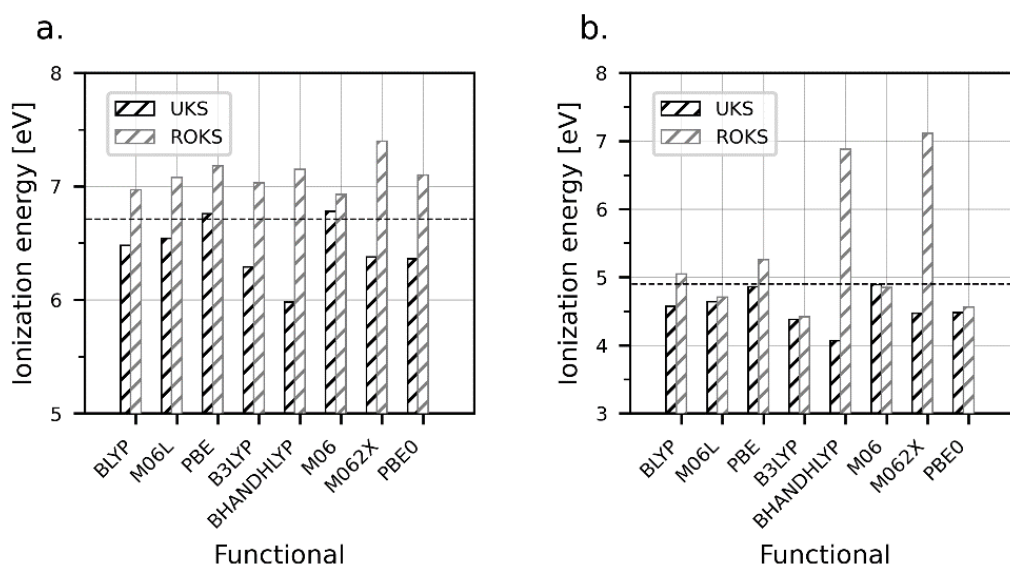


**Figure 10.** Ionization energies of the  $\text{Fc}^0/\text{Fc}^+$  system obtained with various functionals for unrestricted and restricted Kohn-Sham calculations in the gas-phase (a.) and the acetonitrile (b.). Dashed lines denote experimental values for ferrocene ionization in the gas phase and the acetonitrile solution. Reproduced from ref. 214. Available under a CC BY-NC-ND 4.0 license. Copyright 2024 Kramarenko A.S., Sharapa D.I., Pidko E.A., Studt F.

Figure 10 shows ionization energies of the  $\text{Fc}^0/\text{Fc}^+$  reference system (CFE) calculated with unrestricted<sup>215</sup> (UKS) and restricted (ROKS) open-shell calculations.<sup>216</sup> Analyzing the obtained results, it can be seen that UKS consistently underestimates the ionization energy (IE), whereas ROKS overestimates IE values, in some cases for more than 1.5 eV. The most accurate results were obtained by the PBE and M06 functionals, which yield IEs of 6.76 and 6.78 eV in gas phase, respectively. Moving from the gas-phase to the solution ionization potential decreases dramatically due to the solvation effect of the cation radical in the polar acetonitrile solution. The mean absolute error (MAE) for UKS calculations in the gas phase does not exceed 0.3 eV overall. This notable error arises mainly from an over-estimation of the stability of oxidized species, particularly by hybrid functionals that involve a mixture of Hartree-Fock (HF) correlation.<sup>160,175,180,207,217</sup>

Previous research has shown that the error tends to increase with a higher proportion of HF exchange in the functional, except for the two functionals mentioned earlier. Transitioning from the UKS to the ROKS approach dramatically alters this situation, making ionization energy less reliant on the amount of HF in the functionals and shifts  $\text{IE}_{\text{calc.}}$  into the range of experimental values from 6.6 to 7.20 eV.<sup>175</sup> This is related to the phenomenon of the adverse effect of spin contamination to the HF methods.<sup>216,218,219</sup> Consequently, a greater HF-exchange

component within the functional results in an increased occurrence of spin contamination. When dealing with open-shell systems using an unrestricted wave function, the measurement of spin contamination is conducted through the expectation value of the  $S^2$  operator. A commonly accepted guideline is that spin contamination is considered negligible if the difference between the spin-squared value  $S^2$  and  $S(S+1)$  is less than 10%, where  $s$  represents half number of the unpaired electrons. Spin contamination has a more pronounced negative impact on HF methods compared to DFT methods. As a result, a higher HF-exchange component within the functional leads to an increased incidence of spin contamination. It was demonstrated that ferrocenium cation can be affected by this both with DLPNO-CCSD(T)<sup>220</sup> and double-hybrids<sup>125</sup>.

Experimentally, applied potentials ( $E$ ) in solution are usually measured against a reference electrode and can be calculated according to equation 3.2

$$E_{\text{solv}} = (E^0 + E_{\text{ref}})nF \quad (3.3)$$

where  $E_{\text{solv}}$  denotes the  $\Delta G_r^0$  in a specific solvent,  $F$  the Faradays constant and  $E_{\text{ref}}$  is the absolute potential of the reference electrode in a particular solvent,  $n$  denotes the number of electrons transferred during the process, and  $E^0$  corresponds to the experimental standard equilibrium potential. The  $E_{\text{solv}}$  values for several commonly used aprotic solvents are summarized in Table 1 and compared to our computational results using the PBE and M06 functional.

**Table 2.** Comparison of experimental and computed applied electrode potentials in solution ( $E_{\text{solv}}$ ) of the  $\text{Fc}^0/\text{Fc}^+$  system in MeCN, dimethyl formamide (DMF) and ACE solvents.

| Solvent | $E_{\text{solv}}$ [eV]  |      |      |
|---------|---|------|------|
|         | Experiment  | PBE  | M06  |
| MeCN    | 4.88 <sup>146,203</sup> , 4.90 <sup>143</sup> , 5.25 <sup>171</sup> | 5.26 | 4.85 |
| DMF     | 5.33 <sup>180,204</sup> , 4.72 <sup>126,127</sup>                   | 5.28 | 5.03 |
| ACE     | 5.46 <sup>164,169</sup> , 4.74 <sup>90</sup>                        | 5.61 | 6.90 |

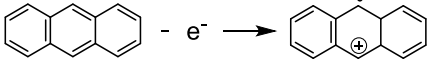
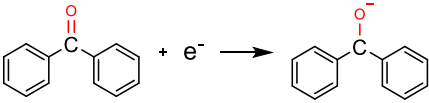
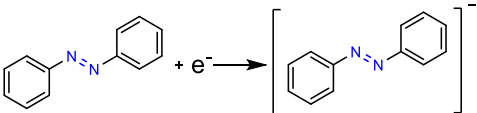
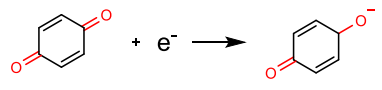
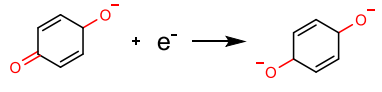
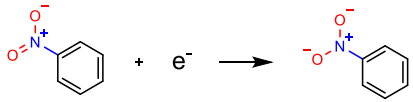
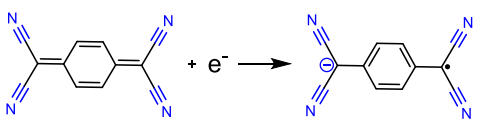
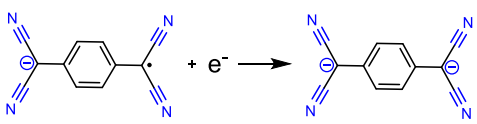
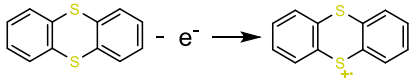
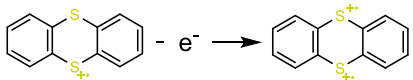
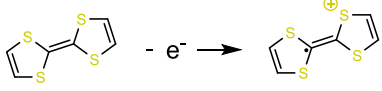
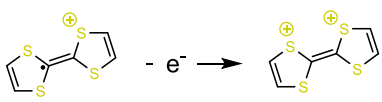
As it can be seen from Table 2, both functionals give reasonable results, especially considering that there is also large disagreement among the experimentally reported data.<sup>171,175,177</sup> Here, we are interested in the absolute potential of  $\text{Fc}^0/\text{Fc}^+$  in acetonitrile solution,

where the average value of the experimentally obtained absolute potentials is 5.01 eV with a mean absolute error (MAE) of 0.16 eV.

### 3.2 Redox Potentials of Organic Molecules in Non-aqueous solvents

We validated our method by computing equilibrium potentials and electron transfer activation barriers of an extensive list of organic molecules (Figure 11), that have been discussed for a broad range of applications such as for energy storage<sup>221–224</sup>, dyes<sup>225–227</sup> and photo-responsive membranes production.<sup>223,228–231</sup>

Standard equilibrium potential, one of the most crucial parameters in electrochemistry represents the difference between the target reaction energetics and the reference electrode potential, thus, even poor predicting ability of the reference electrode potential, might end up in a correct differential value. Therefore, we used a wide range of electrochemical reactions to compare the accuracy of the functional in equilibrium potential prediction. Standard equilibrium potentials were collected from the literature data<sup>113,178,221–223,225,226,228–237</sup> and summarized in the Figure 11. Experimental results are often measured with respect to the SCE electrodes, therefore to convert  $E^0$  from SCE to the  $\text{Fc}^+/\text{Fc}^0$  scale, one needs to extract 0.46 V from the value of  $E^0$  vs. SCE.

| #  | Reactions   | $E^0$ [V vs. $\text{Fc}^+/\text{Fc}^0$ ] |
|----|---|--|
| 1  |  $-\text{e}^- \rightarrow$   | 0.84                                     |
| 2  |  $+\text{e}^- \rightarrow$   | -2.34                                    |
| 3  |  $+\text{e}^- \rightarrow$   | -1.86                                    |
| 4  |  $+\text{e}^- \rightarrow$   | -1.00                                    |
| 5  |  $+\text{e}^- \rightarrow$   | -1.86                                    |
| 6  |  $+\text{e}^- \rightarrow$   | -1.61                                    |
| 7  | $\text{O}=\text{O} + \text{e}^- \rightarrow \cdot\text{O}-\text{O}^-$   | -1.28                                    |
| 8  |  $+\text{e}^- \rightarrow$  | -0.33                                    |
| 9  |  $+\text{e}^- \rightarrow$ | -0.75                                    |
| 10 |  $-\text{e}^- \rightarrow$ | 0.77                                     |
| 11 |  $-\text{e}^- \rightarrow$ | 1.28                                     |
| 12 |  $-\text{e}^- \rightarrow$ | -0.16                                    |
| 13 |  $-\text{e}^- \rightarrow$ | 0.20                                     |

**Figure 11.** Reference reactions used for estimation of accuracy in reduction potential prediction and its experimental reduction potentials extracted from the published literature. Reproduced from ref. <sup>214</sup>. Available under a CC BY-NC-ND 4.0 license. Copyright 2024 Kramarenko A.S., Sharapa D.I., Pidko E.A., Studt F.

Now, by determining the Gibbs free energy of the aforementioned reactions and utilizing the electrochemical potential of the ferrocene/ferrocenium system as a benchmark, equilibrium potentials can be computed using Equation 3.4.

$$E^0 = -\frac{\Delta G_r^0}{nF}, \quad (3.4)$$

where  $F$  denotes Faraday constant and  $n$  shows the number of electrons transferred during the process. We derived  $E^0$  values from DFT calculations, without relying on any experimentally received data. Comparison of experimental and computed reduction potentials by our methodology are shown in Figure 12.

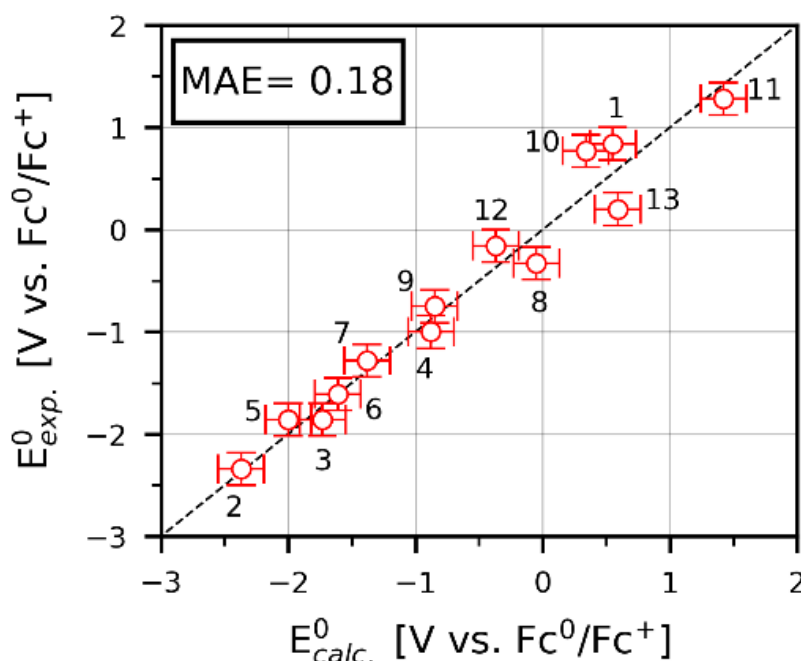


**Figure 12.** Comparison of experimental and calculated reduction potentials of the test set of 13 test reactions from Figure 11 using the CFE with the M06 functional. Reaction Gibbs free energies were computed using equations 3.2 and 3.4. Reproduced from ref. <sup>214</sup>. Available under a CC BY-NC-ND 4.0 license. Copyright 2024 Kramarenko A.S., Sharapa D.I., Pidko E.A., Studt F.

The error bars in Figure 12 represent the deviation of experimentally observed reduction potentials due to the error raised from the reference system. Now, comparing the MAE of all studied functionals (Figure 13), we can assess the accuracy of the DFT methods.

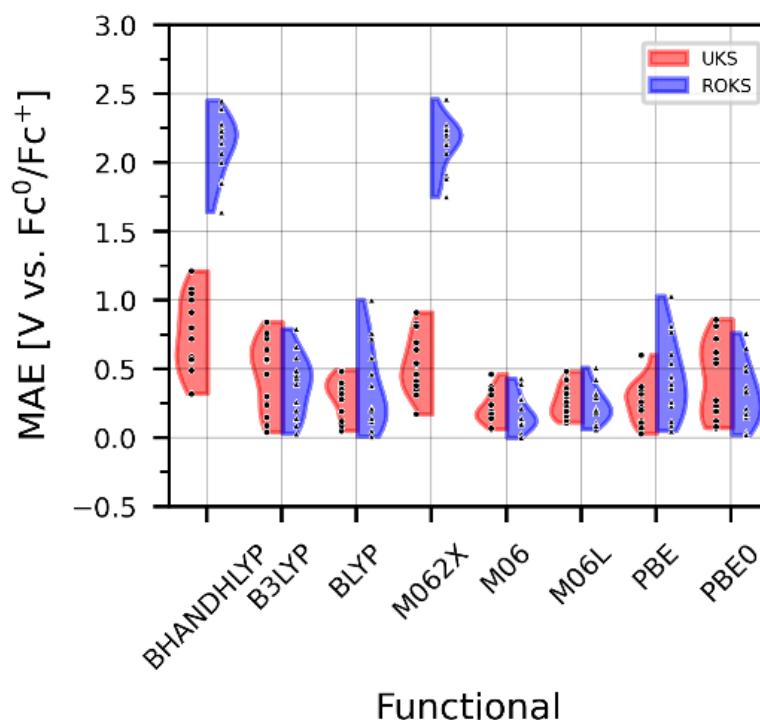


**Figure 13.** Performance of studied DFT functionals for predicting standard reduction potentials. The red area denotes mean average error distribution for standard reduction potentials computed with UKS scheme, whereas the blue areas represent the mean average error for ROKS computed SEPs. Black dots and triangles represent the computed values of SEP for studied reactions (Figure 11).

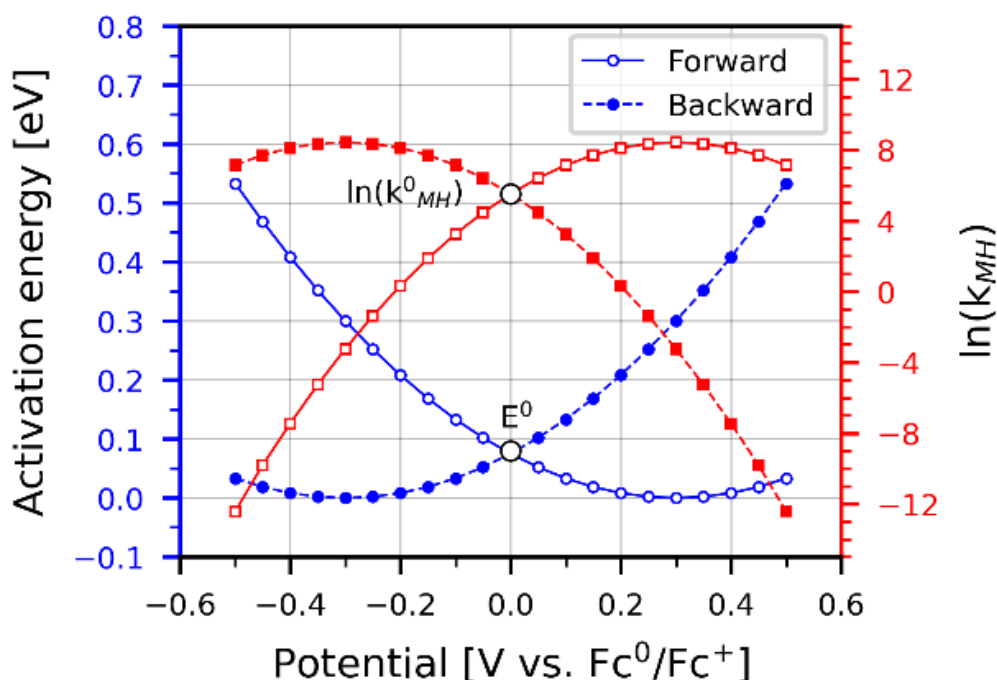
The UKS calculations consistently underestimate reduction potentials across all the functionals studied, while the ROKS approach provides more accurate predictions for reduction potentials. Nonetheless, the M062X and BH&HLYP functionals tend to overestimate the absolute potential of ferrocene/ferrocenium, leading to a high overall error for these particular functionals.

Figure 12 and Figure 13 confirm the high accuracy of our computational  $\text{Fc}^0/\text{Fc}^+$  electrode at the M06 level for the estimation of the reduction potentials of this test set with the mean absolute error of only 0.18 V. Note, that this error is within the accuracy of typical DFT functionals ( $\pm 0.20$  eV). Note that the experiments also deviate in reported reduction potentials, with deviations between experiments being as large as 0.16 V. Having established that we are able to calculate SEPs, and thus the thermodynamics of an electrochemical system using the CFE, we will now use this to evaluate electron transfer kinetics in the framework of the Marcus-Hush model.<sup>112,113,238–243</sup>

### 3.3 Electron Transfer Kinetics on Inert Glassy Carbon Electrode Surface

To evaluate electron transfer kinetics, we employed the outcomes of ROKS M06/ma-def2-TZVPP calculations incorporating a solvation model. Subsequently, we applied these findings to the Marcus-Hush model discussed in Section 2.4.

In the case of the  $\text{Fc}^+/\text{Fc}^0$  system, the computed reorganization energy is partitioned into 0.02 eV for inner-sphere reorganization and 0.28 eV for outer-sphere reorganization energies. Subsequently, we computed the activation energy for both the forward and backward reactions using Equation 2.28, as illustrated in Figure 14.



**Figure 14.** The dependence of the activation energy (dots) and rate constants (squares) for the  $\text{Fc}^0/\text{Fc}^+$  oxidation process on the applied potential. The open white circles at 0 V correspond to the respective values at the standard reduction potential. Reproduced from ref. <sup>214</sup>. Available under a CC BY-NC-ND 4.0 license. Copyright 2024 Kramarenko A.S., Sharapa D.I., Pidko E.A., Studt F.

Figure 14 shows that the activation energy is dependent on the working electrode potential and intersects at the point of SEP, where the activation energy relies specifically on the reorganization energy. A similar behavior was observed for the process rate constants. Table 3 collects thermodynamic and kinetic parameters of the studied reactions calculated at the ROKS M06/ma-def2-TZVPP level of theory.



**Table 3.** Computed Gibbs free energy, standard equilibrium potentials and kinetic parameters obtained from the Marcus-Hush model computed via the methodology in Section 2.4. Reaction free energies are calculated via Equation 3.2 and SEP are computed using Equation 3.4. The inner-structure reorganization energy ( $\lambda_i$ ) and the solvent reorganization energy ( $\lambda_{\text{solv}}$ ) were computed using Equation 2.31 and Equation 2.30.

| Reaction                         | $\Delta G$ [eV] | $E^0$ [V vs. $\text{Fc}^0/\text{Fc}^+$ ] | $\lambda_{\text{solv}}$ [eV] | $\lambda_i$ [eV] | $k^0$ [cm/s] |
|----------------------------------|-----------------|--|------------------------------|------------------|--------------|
| $\text{Fc}^0/\text{Fc}^+$        | -4.85           | 0.00                                     | 0.28                         | 0.02             | 248.59       |
| $\text{BQ}/\text{BQ}^-$          | -3.97           | -0.88                                    | 0.32                         | 0.26             | 21.39        |
| $\text{BQ}^-/\text{BQ}^{2-}$     | -2.85           | -2.00                                    | 0.32                         | 0.72             | 0.24         |
| $\text{BP}/\text{BP}^-$          | -2.48           | -2.37                                    | 0.26                         | 0.21             | 48.04        |
| $\text{O}_2/\text{O}_2^-$        | -3.47           | -1.38                                    | 0.48                         | 0.53             | 0.60         |
| $\text{NB}/\text{NB}^-$          | -3.24           | -1.61                                    | 0.31                         | 0.31             | 13.58        |
| $\text{TCNQ}/\text{TCNQ}^-$      | -4.80           | -0.05                                    | 0.26                         | 0.15             | 81.36        |
| $\text{TCNQ}^-/\text{TCNQ}^{2-}$ | -4.00           | -0.85                                    | 0.26                         | 0.39             | 7.87         |
| $\text{An}/\text{An}^+$          | -5.4            | 0.55                                     | 0.26                         | 0.06             | 209.06       |
| $\text{AB}/\text{AB}^-$          | -3.12           | -1.73                                    | 0.26                         | 0.17             | 70.89        |
| $\text{AB}^-/\text{AB}^{2-}$     | -2.25           | -2.60                                    | 0.26                         | 0.21             | 48.04        |
| $\text{TTF}/\text{TTF}^+$        | -4.48           | -0.37                                    | 0.28                         | 0.14             | 73.79        |
| $\text{TTF}^+/\text{TTF}^{2+}$   | -5.44           | 0.59                                     | 0.28                         | 0.42             | 4.84         |
| $\text{TH}/\text{TH}^+$          | -5.19           | 0.34                                     | 0.26                         | 0.05             | 209.16       |
| $\text{TH}^+/\text{TH}^{2+}$     | -6.27           | 1.42                                     | 0.26                         | 0.36             | 10.24        |

To understand the electrochemical behavior of CFE and the reference reactions, we performed numerical simulations of electrochemical processes using the finite difference method as described in Section 2.2.1. This approach was previously described in the literature.<sup>110,113,244</sup> One of the parameters utilized in the model is the diffusion constant ( $D_i$ ) that was calculated using the Einstein-Stokes equation:

$$D_i = \frac{k_b T}{6\pi\eta a_i} \quad (3.5)$$

where  $k_b$  is the Boltzmann constant,  $\eta$  is the solvent viscosity and  $a_i$  is the radius of the molecule. The viscosity of acetonitrile at 298.15 K equals to 0.38 mPa·s.<sup>176</sup> Thus, the calculated diffusion coefficients are  $0.954 \times 10^{-5}$  and  $0.951 \times 10^{-5}$  cm<sup>2</sup>/s for  $\text{Fc}^0$  and  $\text{Fc}^+$ , respectively. This fits well with experimentally obtained values of  $2.00 \times 10^{-5}$  and  $1.60 \times 10^{-5}$  cm<sup>2</sup>/s for  $\text{Fc}^0$  and  $\text{Fc}^+$ , respectively.<sup>162</sup>

Figure 15 shows the comparison of experimental<sup>245</sup> and simulated CVs of the  $\text{Fc}^0/\text{Fc}^+$  system.

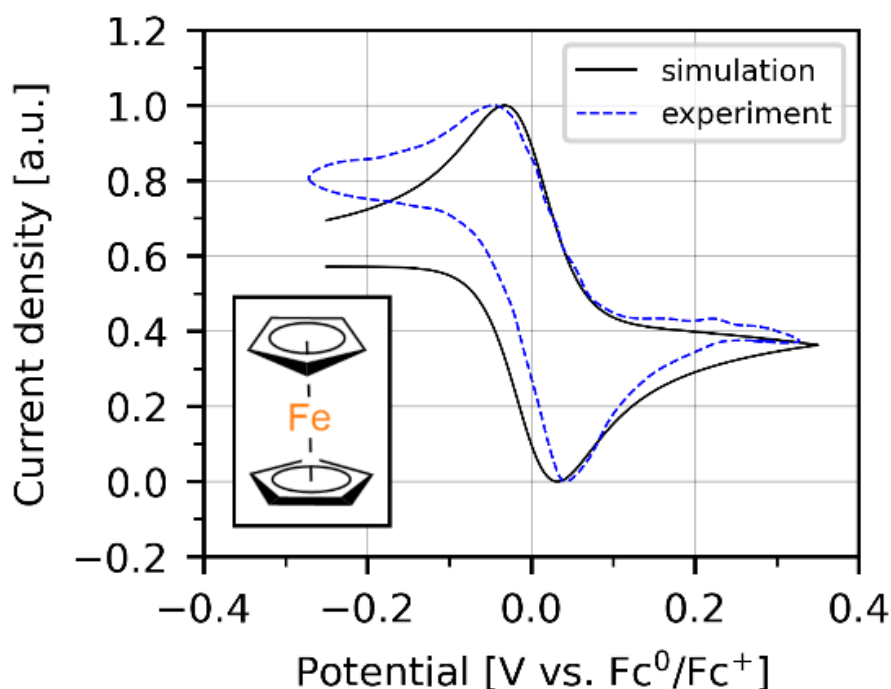


**Figure 15.** Experimental and simulated CV curves of 5 mM ferrocene oxidation at 0.01 V/s scan rate. Solid line represents simulated CV, dashed line represents experimental CVs (see text). The provided values represent simulated/experimental peak potentials and standard reduction potentials. Reproduced from ref. 214. Available under a CC BY-NC-ND 4.0 license. Copyright 2024 Kramarenko A.S., Sharapa D.I., Pidko E.A., Studt F.

Concentrations of all components of the reaction medium in simulations were set to reproduce the experimental conditions. In the simulation of the ferrocene behavior, the equilibrium potential was established at 0 V vs.  $\text{Fc}^0/\text{Fc}^+$ , and the positions of peak potentials exhibited slight variations compared to the experimental results, with the peak potential difference being 0.06 V for our simulation and 0.08 V for experimental results.<sup>245</sup> We can thus nicely simulate the CV of our CFE using exclusively input from DFT calculations as well as the tabulated viscosity of acetonitrile as the input.

Using our CFE simulation we can now focus on the study of the reference reactions. The cases where experimental CVs were found are summarized in Figure 16.

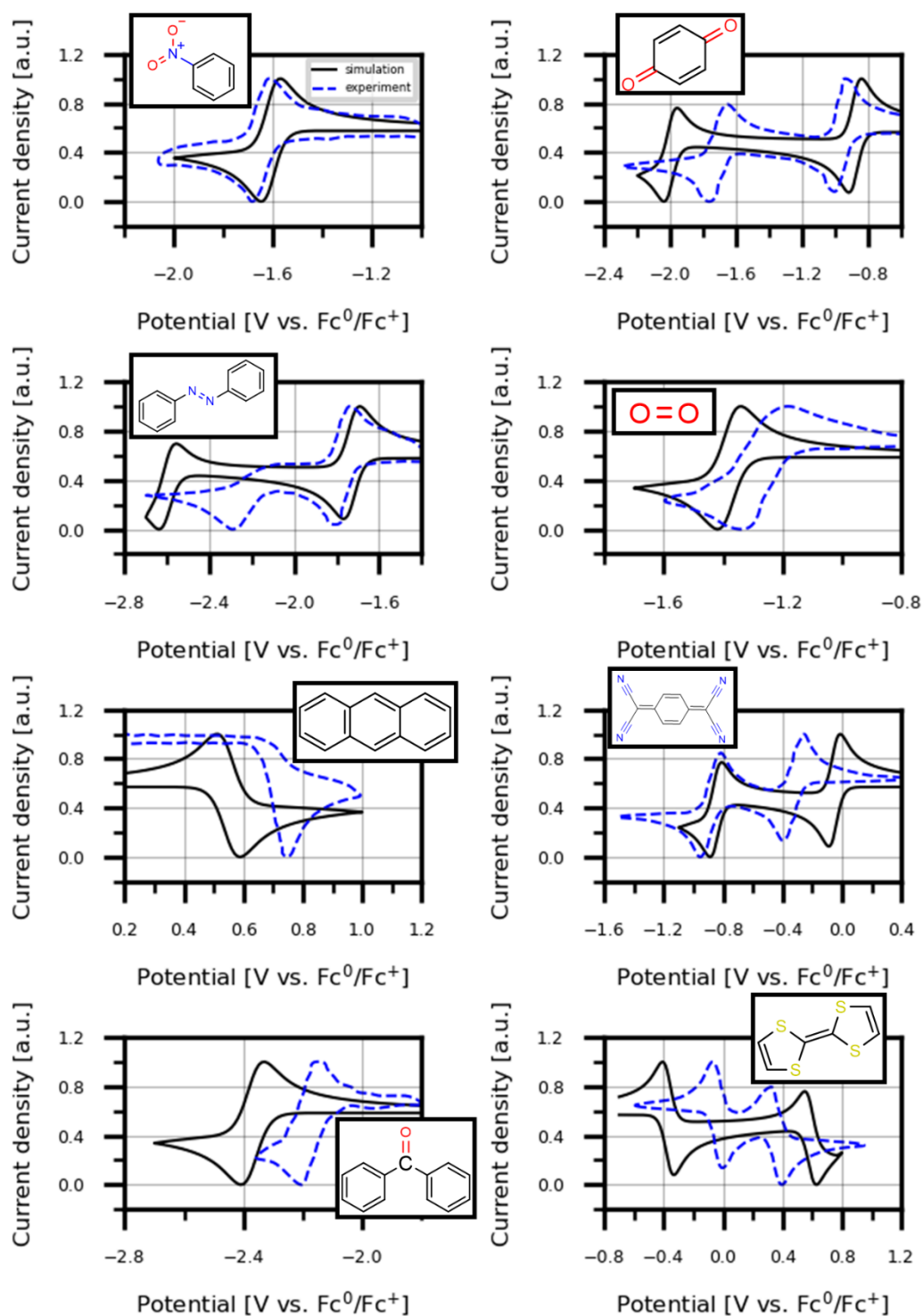


**Figure 16.** Experimental (dashed blue line) and simulated (solid black line) CV curves of electron transfer for some studied electrochemical systems noted in Figure 11. The current density is represented in arbitrary units to neglect the deviation in experimental and computed (via Equation 3.5) diffusion coefficients. Scan rates for simulations were set uniformly to 0.1 V/s to reproduce experimental conditions.

Figure 16 includes experimental CVs adapted from published experimental works.<sup>170,221,222,224,226,229–233,246</sup> In all cases shown in Figure 16, all deviations from the experimentally observed reaction behavior can be explained by the difference in experimental<sup>113,229,233,237</sup> and predicted equilibrium potentials ( $E^0$ ). However, the experimental anthracene oxidation does not show the cathodic peak from the cation radical deactivation which was observed for anthracene derivatives on the Pt electrode.<sup>247</sup> This might be related to the chemical step which was not considered in the current model. This process was shown to be the fast step<sup>248</sup>, hence the reversed process of  $An^+$  reduction is hindered due to lack of cation radicals.<sup>249</sup> The experimental approach for estimating kinetic parameters of a reversible electrochemical process relies on the Nicholson's method, employing an empirical Equations 3.6.<sup>113,168,206</sup>

$$\Psi = \frac{(-0.6288 + 0.0021\Delta E^p)}{(1 - 0.017\Delta E^p)}, \quad (3.6)$$

the standard rate constant can be computed as following:

$$\Psi = \frac{(D_O/D_R)^{\beta/2} k^0}{\left(\frac{\pi D_O F v}{RT}\right)^{1/2}} \quad (3.7)$$

where  $D_O$  and  $D_R$  are diffusion coefficients of reduced and oxidized species and  $\beta$  is symmetry parameter of the Butler-Volmer model.

From simulation results we can see that  $\Delta E^p$  is well reproduced for the reversed processes (Table 3), however in the case of quasi-reversible processes ( $\Delta E^p > 80$  mV), the Marcus-Hush model is unable to predict correctly the electrochemical behavior. Thus, for such processes more advanced models can be used that are taking into account reaction asymmetry.<sup>110,129,140,142,153</sup> When examining experimental rate constants, the assumption was made that the  $\beta$  parameter is uniformly set to 0.5 for all reversible processes. Rate constants calculated by the abovementioned method are summarized in Table 4.

**Table 4.** Rate constants of some reference reactions obtained by the Nicholson method from experimental CVs ( $k_{BV}^0$  exp.) and from simulated CVs ( $k_{BV}^0$  calc.).

| Reaction       | $\Delta E^p$ exp. [V] | $\Delta E^p$ calc. [V] | $k_{BV}^0$ exp. [cm/s] | $k_{BV}^0$ calc. [cm/s] |
|----------------|-----------------------|------------------------|------------------------|-------------------------|
| $Fc^0/Fc^+$    | 0.08                  | 0.06                   | 0.004                  | 0.085                   |
| $BQ/BQ^-$      | 0.20                  | 0.08                   | 0.001                  | 0.015                   |
| $BQ^-/BQ^{2-}$ | 0.12                  | 0.08                   | 0.004                  | 0.015                   |
| $BP/BP^-$      | 0.07                  | 0.08                   | 0.026                  | 0.013                   |

**Table 4.** Rate constants of some reference reactions obtained by the Nicholson method from experimental CVs ( $k_{BV}^0$  exp.) and from simulated CVs ( $k_{BV}^0$  calc.) (cont.).

|                                       |      |      |       |       |
|---------------------------------------|------|------|-------|-------|
| $O_2/O_2^-$                           | 0.12 | 0.08 | 0.005 | 0.018 |
| NB/NB <sup>-</sup>                    | 0.10 | 0.08 | 0.007 | 0.014 |
| TCNQ/TCNQ <sup>-</sup>                | 0.15 | 0.08 | 0.002 | 0.013 |
| TCNQ <sup>-</sup> /TCNQ <sup>2-</sup> | 0.21 | 0.08 | 0.001 | 0.013 |
| An/An <sup>+</sup>                    | -    | 0.08 | -     | 0.013 |
| AB/AB <sup>-</sup>                    | 0.05 | 0.08 | 0.261 | 0.013 |
| AB <sup>-</sup> /AB <sup>2-</sup>     | 0.10 | 0.08 | 0.006 | 0.013 |
| TTF/TTF <sup>+</sup>                  | 0.08 | 0.08 | 0.014 | 0.014 |
| TTF <sup>+</sup> /TTF <sup>2+</sup>   | 0.07 | 0.08 | 0.027 | 0.014 |
| TH/TH <sup>+</sup>                    | -    | 0.08 | -     | 0.015 |
| TH <sup>+</sup> /TH <sup>2+</sup>     | -    | 0.08 | -     | 0.015 |

Our approach qualitatively reproduces the magnitude of the rate constant and can be employed for investigating the thermodynamics and kinetics of electrochemical processes.

Furthermore, by comparing the experimental peak potentials with the simulated values, we can evaluate the reproduction of kinetic parameters. We also stress here, that the discrepancies are mostly due to errors originating from inaccuracies of the DFT functional, as an error of e.g. 0.2 eV translates directly into a deviation of 0.2 V in the CV.

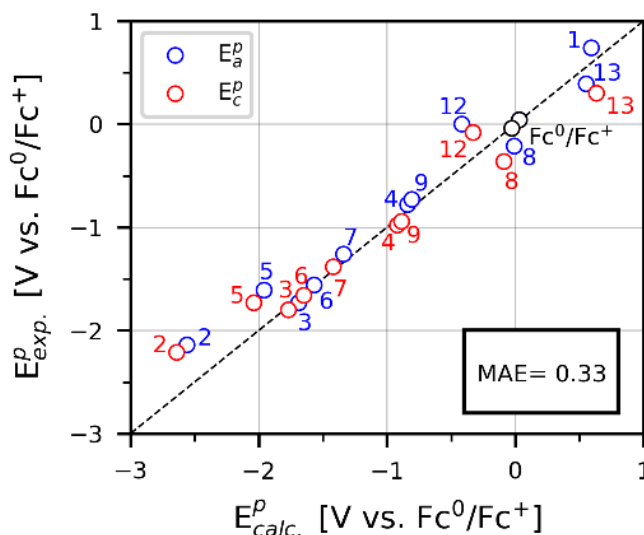


**Figure 17.** Representation of accuracy for peak potential prediction by the Marcus-Hush model.  $E_a^p$  and  $E_c^p$  are anodic and cathodic peak potentials, respectively. Numbers denote the reaction indexes from Figure 11. Reproduced from ref. 214. Available under a CC BY-NC-ND 4.0 license. Copyright 2024 Kramarenko A.S., Sharapa D.I., Pidko E.A., Studt F.

Figure 17 illustrates a comparison between the experimental and simulated peak potentials for investigated test reactions for which experimental CVs have been found. The analysis indicates that the predicted peak potentials align well with the experimental results, within the typical error introduced by DFT. The mean average deviation for the model was estimated to be 0.33 V vs.  $\text{Fc}^0/\text{Fc}^+$ . Significant deviations from experimental results were primarily observed, when computational errors in reduction potentials existed.

### 3.4 Summary and Conclusion

In conclusion, our study digs into the determination of absolute electrode potentials, reduction potentials, and electrode reaction kinetics for the reference reaction and the ferrocene/ferrocenium system in particular. The assessment of various density functional theory functionals revealed that UKS calculations consistently underestimate the ionization energy, especially for functionals with a high proportion of Hartree-Fock exchange. Transitioning to the ROKS approach rectifies this issue, aligning ionization energies more closely with experimental values, particularly for the PBE and M06 functionals.

In the realm of reduction potentials, the study demonstrated that the ROKS approach provides more accurate predictions across various functionals compared to UKS calculations. The M06 functional emerged as the most precise predictor, with a mean average deviation falling within the typical range of DFT errors. This precision in reduction potential predictions is crucial for understanding electrochemical reactions.

Moving beyond potential energies, our investigation extended to electrode reaction kinetics. Utilizing the Marcus-Hush model, we calculated activation energies for reference reactions, shedding light on the electron transfer process. The M06 functional stood out as providing the most accurate predictions for reduction potentials, facilitating precise calculations of activation energies.

Furthermore, the study employed CV simulations to gain insights into the electrochemical behavior of the reference reactions and  $\text{Fc}^+/\text{Fc}^0$  system. The model, validated against experimental data, showcased its utility in predicting peak potentials and current density responses. While deviations were observed, particularly in reduction potentials impacting peak potentials, the model provided a qualitative representation of electrochemical processes.

In summary, our comprehensive investigation involving absolute electrode potentials, reduction potentials, electrode reaction kinetics, and cyclic voltammetry simulations

contributes valuable insights into the computational precision of various DFT functionals for the  $\text{Fc}^+/\text{Fc}^0$  system. The findings emphasize the importance of selecting appropriate functionals for accurate predictions in different electrochemical contexts, laying the groundwork for more informed studies in the field of electrochemistry.

## 4. Dissociative Electron Transfer Kinetics in Benzyl Halides

### Electrocarboxylation

This chapter is based on [Kramarenko, A. S.; Sharapa, D. I.; Pidko, E. A.; Studt, F. Kinetics of Dissociative Electron Transfer in Electrocarboxylation of Benzyl Chloride. 2024, *In preparation*]

Electrocarboxylation is an electrochemical process that introduces carboxylic acids functional groups into organic substrates, with benzyl halides being particularly notable due to their accessibility and versatility. This process represents a sustainable method for synthesizing carboxylic acids while reducing the need for hazardous reagents.<sup>250–257</sup>

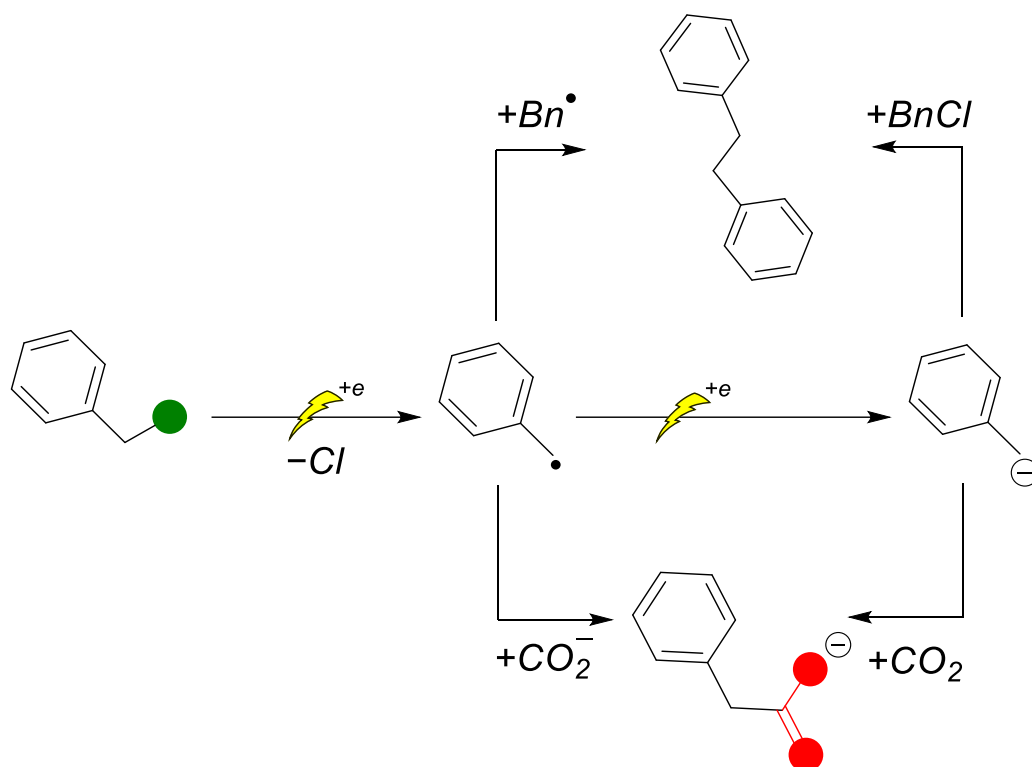
The mechanism often involves dissociative electron transfer (DET),<sup>258–262</sup> where the benzyl halide undergoes one-electron reduction to form a radical anion,<sup>257,263–265</sup> which then fragments or reacts with carbon dioxide to yield the carboxylic acid product. The kinetics of DET in benzyl halides is crucial for optimizing reaction conditions and enhancing yields.<sup>52,266</sup>

Factors such as the electronic properties of the halogen substituent, solvent effects, and supporting electrolytes significantly influence the rate of electron transfer and the stability of radical intermediates. In this section, we aim to investigate this kinetics, providing insights into the mechanistic aspects of electrocarboxylation and contributing to the development of more efficient and environmentally friendly synthetic methods for carboxylic acids and their derivatives.<sup>213,250,251,253,266–273</sup>

### 4.1 Electrochemical reduction of Benzyl Halides

In this section, we utilize the previously developed method for calculating the free energy of electron transfer at any given potential by focusing on an electrochemical reaction that involves only electron transfer steps, using the CHE reference. Additionally, we demonstrate how Marcus theory<sup>148,239,274–278</sup> can be employed to calculate reaction barriers for these electron transfer steps in a simple and computationally efficient way. As a test case, we selected the electrochemical activation of benzyl chloride (BnCl) followed by CO<sub>2</sub> fixation in aprotic acetonitrile (see Scheme 2), as this process occurs in the liquid phase without the need for adsorption into a solid electrocatalyst and is considered as a promising, sustainable approach for carbon cycle optimization and halogenated pollutant remediation.<sup>52,57,73,90,92,98,148,211,239,275,278–282</sup>





**Scheme 2.** Schematic representation of electrochemical carboxylation of benzyl chloride consisting of two-electron transfer, with chemical steps and CO<sub>2</sub> electrochemical activation producing phenylacetate as a target product.

We employed the M06 functional combined with the ma-def2-TZVPP basis set as implemented in the ORCA code (version 5.0.3). The procedure followed in this study is based on methods reported in Section 3. To account for the solvation effects of the acetonitrile medium, the CPCM solvation model was utilized.

Although the reaction is known to be influenced by the choice of the cathode material<sup>58,71,75,98,147,212,283</sup>, our focus here is on using an inert electrode, such as glassy carbon (GC), which has been demonstrated to facilitate the reaction without requiring intermediate adsorption.<sup>147,148</sup> This concept is supported by previous molecular dynamics simulations, which revealed the formation of a dense solvation layer on the electrode surface<sup>91</sup> that prevents direct interaction between the organic halide and the electrode. The electron transfer occurs from the electrode, across the electric double layer (EDL), to the BnCl via an outer-sphere electron transfer (OSET) mechanism (see Figure 18).<sup>113,284,285</sup> Recent studies have shown that the EDL density varies with applied potential, particularly as cation concentration increases. Typical EDLs range from 0.5 to 30 nm in thickness.<sup>131,286,287</sup>

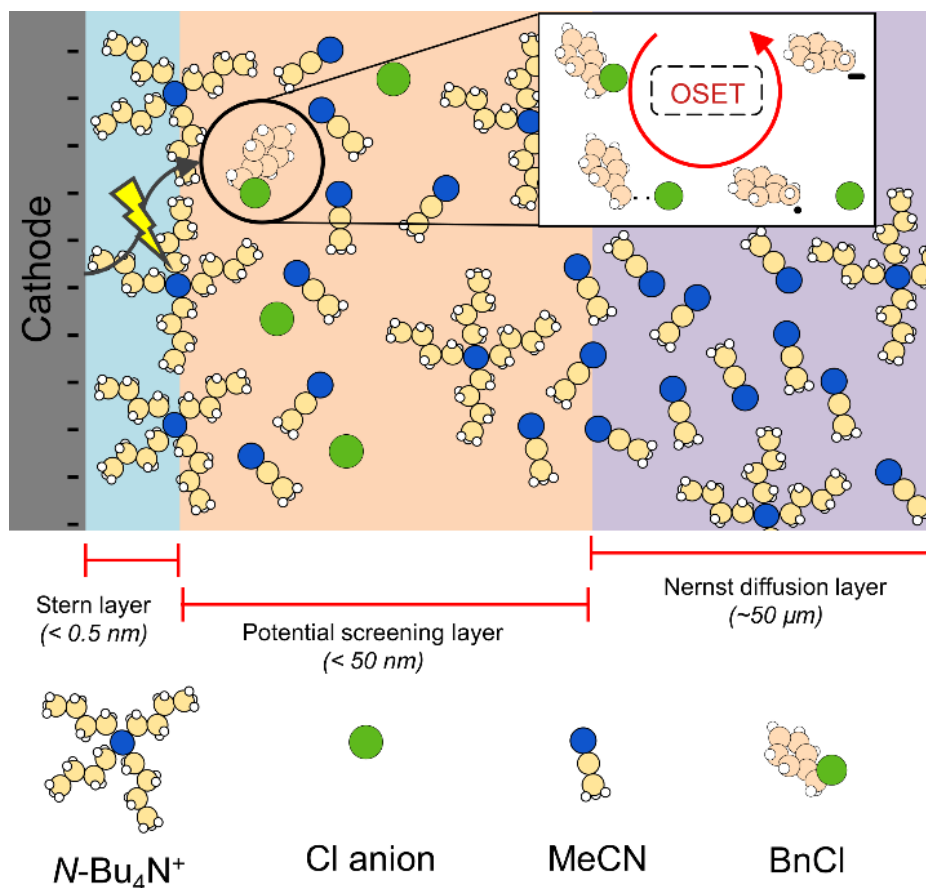
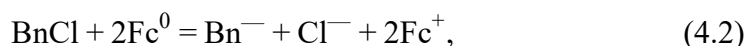
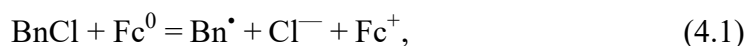


**Figure 18.** Schematic description of benzyl chloride electroreduction over a glassy carbon electrode through an electron transfer from the cathode to the bulk solution via an outer-sphere electron transfer mechanism.

We introduce a method for calculating free energy changes during electron transfer as a function of potential, drawing inspiration from the computational hydrogen electrode method used for proton coupled electron transfer steps. This approach enables us to analyze the thermodynamics of the electrochemical reactions in Scheme 2 in relation to the applied potential, allowing us to evaluate the likelihood of different reaction pathways.

The thermodynamics of the two electron transfer steps are thus calculated according to Equations 4.1 and 4.2.



The free energy change of the electron transfer process,  $\Delta G_{\text{ET}}$ , at a given potential is than easily obtained by

$$\Delta G_{\text{ET}} = G_{\text{Fc}^+} - G_{\text{Fc}^0} + neU, \quad (4.4)$$

here  $G_{\text{Fc}^+}$  and  $G_{\text{Fc}^0}$  represent the free energies of  $\text{Fc}^+$  and  $\text{Fc}^0$ , respectively, while  $e$  denotes the elementary charge,  $U$  is the applied potential, and  $n$  is the number of transferred electrons. It is important to note that we assume the reduction occurs in the liquid phase within the electric double layer (EDL), with no adsorbed species at the electrode surface during this process. The free energy diagram illustrating the electroreduction of  $\text{BnCl}$ , derived from this model and our DFT calculations of various intermediates in solution (utilizing a CPCM model), is presented in Figure 19 for different applied potentials ( $E$ ) relative to the  $\text{Fc}^0/\text{Fc}^+$  couple.

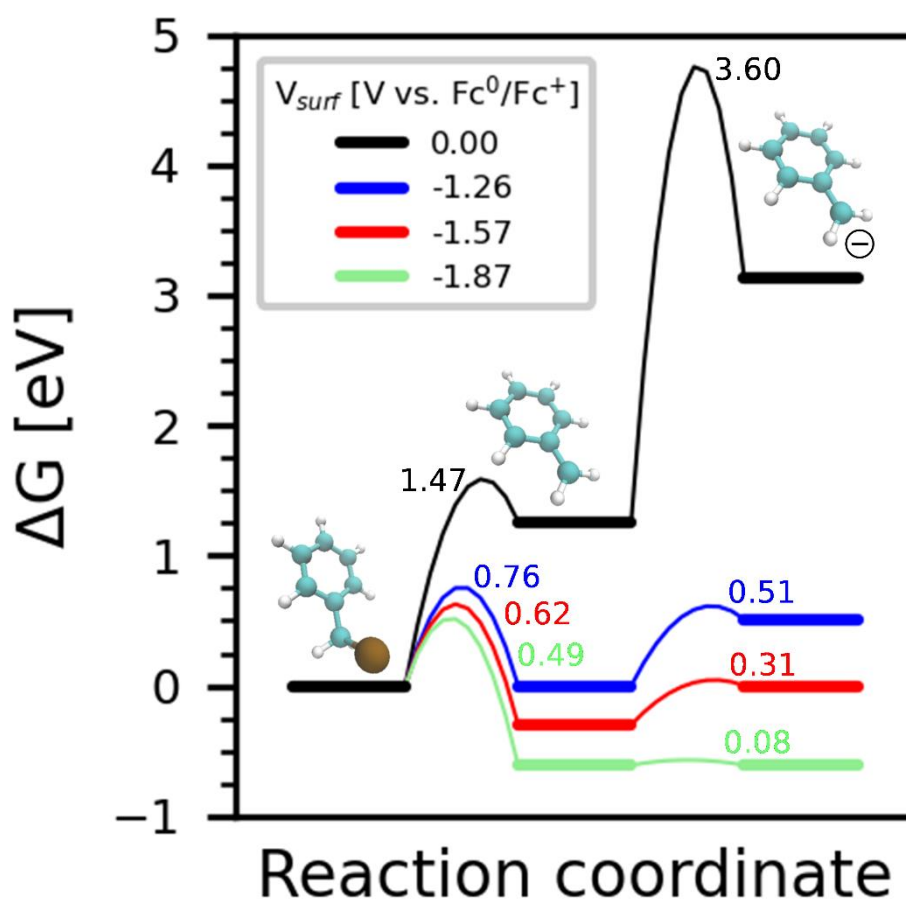


**Figure 19.** Free energy diagram of the electroreduction of benzyl chloride to benzyl radical at standard conditions given at various potentials vs  $\text{Fc}^0/\text{Fc}^+$  as obtained from our electron transfer model. Reaction free energy barriers as obtained through calculations using Marcus theory at the various potentials (Equation 2.28).

As illustrated in Scheme 2, the electrochemical activation of  $\text{BnCl}$  begins with the cleavage of the C-Cl bond and the formation of the benzyl radical at a reduction potential (SRP) of -1.26 V vs.  $\text{Fc}^0/\text{Fc}^+$ , which is very close to the experimental SRP value of -1.22 V vs.

$\text{Fc}^0/\text{Fc}^+$ .<sup>239</sup> The second electron transfer becomes thermoneutral with respect to the BnCl molecule at the SRP of -1.56 V vs.  $\text{Fc}^0/\text{Fc}^+$ . However, this step remains unfeasible at this potential. Instead, the second electron transfer occurs at a more negative potential of -1.87 V vs.  $\text{Fc}^0/\text{Fc}^+$ , which matches the experimental SRP value<sup>58,211</sup> for the second electron transfer. The final step, the formation of phenylacetate, is a thermochemical step that does not depend on the applied potential.

Using Marcus theory, we calculated the activation barriers for the electron transfer steps involved in the electroreduction of BnCl and  $\text{CO}_2$  activation. As anticipated, the barriers decrease with increasing exothermicity of the reaction step, which corresponds to more negative potentials. Notably, for BnCl activation, the activation barriers for the first and second electron transfer steps are 0.83 eV and 0.08 eV, respectively, for the standard equilibrium potentials of -1.26 V and -1.87 V vs.  $\text{Fc}^0/\text{Fc}^+$ , where the corresponding reaction steps become thermoneutral. These barriers correspond to reaction rates of approximately  $6.3 \times 10^{-11}$  and  $2.2 \times 10^2$  cm/s at 298.15 K, respectively (Table 4).

**Table 4.** Computed thermodynamic ( $E^0$  via Equation 2.29) and kinetic parameters ( $k^0$  via Equation 2.35) of electrochemical steps used in electrochemical response simulations. Reorganization energies were calculated using Equations 2.30 and 2.31.

| Reactions  | $E^0$ [V vs. $\text{Fc}^0/\text{Fc}^+$ ] | $\lambda_{\text{solv}}$ [eV] | $\lambda_{\text{i}}$ [eV] | $\lambda_{\text{tot}}$ [eV] | $k^0$ [m/s]            |
|--|--|------------------------------|---------------------------|-----------------------------|------------------------|
| $\text{BnCl} + \text{e} = \text{Bn}^{\bullet} + \text{Cl}^-$ | -1.26                                    | 0.30                         | 3.00                      | 3.30                        | $6.33 \times 10^{-13}$ |
| $\text{Bn}^{\bullet} + \text{e} = \text{Bn}^-$               | -1.87                                    | 0.32                         | 0.03                      | 0.35                        | 2.18                   |
| $\text{CO}_2 + \text{e} = \text{CO}_2^{\bullet-}$            | -2.86                                    | 0.43                         | 1.63                      | 2.06                        | $1.86 \times 10^{-7}$  |

This observation supports the assumption underlying the CHE model that a reaction is more likely when the free energy of the reaction step is at least thermoneutral.

Figure 20 illustrates the calculated barrier heights as a function of applied potential and exothermicity. We analyzed three reactions within a reorganization energy range of 0 to 3.30 eV to highlight the observed trends. It is clear that the slope of the activation energy curve is significantly affected by the value of the reorganization energy (see Figure 20a). Since the reorganization energy is composed of two components, and the solvent's reorganization energy typically does not exceed 0.5 eV, the primary contribution comes from the internal reorganization (change in bond lengths and angles), which depends on the nature of the reagent.

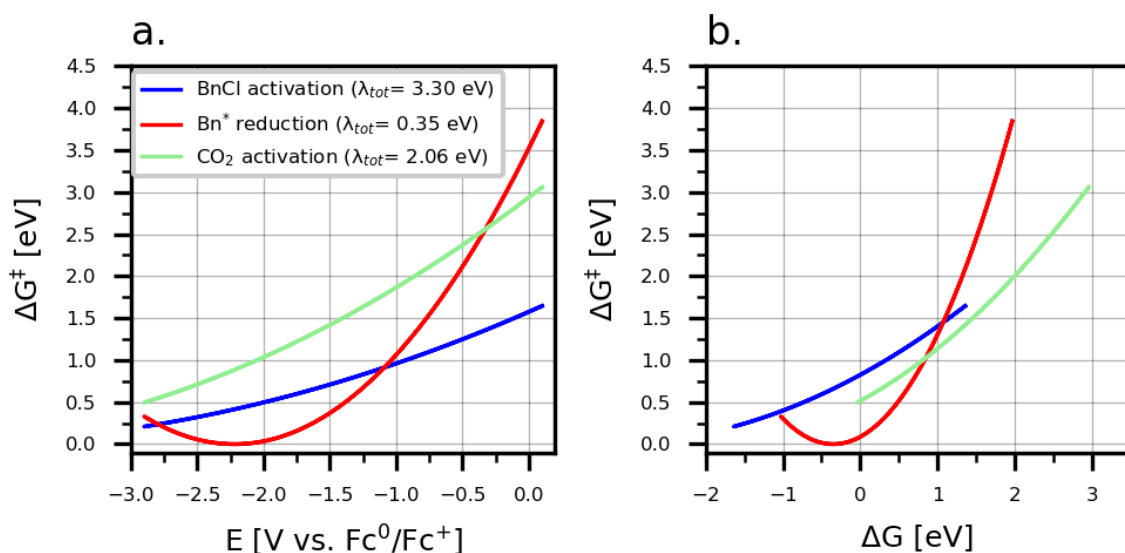


**Figure 20.** Computed activation energy dependence of benzyl chloride (blue line), benzyl radical (red line), and  $\text{CO}_2$  (green line) electroreduction on applied potential (a) and reaction free Gibbs energy change (b). The chosen electrochemical reactions cover the reorganization energy range from 0.35 to 3.3 eV.

Now, having Figure 20, it is possible to predict the potential dependent activation barrier of an electron transfer, approximating the reorganization energy for any system. It is useful for experimentalist to compare and assess kinetic parameters of several reactions by modulating the total reorganization energy of their systems.

Figure 20b shows the activation energy plotted against the free energy change of the reactions within the potential range of 0.1 to -2.9 V vs.  $\text{Fc}^0/\text{Fc}^+$ . It is clear that  $\text{CO}_2$  activation requires very negative potentials. Therefore, under standard experimental conditions, the formation of  $\text{BnCO}_2^-$  occurs exclusively through the interaction of  $\text{Bn}^-$  with neutral  $\text{CO}_2$  molecules.

Considering  $\text{CO}_2$  activation, we assume in this study that this process is reversible because attaching an excess electron to the  $\text{CO}_2$  molecule it only changes the OCO angle from 180 to 120 deg. Without a coupling agent, it is expected that the electron can be returned and since  $\text{CO}_2$  does not undergo bond splitting like in the case of BnCl, it is likely that  $\text{CO}_2$  activation is a reversible process.

Having all necessary kinetic properties of  $\text{CO}_2$  activation, we computed the cyclic voltammetry response using the finite elements method<sup>132,288–292</sup> by the COMSOL Multiphysics (version 6.1) software.

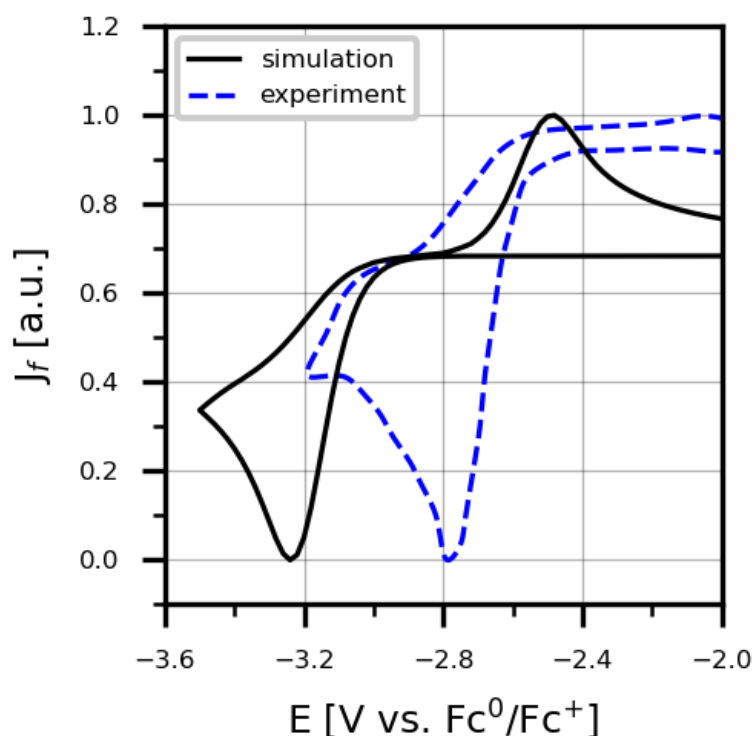
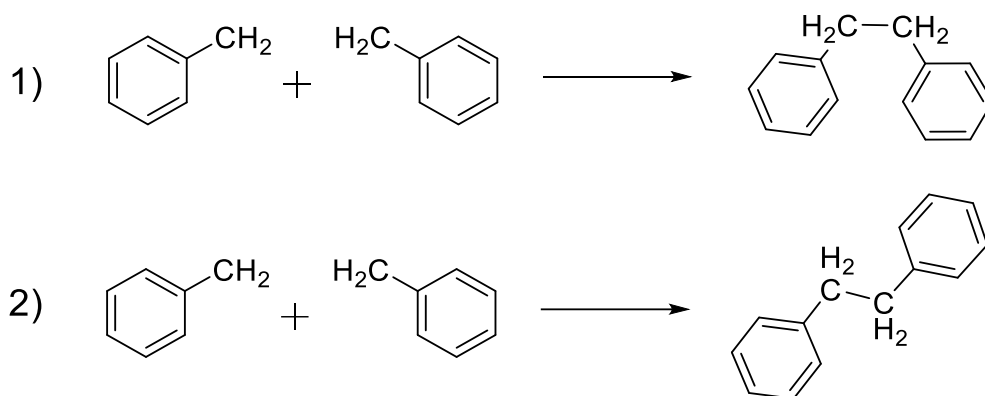


**Figure 21.** Electrochemical response of simulated (black line) and experimental<sup>211</sup> (blue line) CO<sub>2</sub> electrochemical activation at the inert and Ag electrodes, respectively.

Figure 21 shows the simulated and experimental CV responses of CO<sub>2</sub> electroreduction. The main mismatch between simulation and experiment arises from our approximation of the process reversibility. Therefore, we can observe the current peak in the range -2.4 – -2.5 V vs. Fc<sup>0</sup>/Fc<sup>+</sup> from CO<sub>2</sub> deactivation. Another big difference between the simulation and the experiment comes from the mismatch of computed (-2.86 V vs Fc<sup>0</sup>/Fc<sup>+</sup>) and experimental<sup>13</sup> (-2.55 V vs. Fc<sup>0</sup>/Fc<sup>+</sup>) standard equilibrium potentials, which leads to the difference in position of peak potentials. This also might be connected to the electrocatalytic activity of the cathode material. However, previous theoretical studies show that outer-sphere electron transfer mechanisms are a possible scenario for the CO<sub>2</sub> electroreduction process.<sup>284</sup>

Additionally, the whole process depicted in Scheme 2 also includes thermochemical steps. Therefore, we also investigated the thermodynamics of these steps performing potential surface scans. Radical coupling reactions are shown in Scheme 3. We performed potential energy scans using C-C bond length as a descriptor.



**Scheme 3.** Schematic representation of two possible radical coupling pathways with two possible product conformers. Highlighted carbon atoms represent the atoms used in the distance constrain for the potential energy scan.

Analyzing Figure 22 it can be observed that radical the coupling reaction undergoes a barrierless process producing two possible conformers of biphenyl ethane (Scheme 3).

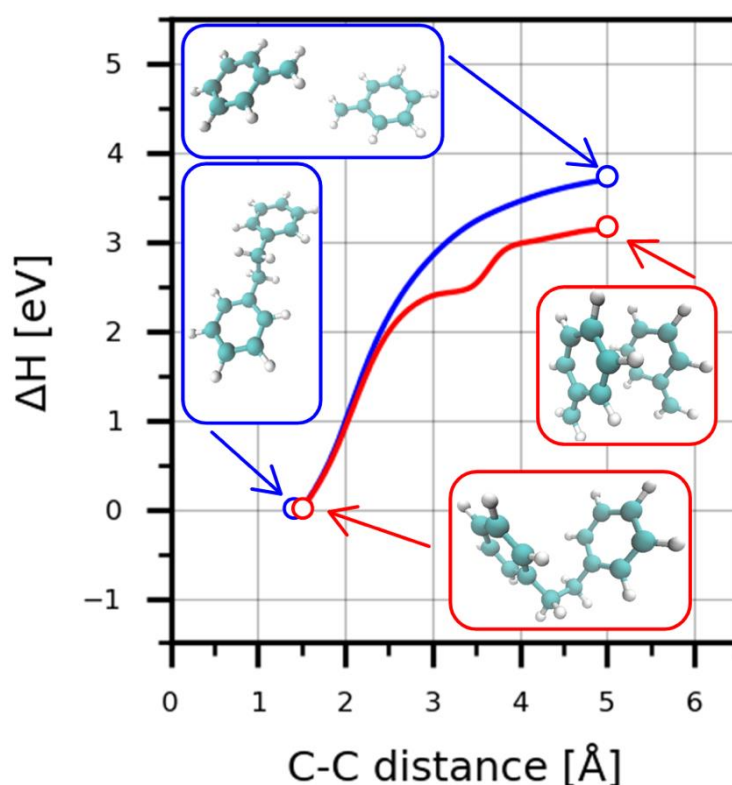
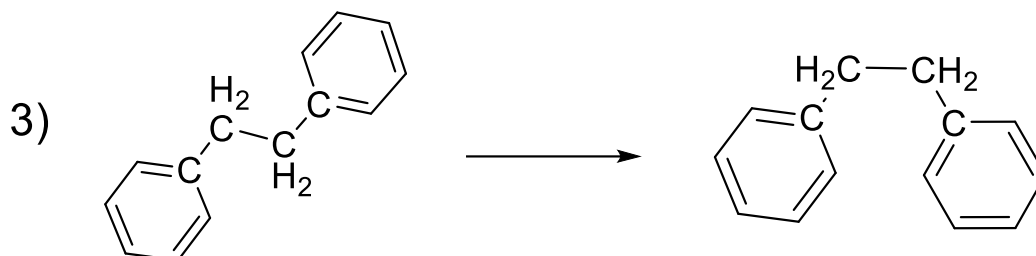


**Figure 22.** Relative energy dependence of radical coupling reaction described as a function of distance between two carbon atoms highlighted in Scheme 3. The blue and red lines denote two possible reaction paths from of Scheme 3. (Reaction 1: blue line, Reaction 2: red line) Optimized geometries of the initial and final states for both processes are shown in the figure with the corresponding color scheme.

As we mentioned before, radical coupling undergoes two possible pathways. Therefore, we computed the activation barrier of the conformer transition from one state to another. For this, also we computed the potential energy profile as a function of the dihedral angle between two aromatic rings (Scheme 4).



**Scheme 4.** Schematic representation of the isomerization reaction of biphenyl ethane. Highlighted carbon atoms construct the dihedral angle that was used as a constraint descriptor for the potential energy scan.

A summary of the studied potential energy scan for the isomerization process can be found in Figure 23.

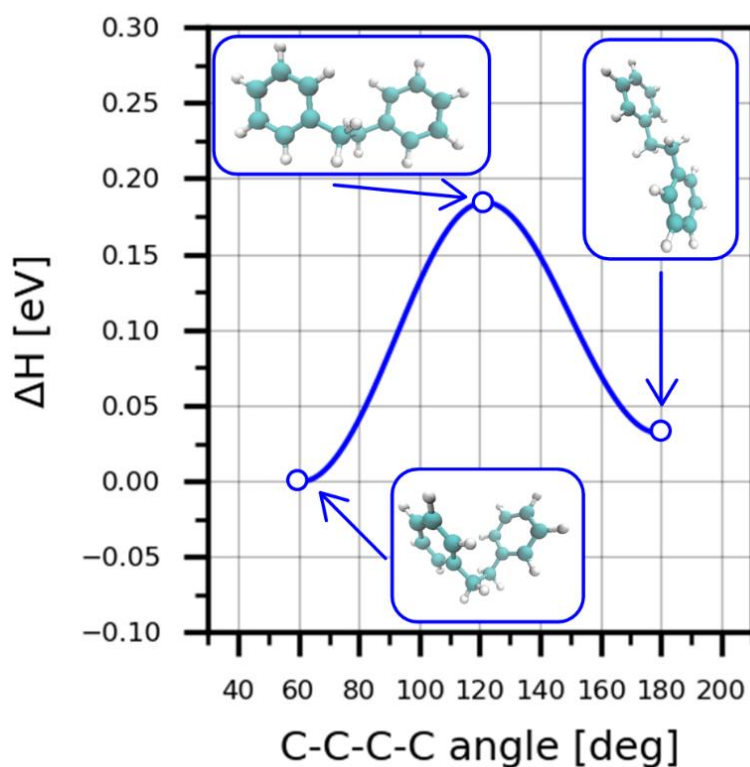
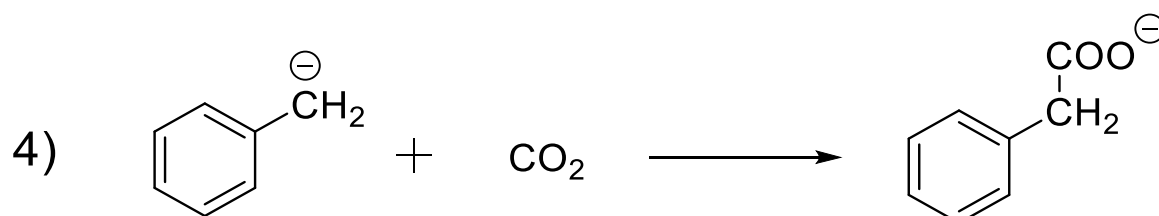


**Figure 23.** Relative energy dependence of the biphenyl ethane isomerization process as a function of the dihedral angle between the highlighted carbon atoms in Scheme 4. Optimized geometries of initial, final and transition state are shown in the figure.



Our findings show that there is one transition state in the process. Therefore, we computed the activation free energy of the isomerization process which is about 0.18 eV. Additionally, we show that the plane conformation of biphenyl ethane is less energetically favorable than the bent one.

Now, we will discuss the reaction thermodynamic properties of phenyl acetate anion formation by discussing the results of the potential energy scan.



**Scheme 5.** Schematic representation of benzyl anion radical coupling with CO<sub>2</sub> molecule. Highlighted carbon atoms represent the atoms used in the distance constrain for the potential energy scan.

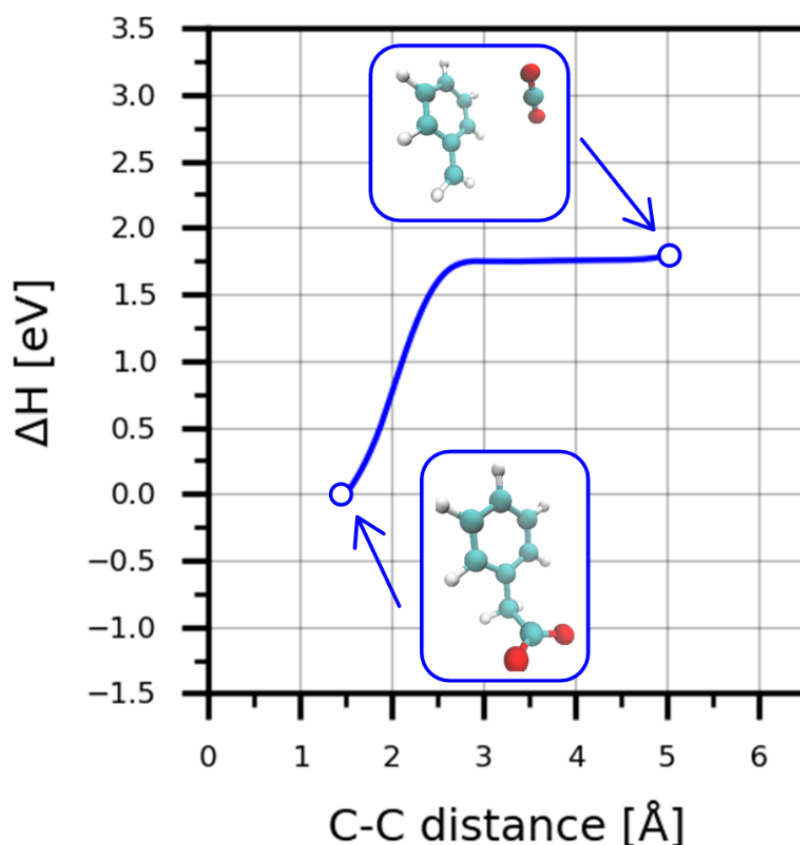
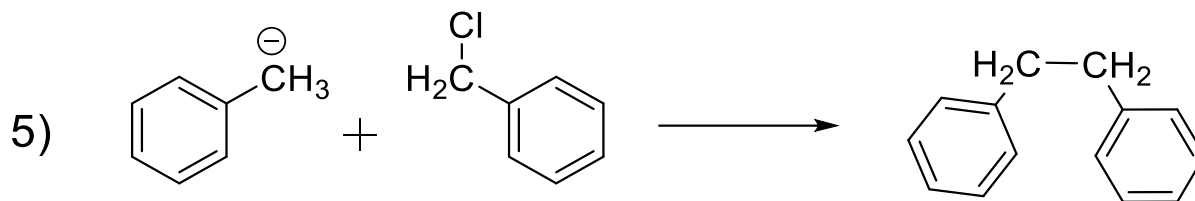


**Figure 24.** Relative energy dependence of benzyl anion radical coupling with the CO<sub>2</sub> molecule as a function of distance between the highlighted carbon atoms in Scheme 5. Optimized geometries of initial and final states are shown in the figure.

This result shows that this process is barrierless and can be described through collision theory.



Scheme 6. Schematic representation of benzyl anion radical coupling with the BnCl molecule. Highlighted carbon atoms represent the atoms used in the distance constrain for the potential energy scan.

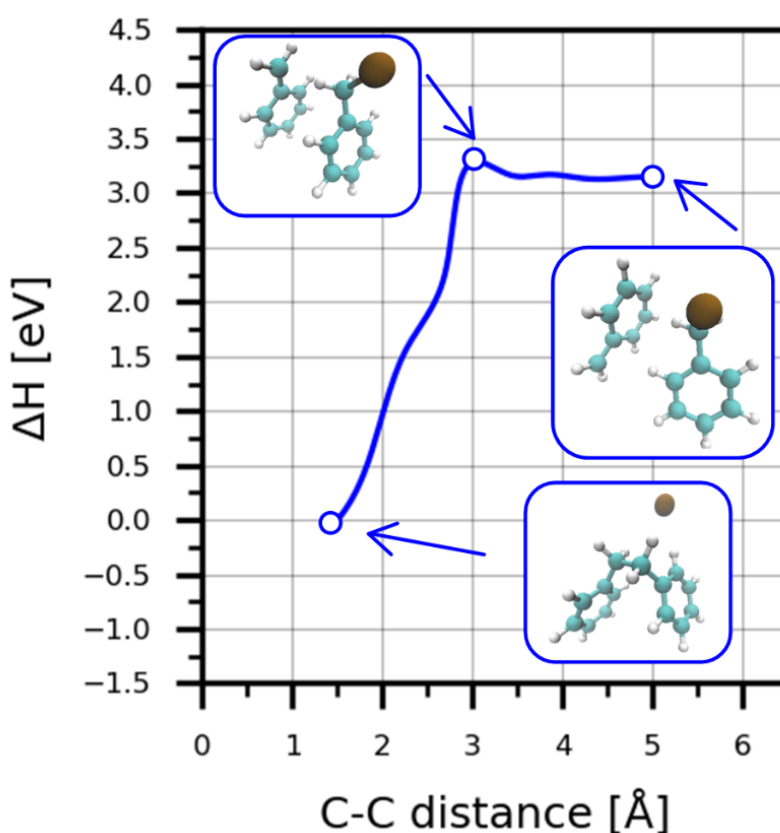


**Figure 25.** Relative energy dependence of benzyl anion radical coupling with the BnCl molecule as a function of distance between the highlighted carbon atoms in Scheme 6. Optimized geometries of initial, final and transition states are shown in the figure.

The reaction between BnCl and Bn anion undergoes  $S_N2$  mechanism with the activation barrier of 0.15 eV. Our results show that all thermochemical reactions taking place in our system can be divided in two groups, where an activation barrier was observed and where it was not (barrierless reactions). For the first group of reactions, rate constants were computed according to transition state theory (Equation 4.5).

$$k = \frac{k_B T}{h} e^{-\frac{\Delta G^\ddagger}{RT}}, \quad (4.5)$$

where  $k_B$  is the Boltzmann constant,  $T$  is the temperature,  $h$  is the Plank constant and  $\Delta G^\ddagger$  is the activation energy of the process.

For the second group of reactions, where the activation barrier was not observed, we utilized collision theory for the reaction rate calculation. Chemical reaction rate constants were computed according to the collision theory<sup>293</sup> via the following equation.

$$k = 4\pi N_A (D_a + D_b)(r_a + r_b)\sigma, \quad (4.6)$$

where  $N_A$  represents Avogadro's number,  $D_a$  and  $D_b$  are the reagents molecules diffusion coefficients,  $r_a$ ,  $r_b$  denote molecular radii of the reagents and  $\sigma$  is the spin statistical factor, which is equal of 0.25 and considers that only singlet encounters will lead to the reaction products.<sup>294</sup> The computed rate constants of thermochemical steps are summarized in Table 6.

**Table 6.** Rate constants of thermochemical reactions depicted in Scheme 2 calculated using transition state theory ( $k$  via Equation 4.5) for the reaction with an explicitly computed activation barrier and using the collision theory for the reaction where an activation barrier was not found ( $k$  via Equation 4.6).

| Reaction  | $k$ [mol/(m <sup>3</sup> ·s)] |
|---|-------------------------------|
| $2\text{Bn}^\bullet = \text{BnBn}$                      | $4.86 \times 10^6$            |
| $\text{Bn}^- + \text{CO}_2 = \text{BnCOO}^-$            | $4.97 \times 10^6$            |
| $\text{Bn}^- + \text{BnCl} = \text{BnBn} + \text{Cl}^-$ | 1.24                          |

Having all information about the elementary steps of the process, we perform complex multi-scale modelling of benzyl chloride electrocarboxylation.

## 4.2 Cyclic voltammetry simulation of Benzyl Chloride Electrocarboxylation

When comparing our theoretical results for the electrochemical two-electron reduction of  $\text{BnCl}$  to  $\text{Bn}^-$ , we generally observe that the reactivity trends align well with experimental data. We conducted a cyclic voltammogram (CV) simulation for both  $\text{BnCl}$  activation and the electrocarboxylation (EC) process. Figure 33 displays the experimental<sup>147</sup> and simulated CVs for  $\text{BnCl}$  activation, along with concentration profiles of the reaction species at key points during the simulation.

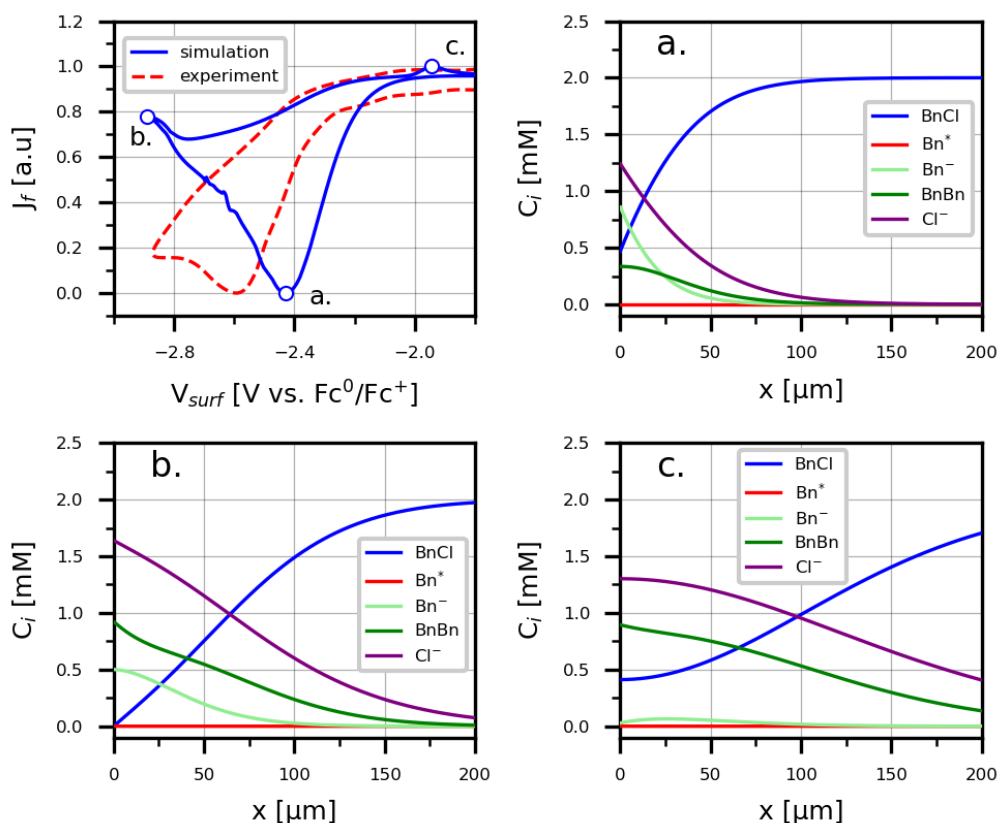


**Figure 26.** Comparison of experimental and simulated CVs of BnCl activation, with concentration profiles at various scan points. Electrode surface is assumed to be at 0  $\mu\text{m}$ . Initial concentration of BnCl of 2 mM and scan rate of 0.2 V/s were taken to be consistent with the experiment.<sup>147</sup>

Although our model underestimates the absolute value of the current density, the peak potential difference is approximately 0.2 V, corresponding to an energy difference of 0.2 eV, which falls within the error range of DFT methods<sup>214</sup>. Therefore, we conclude that our simulation results align well with the experimental findings. The simulation indicates that the first electron transfer is associated with a high activation barrier, which results in the simultaneous activation of BnCl and the reduction of the Bn radical.

Figure 26a displays the concentration profile of the reaction species at the peak potential, illustrating that the coupling of chemical radicals hinders the second electron transfer due to the absence of free Bn radicals, with a concentration of 0 mM. However, at this peak potential, the reduction of the Bn radical remains dominant, as indicated by the higher concentration of the Bn anion. As the potential decreases further, the activation energy for the second electron transfer is affected (see Figure 20a), which slows the reduction of the Bn radical. Consequently, the radical coupling process becomes more probable, leading to an almost twofold increase in BnBn concentration at the most negative potential in the simulation

(Figure 26b). Our simulation also revealed a peak for the oxidation of the Bn anion at approximately -1.9 V vs.  $\text{Fc}^0/\text{Fc}^+$ , which is not observed in the experimental CV scan. However, such a process has been reported in experimental studies of BnBr electroreduction on the Ag electrode surface.<sup>212</sup> This observation may be attributed to the greater difference between the standard reduction potentials for the first and second electron transfers for BnBr,<sup>91</sup> which increases the peak potential separation and makes the oxidation of the Bn anion more noticeable. At this point, the concentration of the Bn anion (see Figure 26c) drops nearly to 0 mM due to the chemical reactions taking place.

Figure 27 compares the simulated EC process with experimental results<sup>211</sup> obtained at the Ag electrode. The peak potential difference between the simulated and experimental CVs is approximately 0.4 V, which may be attributed to the influence of the electrode material on the process. Two characteristic peaks can be observed: one corresponding to the electroreduction of BnCl and the other to  $\text{CO}_2$  activation.

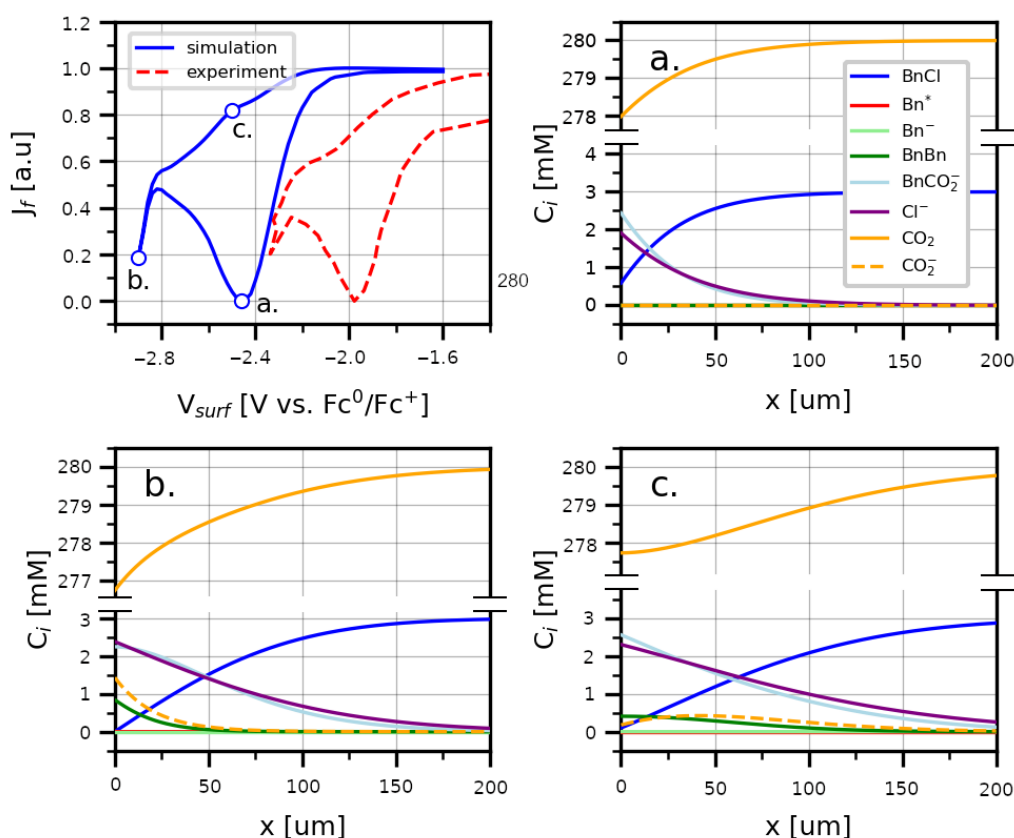


**Figure 27.** Comparison of experimental and simulated CVs of EC process, with concentration profiles at various scan points. Electrode surface is assumed to be at 0  $\mu\text{m}$ . Initial concentration of BnCl of 3mM, and  $\text{CO}_2$  is 280 mM ( $\text{CO}_2$  solubility in acetonitrile) and scan rate of 0.2 V/s were taken to be consistent with the experiment<sup>211</sup>.

Figure 27a presents the concentration distribution of the reaction reagents and products at the first peak potential of approximately -2.4 V vs.  $\text{Fc}^0/\text{Fc}^+$ . Our results indicate that at this potential, there is a simultaneous electrochemical reaction involving both the first and second electron transfers, linked to the interaction between the Bn anion and the  $\text{CO}_2$  molecule. The rate constant for this chemical step is  $4.97 \times 10^9 \text{ M}^{-1} \text{ s}^{-1}$ , which is slightly higher than that of the radical coupling reaction.

Despite this, the concentrations of Bn radical, Bn anion, and dibenzyl ethane all drop to 0 mM during the EC process, with  $\text{BnCOO}^-$  being the sole product. This contrasts with the BnCl activation process, where BnBn is the primary product. At more negative potentials (see Figure 34b), the production of Bn radical increases, leading to a rise in BnBn concentration up to 1 mM near the electrode surface. In this study, we did not account for the interaction between neutral  $\text{CO}_2$  and the  $\text{CO}_2$  anion, but we observed an increase in the concentration of free  $\text{CO}_2$  anions in the reaction system. Figure 27c depicts the concentration profile during  $\text{CO}_2$  deactivation, which in experimental work shows a slightly visible peak in the potential range between -2.0 and -1.8 V vs.  $\text{Fc}^0/\text{Fc}^+$ .

#### 4.4 Summary and Conclusion

In summary, we have developed a comprehensive method for calculating both the energetics and the kinetic barriers of electron transfer steps in electrochemical processes. This methodology has been successfully applied to investigate the electrochemical carboxylation of benzyl chloride (BnCl) to form  $\text{BnCO}_2^-$  in the aprotic solvent acetonitrile, providing a valuable framework for studying complex reaction mechanisms. Drawing inspiration from the CHE model, our approach calculates energetics using the  $\text{Fc}^0/\text{Fc}^+$  redox couple as a standard, enabling consistent comparison across different reaction conditions and materials.

To assess the electron transfer barrier heights for the transition from the electrode to the solvated molecule at the EDL, we employed Marcus theory, which is known for its accuracy in predicting reaction kinetics in electrochemical systems. However, we recognize that more rigorous computational methods would enhance the accuracy of these calculations by incorporating additional factors, such as dynamic solvent effects and specific electrode-molecule interactions. Our current methodology allows the computation of both energetics and kinetic barriers as a function of the applied potential, making it a powerful tool for tailoring electrochemical processes under various operational conditions.

Our results provide key insights into the mechanistic pathway of BnCl reduction to  $\text{BnCO}_2^-$ , aligning well with experimental findings in the literature, thereby validating our approach. This alignment with experimental data not only supports the reliability of our method but also emphasizes its applicability to similar electrochemical transformations.

Moreover, our study suggests that the electrochemical potential of electrons in electrode materials, particularly at the potential of zero charge, could serve as a critical descriptor for designing and selecting optimal electrode materials. This insight opens new avenues for targeted electrode engineering, as materials could be tailored based on their electronic properties to optimize reaction efficiency, selectivity, and stability.

Moving forward, future research should focus on refining this model to incorporate the nuanced effects of the electrode surface, such as atomic structure, roughness, and electronic properties, which could significantly impact reaction kinetics and selectivity. Furthermore, expanding this approach to coupled proton-electron transfer steps would allow for broader application in fields such as electrocatalysis and energy storage, where such reactions are common.

Overall, our work lays a robust foundation for understanding and advancing electrochemical transformations, providing tools and perspectives that will be instrumental in developing next-generation materials and processes for various applications in sustainable chemistry and energy conversion.

## **5. Surface Charging Effect on Outer-Sphere Electron Transfer: A Strong Dependence on Supporting Electrolyte Concentration**

This chapter is based on [Kramarenko, A. S.; Sharapa, D. I.; Pidko, E. A.; Studt, F. Surface Charging Effect on Outer-Sphere Electron Transfer: A Strong Dependence on Supporting Electrolyte Concentration. 2024, *In preparation*].

Supporting electrolyte plays an active role in electrochemical processes influencing the ionic conductivity of the solution and participates in EDL formation, which controls mobility of electroactive species in the region close to the electrode.<sup>91,131,243,284,286,295–299</sup> Variations in electrolyte concentration can alter the thickness and capacitance of the EDL, subsequently influencing the potential distribution and contribute rate, efficiency, and pathways of electrochemical reactions.<sup>208,209,295,300–305</sup> Understanding these interactions is crucial for optimizing reaction conditions in diverse applications, ranging from energy storage and conversion systems like batteries and fuel cells to electrolysis processes and electrochemical sensors.<sup>11,71,221–223,225,228,230,232–234,237,247,306</sup>

### **5.1 Model of Electric Double Layer Formation and Electron Transfer Kinetics simulation**

The surface charge and EDL structure influence the electrode material activity and dynamics of electrochemical reactions. In this way, the electrode's surface charge is compensated by the charge of specifically and non-specifically adsorbed ions, controlling the overall EDL electroneutral. Consequently, the dynamics and structure of EDL are influenced by the concentration of supporting electrolyte in the bulk solution.<sup>300,307–321</sup> Thus, modulating the concentration of supporting electrolyte one can significantly alter the rate, efficiency and pathway of electrochemical reactions.<sup>208,209,295,300–305</sup> Changes in the electrolyte concentration can alter the thickness and capacitance of the EDL, subsequently influencing the potential distribution and reaction kinetics at the electrode surface. A higher concentration usually enhances ionic conductivity of solution, reducing ohmic losses and stimulating more efficient current flow. In addition, the choice and concentration of the supporting electrolyte can affect the selectivity and mechanism of the electrochemical reactions. Different ions in the electrolyte can participate in side reactions, form complexes with the reacting species, or influence the adsorption of reactants and products on the electrode surface.<sup>12,295,309,322–329</sup> Investigation of



these processes is important for optimizing reaction conditions in various applications, such as energy storage, batteries and fuel cells, electrolysis processes and electrochemical sensors.

In previous chapters we discussed heterogeneous electron transfer through the lens of the OSET mechanism where the electron transfer occurs through the electron tunnelling from electronic state in the electrode to the energetic state in the reacting specie. In real systems, electron transfer reactions are happening in the electrode-electrolyte interface where EDL influences the reaction conditions. Influence of the EDL was firstly described by Frumkin modifying the Butler-Volmer approach.<sup>243</sup> Following his approach, we can rewrite Equation 2.32 and 2.33, modifying the activation energy term by adding the parameter that considers formation of the EDL on the electrode surface:

$$k_f = Z e^{\left( \frac{(\lambda - e_0 \eta)^2}{4\pi k_B T \lambda} \right)}, \quad (5.1)$$

$$k_b = Z e^{\left( \frac{(\lambda + e_0 \eta)^2}{4\pi k_B T \lambda} \right)}, \quad (5.2)$$

where  $Z$  is a prefactor depending on the molar mass of the reacting molecule assuming that the electron coupling between electrons in the electrode and reactant state is negligibly low (Equation 2.36),<sup>214</sup>  $\lambda$  is the reaction reorganization energy,  $e_0$  is the elementary charge, and  $\eta$  is the overpotential, which is the difference between applied potential ( $E$ ) and reaction equilibrium potential ( $E^0$ ):

$$\eta = E - E^0 - (\phi_{\text{OHP}} - \phi_{\text{Bulk}}), \quad (5.3)$$

with  $\phi_{\text{OHP}}$  being the electrostatic potential at the outer-Helmholtz plane (OHP) and  $\phi_{\text{Bulk}}$  being the reference potential in the bulk solution ( $\phi_{\text{Bulk}} = 0$  V) (Figure 28).

As we previously discussed in Chapter 3, applied potential ( $E$ ) is dependent on the electrochemical potential ( $\tilde{\mu}_e$ ) of electrons in the solid electrode:<sup>115</sup>

$$E = -\tilde{\mu}_e, \quad (5.4)$$

$$\tilde{\mu}_e = \mu_e - e_0 \phi_M, \quad (5.5)$$

where  $\mu_e$  is the chemical potential of electrode's electrons and  $\phi_M$  (Figure 28) is the electrostatic potential in the electrode surface produced by electrons and nuclei.  $E^0$  in this case is the free energy of the corresponding electrochemical reaction.

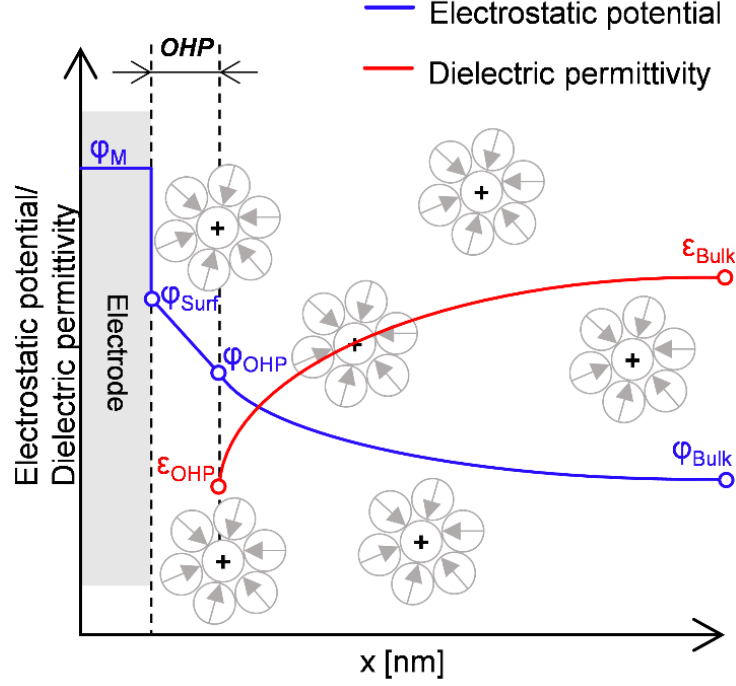


**Figure 28.** Schematic depiction of the electric double layer, showing the outer-Helmholtz plane (OHP), which indicates the distance of the closest approach for the solvated ions. The red and blue lines illustrate the distributions of the electrostatic potential and the dielectric permittivity, respectively.

In the electrolyte, the distribution of supporting electrolyte ions, reagents, products and their fluxes, as well as the electrostatic potential distribution are obtained by simultaneously solving the generalized modified Nernst-Planck and Poisson equations (Equations 5.6 and 5.7) using the finite elements method (Chapter 2.2.2).

$$\frac{\partial}{\partial x} \left( \epsilon_0 \epsilon_r \frac{\partial \phi}{\partial x} \right) = -F \sum_{i=1}^n z_i C_i, \quad (5.6)$$

$$\frac{\partial C_i}{\partial t} = D_i \frac{\partial C_i}{\partial x} + \frac{D_i F z_i C_i}{RT} \frac{\partial \phi}{\partial x} + \frac{D_i N_A C_i \sum_{i=1}^N a_i^3 \frac{\partial C_i}{\partial x}}{1 - N_A \sum_{i=1}^N a_i^3 C_i}, \quad (5.7)$$

where  $\epsilon_0$  and  $\epsilon_r$  are the vacuum and the solvent dielectric permittivity,  $\phi$  is the electrostatic potential,  $z_i$  and  $C_i$  are the charge and the concentration distribution of  $i$ -th specie of the system,  $D_i$  is the specie's diffusion coefficient,  $a_i$  is the radius of the solid sphere with the molar volume equivalent to the cavity from the solvation model. We computed the diffusion constants using the Einstein-Stokes equation (Equation 3.5). For the continuum model, surface charging is dependent on the dielectric permittivity of the EDL.<sup>330</sup> Therefore, concentration dependent dielectric permittivity (Figure 28) can be calculated according to Equation 2.19.

Experimentally,<sup>311</sup> it was shown that the dielectric permittivity of a solution is dependent on the supporting electrolyte concentration (n-NBu<sub>4</sub>PF<sub>6</sub>) (Figure 29).

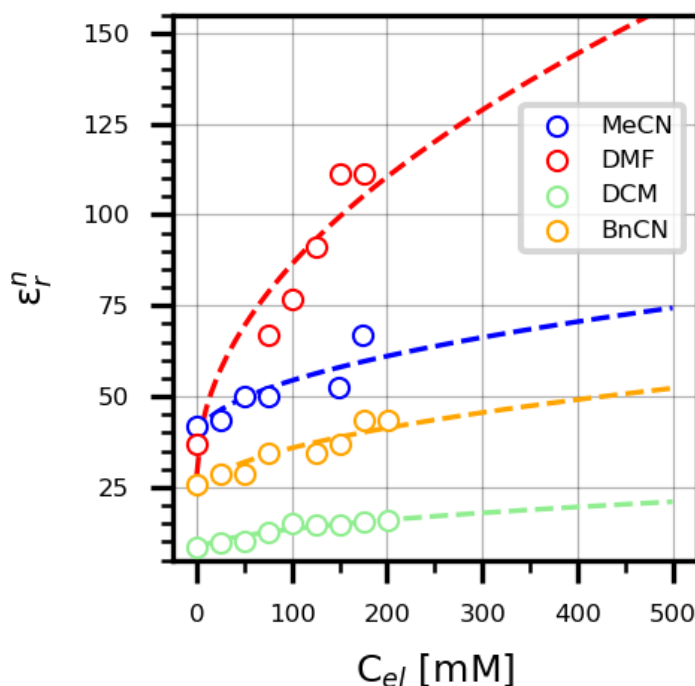


**Figure 29.** Dependence of dielectric permittivity of various solvents on electrolyte concentration (NBu<sub>4</sub>PF<sub>6</sub>). The experimental dielectric permittivity values are adapted from ref <sup>311</sup>. Available under a CC-BY 4.0 license. Copyright 2024 O. O'Mari, V. I. Vullev.

The curve fit for dielectric permittivity dependences on the supporting electrolyte concentration are summarized in the Table 7.

**Table 7.** Dielectric permittivity curve fit for four aprotic solvents often used in electrochemical measurements.

| Solvent | Equation  |
|---------|---|
| MeCN    | $\epsilon_r^n = 1.62 \cdot \sqrt{C_{el}} + 38.20$ |
| DMF     | $\epsilon_r^n = 5.79 \cdot \sqrt{C_{el}} + 28.45$ |
| DCM     | $\epsilon_r^n = 0.61 \cdot \sqrt{C_{el}} + 7.37$  |
| BnCN    | $\epsilon_r^n = 1.33 \cdot \sqrt{C_{el}} + 22.51$ |

Having derived the expression for the relative dielectric permittivity as a function of supporting electrolyte, one can now simulate the formation of EDL on the electrode surface and compute the potential-dependent rate constant for the forward and backward processes as described in Section 2.4.<sup>331,332</sup>

## 5.2 Electrode surface charge and Potential of Zero Charge

In this section, we will discuss electron transfer thermodynamics closely, considering aspects that influence the electrochemical potential of electrons in the electrode material. Assuming that the density of states in the electrode is high ( $\approx 10^{28}$  electrons/m<sup>3</sup>)<sup>333</sup> and the change in  $\mu_e$  due to the electron transfer is negligible. We are able to consider  $\mu_e$  as a constant value. Therefore, the electrochemical potential is affected solely by the electrostatic potential in the electrode ( $\phi_M$ ). Thus, adjusting  $\tilde{\mu}_e$ ,  $\phi_M$ , and  $\phi_{\text{Surf}}$  are changing accordingly (Figure 28).<sup>116,117,334</sup> In this study, we investigate the electron transfer process on the inert glassy carbon (GC) electrode and some of the most common electrode materials.  $\mu_e$  of electrons in the electrode can be calculated using the Thomas-Fermi approximation for homogeneous electronic gas as

$$\mu_e = \frac{h}{4\pi m} (3\pi^2 n_0)^{\frac{2}{3}}, \quad (5.8)$$

with  $h$  being the Planck constant,  $m$  is the mass of electron and  $n_0$  is the electrons number density. Since glassy carbon is a amorphous semiconductor, the electrons number density can be calculated knowing its band gap (BG). For GC the band gap is ranging from 1 to 0.05 eV.<sup>335</sup> Eventually, the electrons number density can be calculated via Equation 5.9.

$$n_0 = \frac{\rho N_A n}{M} e^{(-fBG)}, \quad (5.9)$$

where  $\rho$  is the GC density (1.5 g/cm<sup>3</sup>)<sup>336</sup>,  $N_A$  is the Avogadro number,  $n$  is the valence of carbon atom,  $M$  molar mass of carbon,  $f$  equals to  $F/RT$  with  $F$  being Faraday constant,  $R$  is gas constant, and  $T$  is the process temperature. Computed by this approach,  $\mu_e$  for GC equals to 4.49 eV which is close to experimental values in the range 4.5-4.6 eV.<sup>335,337,338</sup>

For the case of GC,  $\phi_M$  can be calculated from Equation 5.5 knowing the electrochemical potential. Experimentally, applied potential is always measured relative to a known reference system (standard hydrogen electrode, saturated calomel electrode, etc.). The electrochemical potential can be determined from the electrode's potential of zero charge (PZC), which represents the applied potential at which the surface charge density and  $\phi_{\text{Surf}}$  are zero. Thus, the electrochemical potential at the PZC is calculated as

$$\tilde{\mu}_e(\text{PZC}) = -(\text{PZC} + E_{\text{ref}})e_0, \quad (5.10)$$

where  $E_{\text{ref}}$  is the absolute electrode potential of the reference system. For our case, the experimentally obtained PZC for the GC electrode is 0.29 V vs. Standard Hydrogen Electrode

(SHE)<sup>339</sup>, and  $E_{\text{ref}}$  for SHE equals to 4.44 V.<sup>204</sup> Eventually,  $\phi_M$  computed from Equation 5.5 at the PZC is around 9.22 V.

For the rest of the metals that were studied, we establish a realistic model of an electrode surface relying on recent works of Tran et. al.<sup>340–342</sup> who shows the surface fraction distribution of various facets for a wide number of materials. In this study, we also focus on four transition metals frequently used in electrochemical setups (Ag, Cu, Au, Pt). The metal surfaces were represented as symmetric slabs with a thickness of four atomic layers within periodic boxes (computational details in Section 2.5).

The potential of zero charge (PZC) is a crucial parameter in understanding the interfacial properties of electrochemical systems. It represents the electrode potential at which the surface of an electrode has no net charge, meaning the positive and negative charges on the electrode surface are balanced. Table 8 summarizes electrochemical potentials of electrons in the electrode ( $\tilde{\mu}_e$ ), PZC of the surface facets with the highest coverage, and computed Fermi level for each structure.

Figure 30 shows computed the electrostatic potential profile for the Ag (111) surface at the potential of zero charge.

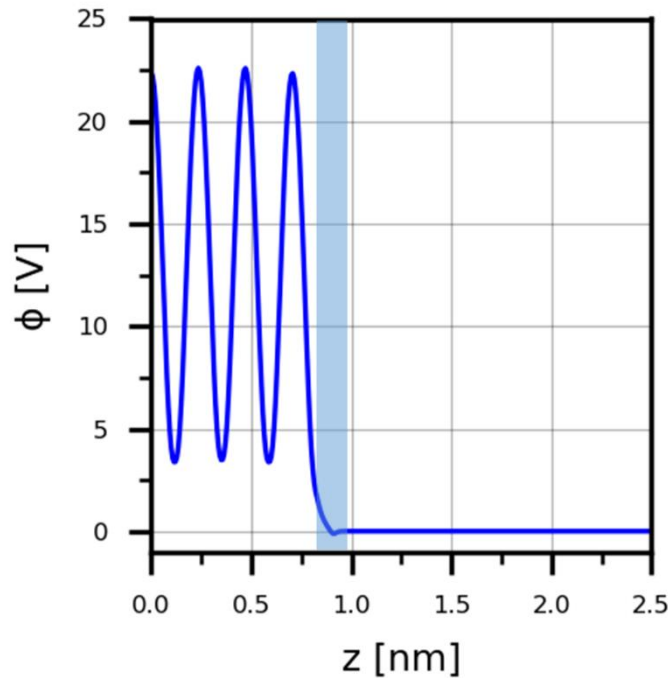


**Figure 30.** DFT computed electrostatic potential distribution of Ag(111) surface along the simulation cell. The blue region denotes the transition region between the silver atoms and the solution phase.

In the Figure 30, distinct peaks in electrostatic potential are visible at the surface atom cores when the cell size is below 0.8 nm, followed by a transition zone between the electrode's surface and the solution (cell size between 0.8 nm and 1 nm). Beyond this point, the electrostatic potential stabilizes, reaching a plateau that matches the potential in the bulk solution. Consequently, the applied potential at the potential of zero charge can be calculated using Equation 5.11.

$$\tilde{\mu}_e = E_f - e_0 \phi_{\text{bulk}}, \quad (5.11)$$

where  $\phi_{\text{bulk}}$  is the electrostatic potential in vacuum/bulk solution (e.g. electrostatic potential at 2.5 nm in Figure 30) and  $E_f$  is the corresponding Fermi level energy.

Furthermore, the applied potential can be calculated via Equation 3.1. The PZC of polycrystalline electrode surfaces were calculated using Equation 5.13.

$$\text{PZC}_{\text{surf}} = \sum_{i=1}^n \theta \text{PZC}_i, \quad (5.13)$$

where  $\theta$  is the surface fraction of a facet and  $\text{PZC}_i$  is the potential of zero charge of various facets.

**Table 8.** DFT computed properties of studied metallic electrode materials: Fermi levels ( $E_f$ ) of different facets, surface fractions of corresponding facets were extracted from recent publication<sup>341</sup>, electrochemical potential ( $-\tilde{\mu}_e$ ) at the PZC was computed according to Equation 5.11.

| Electrode | Facet | Surface fraction <sup>a</sup> | $E_f$ [eV] <sup>b</sup> | $-\tilde{\mu}_e$ [eV] <sup>c</sup> | PZC [V vs. $\text{Fc}^0/\text{Fc}^+$ ] | $\text{PZC}_{\text{surf}}$ [V vs. $\text{Fc}^0/\text{Fc}^+$ ] |
|-----------|-------|-------------------------------|-------------------------|------------------------------------|--|---|
| Ag        | 111   | 0.08                          | -4.98                   | 4.27                               | -0.59                                  | -0.70   |
|           | 322   | 0.63                          | -4.82                   | 4.18                               | -0.68                                  |   |
|           | 332   | 0.10                          | -4.80                   | 4.14                               | -0.72                                  |   |
|           | 100   | 0.18                          | -4.62                   | 4.00                               | -0.86                                  |   |
| Cu        | 111   | 0.46                          | -5.36                   | 4.59                               | -0.27                                  | -0.40   |
|           | 100   | 0.21                          | -4.98                   | 4.31                               | -0.55                                  |   |
|           | 311   | 0.10                          | -5.02                   | 4.31                               | -0.55                                  |   |
|           | 331   | 0.06                          | -5.06                   | 4.29                               | -0.57                                  |   |
|           | 221   | 0.06                          | -5.11                   | 4.38                               | -0.48                                  |   |
|           | 332   | 0.05                          | -5.11                   | 4.39                               | -0.47                                  |   |
|           | 322   | 0.05                          | -5.08                   | 4.43                               | -0.43                                  |   |
|           |       |                               |                         |                                    |  |   |

**Table 7.** DFT computed properties of studied metallic electrode materials: Fermi levels ( $E_f$ ) of different facets, Surface fractions of corresponding facets were extracted from recent publication<sup>341</sup>, electrochemical potential ( $-\tilde{\mu}_e$ ) at the PZC was computed according to Equation 5.11. (cont.)

|    |     |      |       |      |      |      |
|----|-----|------|-------|------|------|------|
| Au | 111 | 0.24 | -6.05 | 5.04 | 0.18 | 0.12 |
|    | 322 | 0.47 | -5.90 | 4.99 | 0.13 |      |
|    | 332 | 0.21 | -5.84 | 4.90 | 0.04 |      |
|    | 100 | 0.09 | -5.78 | 4.91 | 0.05 |      |
| Pt | 111 | 0.28 | -6.54 | 5.55 | 0.69 | 0.56 |
|    | 332 | 0.12 | -6.24 | 5.33 | 0.47 |      |
|    | 322 | 0.26 | -6.31 | 5.42 | 0.56 |      |
|    | 221 | 0.19 | -6.22 | 5.36 | 0.50 |      |
|    | 311 | 0.09 | -6.63 | 5.33 | 0.47 |      |
|    | 100 | 0.05 | -6.31 | 5.45 | 0.59 |      |

a - surface fractions obtained from ref.<sup>341</sup>

b - DFT computed Fermi level energies of studied facets

c - electrochemical potentials computed via Equation 5.13

Figure 31 depicts the parity plot illustrating the accuracy of our methodology by comparing the calculated potentials of zero charge (PZC) with the experimentally obtained values.<sup>200,343–347</sup>

Our findings show that our approach can effectively predict a potential of zero charge for studied transition metals with the overall mean average error 0.13 V which is within the error of the DFT approach. However, we can see that the PZC of Pt has the largest deviation among the studied metals. Moreover, experimental results also vary in range -0.75 to 0.1 V. This can be connected with the strong interaction of the solvent molecules with the electrode surface.<sup>287,343,348–350</sup> Ludwig et. al. has shown in his recent work that at the potential of zero charge acetonitrile is chemisorbed at the platinum surface.<sup>345</sup>

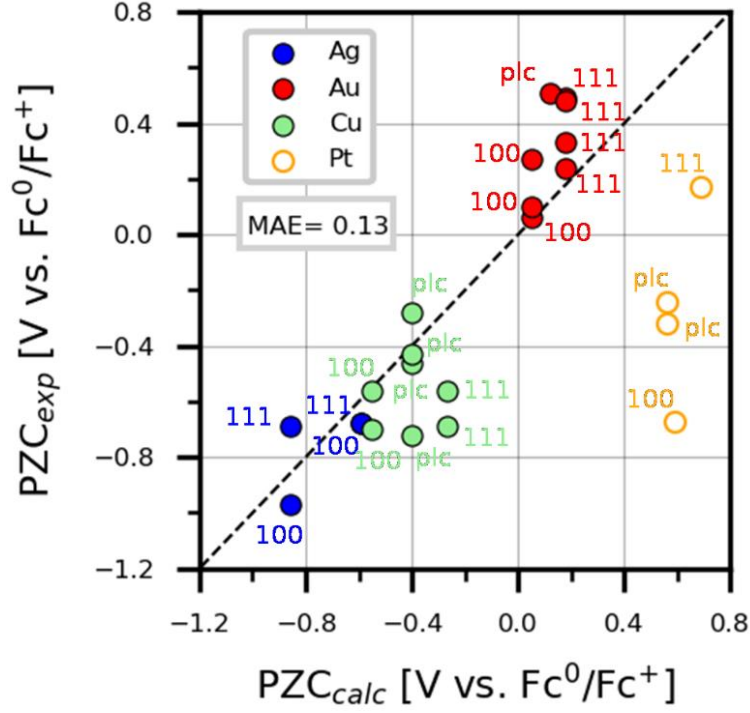


**Figure 31.** Parity plot of DFT computed and experimental potentials of zero charge (PZC) for various surface facets and polycrystalline (plc) electrode surface. Indexes in the Figure denote the Miller's index of the facet and inherit the color scheme from the figure's legend.

To assess the accuracy of the polycrystalline electrode model we investigated the surface charging of electrodes in the MeCN solution with 100 mM of n-NBu<sub>4</sub>PF<sub>6</sub> according to the methodology described in Section 2.5. Changing the number of electrons in the system, we are able to compute the surface charge dependence on the applied potential. The surface charge of polycrystalline surface can be calculated according to Equation 5.14:

$$\sigma_M = \sum_{i=1}^n \theta_i \sigma_M(E)_i, \quad (5.14)$$

where  $\sigma_M(E)_i$  is the surface charge of i-th facet.

Figure 32 represents the dependence of the surface charge density on the applied potential of the electrode.



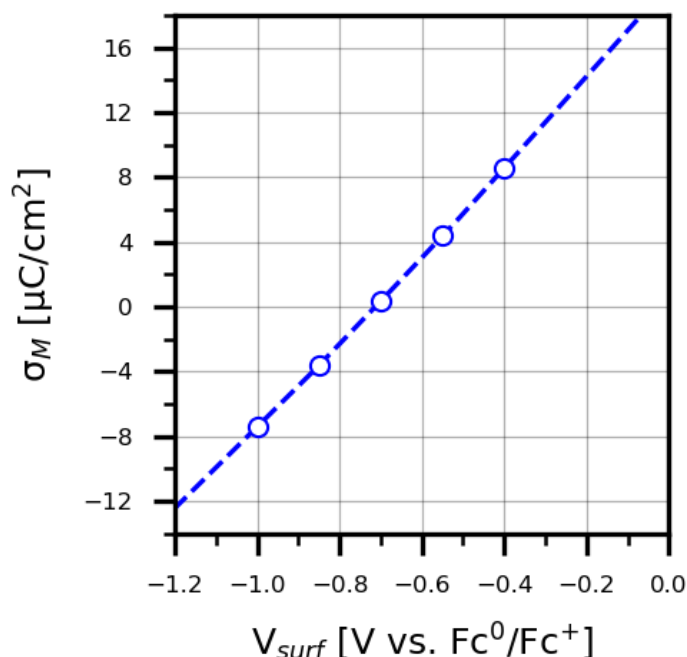


**Figure 32.** Surface charge density of the polycrystalline silver electrode as a function of applied potential computed with the implicit electrolyte module, VASPsol. The slope of the curve determines the capacitance of the electric double layer.

The linear slope of  $\sigma_M(E)$  is the EDL capacitance, fitting the linear polynomial to the computed results. Evaluating the slope at the PZC ( $\sigma_M = 0 \mu C/cm^2$ ) we can obtain the double layer capacitance. Table 9 compares experimental and computed electric double layer capacitances at the PZC for the studied electrode materials.

**Table 9.** Comparison of experimental and computed data obtained from the linear slope of the surface charge (EDL capacitance) using VASPsol implicit electrolyte module.

| Electrode material | $C_{dl \text{ exp}}$ [ $\mu F/cm^2$ ] | $C_{dl \text{ calc}}$ [ $\mu F/cm^2$ ] |
|--------------------|---------------------------------------|--|
| Ag                 | 28.5 <sup>351</sup>                   | 26.55                                  |
| Cu                 | 25.0 <sup>352</sup>                   | 25.82                                  |
| Au                 | 25.0 <sup>344</sup>                   | 23.35                                  |
| Pt                 | 30 <sup>349</sup>                     | 22.75                                  |

Our computational results show a strong alignment with experimental data, confirming the reliability of our approach for modelling polycrystalline electrode surfaces. This alignment suggests that our model accurately captures the key characteristics of polycrystalline surfaces, providing a solid foundation for further simulations and predictions in various electrochemical applications.

### 5.3 Supporting Electrolyte Influence on the Thermodynamics of $\text{Fc}^0/\text{Fc}^+$ Oxidation on the Glassy Carbon Electrode

A critical, yet often underexplored, factor affecting electron transfer dynamics and thermodynamics is the role of supporting electrolytes. These inert ionic species, which are added to stabilize the electrochemical environment, exert substantial influence on electron transfer processes. Through modulation of ionic strength, double-layer structure, and solvation properties, supporting electrolytes shape the energetic landscape in which electron transfer occurs. Consequently, understanding how supporting electrolyte concentration, composition, and ionic properties influence electron transfer thermodynamics is essential for optimizing electrochemical processes across applications.

The solvation environment of the electroactive specie can have huge effect on the electron transfer, participating in the hydrogen bonds formation and other short-range interactions.<sup>91,285</sup> Figure 33 shows schematic dependence of the chemical potential of  $\text{Fc}^0/\text{Fc}^+$  system in the EDL with various concentration of supporting electrolyte ( $n\text{-NBu}_4\text{PF}_6$ ).

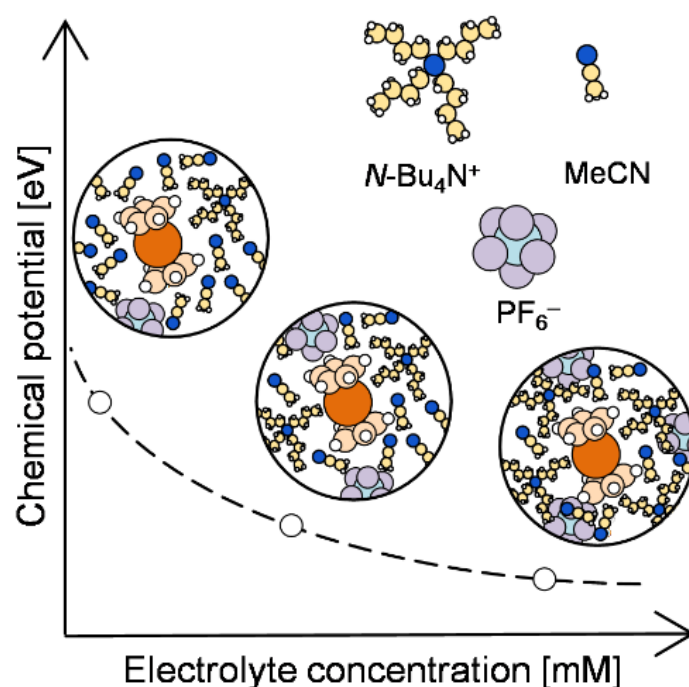


**Figure 33.** Schematic representation of supporting electrolyte influence on the chemical potential of reagents and products. Solvent environment is approximated as bulk solution with different supporting electrolyte concentration modeled with COSMO-RS solvation model.

To assess the influence of supporting electrolyte on the  $\text{Fc}^0/\text{Fc}^+$  oxidation process, we calculated the free energy correction via the equation:

$$\Delta G_r^0 = \Delta G_r^{\text{gas}} + \Delta G_{\text{solv}}, \quad (5.15)$$

where  $\Delta G_r^0$  is the reaction free energy change,  $\Delta G_r^{\text{gas}}$  is the free energy change and  $\Delta G_{\text{solv}}$  is the solvation energy change.

$\Delta G_{\text{solv}}$  can be calculated from

$$\Delta G_{\text{solv}} = \Delta G_{\text{solv}}^{\text{PCM pure}} - \Delta G_{\text{solv}}^{\text{COSMO pure}} + \Delta G_{\text{solv}}^{\text{COSMO } i}, \quad (5.16)$$

where  $\Delta G_{\text{solv}}^{\text{PCM pure}}$  is the solvation energy change in a pure solvent obtained by the PCM solvation model,  $\Delta G_{\text{solv}}^{\text{COSMO pure}}$  is the solvation energy change in a pure solvent obtained by the COSMO-RS solvation model and  $\Delta G_{\text{solv}}^{\text{COSMO } i}$  is the solvation energy change in a mixture with  $i$  mM of tetrabutylammonium hexafluorophosphate (NBu<sub>4</sub>PF<sub>6</sub>). We studied the influence of various aprotic solvents widely used for electrochemical measurements: dichloromethane (DCM), acetonitrile (MeCN), N,N-dimethylformamide (DMF) and benzonitrile (BnCN).

Figure 34 shows the dependence of the Fc<sup>0</sup>/Fc<sup>+</sup> free energy change on the supporting electrolyte concentration.

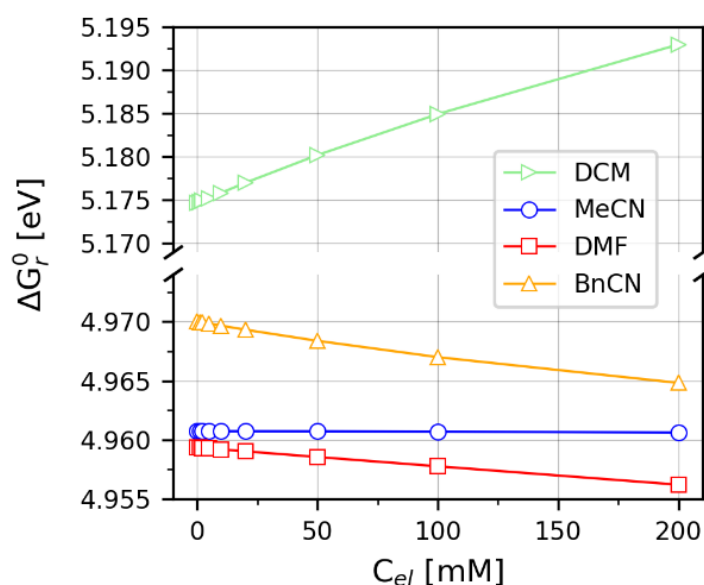


**Figure 34.** DFT computed (via Equations 5.15 and 5.16) free Gibbs energy dependence on n-NBu<sub>4</sub>PF<sub>6</sub> concentration.

Our findings show that the ferrocene oxidation process is slightly dependent on the concentration of the supporting electrolyte within the studied range. This aligns with the experimentally measured oxidation potentials of ferrocene, which exhibit relatively little dependence on the polarity of the pure solvents used for the measurements.<sup>164,353,354</sup> Furthermore, the oxidation potential of ferrocene shows negligible dependence on the chemical composition of the electrolyte and the material of the working electrode used for voltametric

measurements.<sup>355,356</sup> However, changes in the concentration of the supporting electrolyte cause dramatic shifts in the half-wave potentials of ferrocene oxidation in dilute solutions and will be discussed later (Section 5.3).<sup>164,300,357,358</sup>

#### 5.4 Supporting Electrolyte Influence on the Electron Transfer Kinetics of $\text{Fc}^0/\text{Fc}^+$ Oxidation Process on the Glassy Carbon Electrode

In this section, we discuss kinetic aspects of  $\text{Fc}^0/\text{Fc}^+$  electron transfer. Firstly, we computed the viscosities of some solvents, commonly used in electrochemical measurements, using the quantity-structure relation model (QSPR) implemented in COSMOtherm. Further, we computed the molecular volume, and the diffusion coefficients of  $\text{Fc}^0$  and  $\text{Fc}^+$  and summarized all the data in Table 10.

**Table 10.** Experimental and computed mobility parameters of ferrocene in various solvents.<sup>164</sup>

| Solvent | Viscosity [Pa·s] <sup>a</sup> | $D_{\text{Fc}}$ calc [cm <sup>2</sup> /s] <sup>b</sup> | $D_{\text{Fc}}$ exp [cm <sup>2</sup> /s] |
|---------|-------------------------------|--|--|
| MeCN    | $0.41 \times 10^{-3}$         | $1.38 \times 10^{-5}$                                  | $2.24 \times 10^{-5}$                    |
| DMF     | $0.68 \times 10^{-3}$         | $0.84 \times 10^{-5}$                                  | $0.95 \times 10^{-5}$                    |
| DCM     | $0.35 \times 10^{-3}$         | $1.64 \times 10^{-5}$                                  | $1.67 \times 10^{-5}$                    |
| BnCN    | $1.31 \times 10^{-3}$         | $0.43 \times 10^{-5}$                                  | -  |

a – viscosities obtained using QSPR model implemented in COSMOtherm.

b – diffusion constants computed using Einstein-Stokes equation (Equation 3.5)

Previously, in Section 5.3, we showed that supporting electrolyte concentration has negligible influence to the electrochemical reaction free energy. Therefore, in this section we use PCM computed solvation energy for the reagent and the product without taking into account concentration correction. We summarized main thermodynamic and kinetic parameters for the  $\text{Fc}^0/\text{Fc}^+$  system in the Table 11.

**Table 11.** Reaction free energy change, total reorganization energy and standard rate constant of the electron transfer. Free energy change was computed according to Equation 3.2, total reorganization energy and standard rate constant were computed via Equation 2.35.

| Solvent | $\Delta G_r$ [eV] | $\lambda_{\text{tot}}$ [eV] | $k^0$ [cm/s] |
|---------|-------------------|-----------------------------|--------------|
| MeCN    | 4.96              | 0.48                        | 44.05        |
| DMF     | 4.96              | 0.62                        | 10.80        |
| DCM     | 5.18              | 0.46                        | 51.60        |
| BnCN    | 4.97              | 0.62                        | 11.60        |

Initially, we performed a simulation for the  $\text{Fc}^0/\text{Fc}^+$  oxidation process in the MeCN solution containing 50 mM of n-NBu<sub>4</sub>PF<sub>6</sub>. The initial concentration of  $\text{Fc}^0$  was set to 5 mM (Figure 35). The scan rate for all simulations in this section was set to 0.05 V/s.

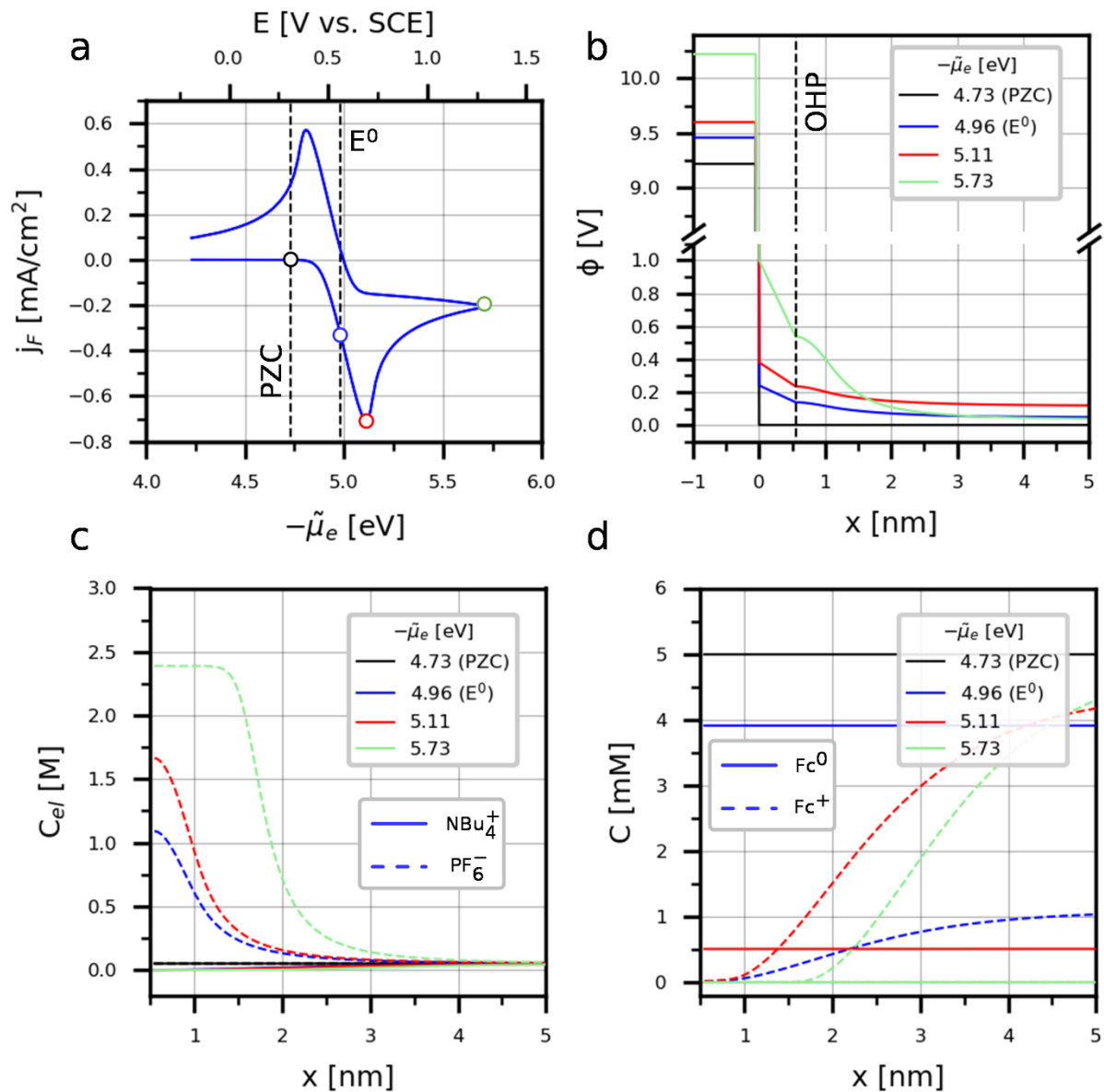


**Figure 35.** Electrochemical response of  $\text{Fc}^0/\text{Fc}^+$  oxidation process in MeCN solution with 50 mM of n-NBu<sub>4</sub>PF<sub>6</sub> with 5 mM of  $\text{Fc}^0$  and scan rate of 50 mV/s (a). The black dashed lines denote the electrochemical potential of electrons in the electrode at the potential of zero charge, and standard equilibrium potential for the  $\text{Fc}^0/\text{Fc}^+$  system. Colored points represent four critical points which are shown in the rest of subplots. Electrostatic potential (b) along the 5 nm from the electrode surface represents the EDL structure. The black dashed line denotes

the outer-Helmholtz plane. Supporting electrolyte (c), reagent and product (d) concentration distribution within the 5 nm from electrode surface.

Our findings show CV response (Figure 35a) as the function of the electrochemical potential. Moreover, to be able to compare our results with the experiment we also represented the dependence on the applied potential relative to SCE. The potential of the reference electrode was set to 4.42 V as recommended in previous studies.<sup>91</sup> To assess the performance of our model, we computed the half-wave potential of the simulated results. Half-wave potential can be computed from CV response via the equation:

$$E_{1/2} = \frac{E_p^C + E_p^A}{2}, \quad (5.15)$$

where  $E_p^C$  and  $E_p^A$  are the cathodic and anodic peak potentials, respectively.

Comparing this parameter obtained in our simulation (0.54 V vs. SCE) with the experimental (0.47 V vs. SCE)<sup>300</sup> half-wave potential we show that our approach can be an accurate tool for the electron transfer kinetics prediction. Figure 35b shows the distribution of the electrostatic potential within the 5 nm from the electrode surface and in the bulk glassy carbon electrode. It was demonstrated how the change in electrostatic potential in the electrode material affects the electrostatic potential distribution within the whole simulation region. Figures 35c,d are representing the solution components distribution within the first 5 nm from the electrode surface. The electrostatic potential increase in the electrode material causes the adsorption of anions on the electrode surface (Figure 35c) and reach a steric limit for a particular type of anions ( $\text{PF}_6^-$ ) of around 2.5 M.<sup>118</sup> Figure 35d shows us that the concentration of  $\text{Fc}^+$  in the electrode region decreases due to the electrostatic interaction with the positively charged electrode surface, whereas the concentration of neutral  $\text{Fc}^0$  stays unchanged in the region of 5 nm from the electrode surface.

Furthermore, we investigated the supporting electrolyte influence on the electrode kinetics. Figure 36 represents the activation energy (computed via the Equation 5.16) of the  $\text{Fc}^0/\text{Fc}^+$  electron transfer dependence on the electrochemical potential and electrostatic potential at the OHP.

$$\Delta G^\ddagger = \frac{\lambda}{4} \left( 1 + \frac{\eta}{\lambda} \right)^2, \quad (5.16)$$

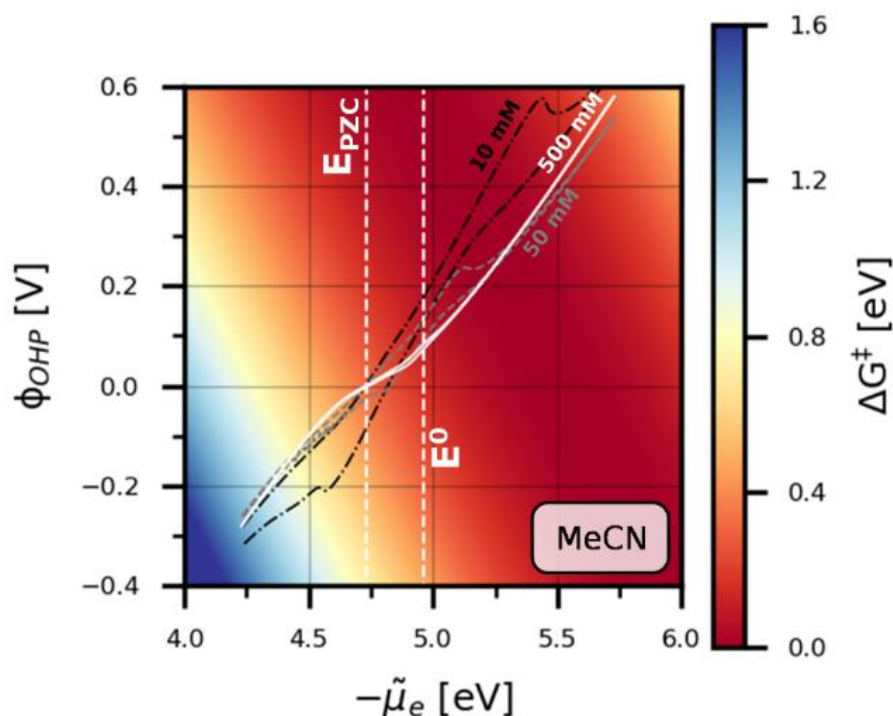


**Figure 36.** Computed (Equation 5.16) activation energy for  $\text{Fc}^0/\text{Fc}^+$  oxidation process in MeCN solution as a function of applied potential ( $E$ ) and OHP electrostatic potential ( $\phi_{\text{OHP}}$ ). Color lines denote  $\phi_{\text{OHP}}$  potential dependence on the applied potential from COMSOL simulations with different concentration of  $n\text{-NBu}_4\text{PF}_6$  and 5 mM of  $\text{Fc}^0$  and potential scan rate of 50 mV/s. White lines represent the position of the reaction equilibrium potential ( $E^0$ ) and electrode applied potential at the point of zero charge ( $E_{\text{PZC}}$ )

These results show that the concentration of supporting electrolyte dramatically affects the activation energy of the process. Supporting electrolyte influences the EDL structure modulating  $\phi_{\text{OHP}}$  and changing the activation energy of the process accordingly. This influences the kinetics of the process by decreasing the electron transfer rate. These findings are summarized in Figure 37. The dependence of the equilibrium constant on the applied potential shows that decreasing the concentration of  $n\text{-NBu}_4\text{PF}_6$  in the system we can modulate forward and backward rates of the electron transfer. These results also describe the electrochemical reaction asymmetry without additionally fitted parameters.<sup>110,129,140,142</sup> Additionally, we can see that solution design can intensify the electron transfer rate for a particular reaction even at lower supporting electrolyte concentration as was shown in Figure 37 in the applied potential range from 5.25 to 5.75 eV, for the cases of 50 and 500 mM.

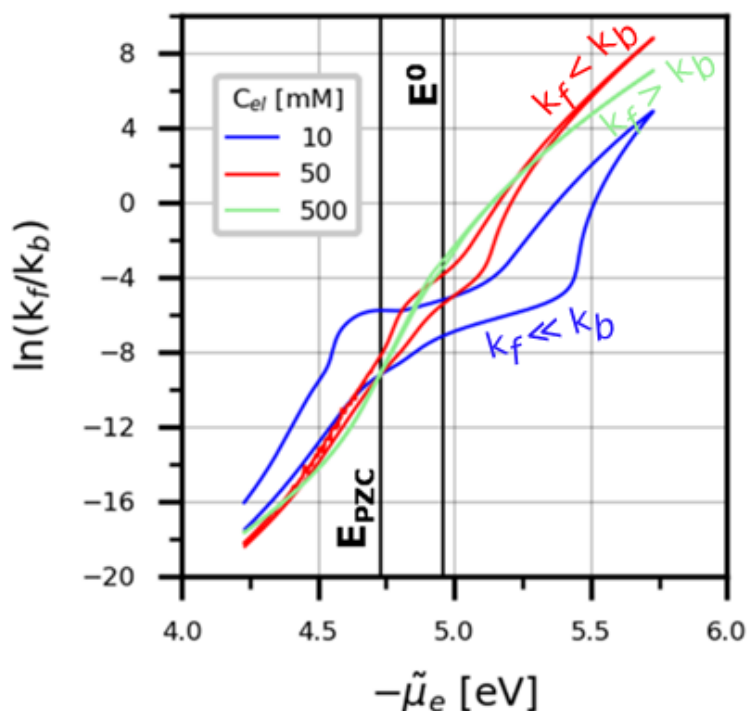


**Figure 37.** Equilibrium constant dependence on the applied potential for three studied supporting electrolyte concentrations with 5 mM of  $\text{Fc}^0$  and 50 mV/s of scan rate. The black lines represent the applied potential at the potential of zero charge ( $E_{\text{PZC}}$ ), and equilibrium potential ( $E^0$ ) for  $\text{Fc}^0/\text{Fc}^+$  electron transfer.

Another important parameter when discussing electron transfer in different solvents is reorganization energy.<sup>359–361</sup> Table 10 collects thermodynamic and kinetic parameters of  $\text{Fc}^0$  oxidation for wide ranges of solvents usually used in electrochemical setups. Reorganization energy refers to the energy required to reorganize both the reactants and the solvent environment during the electron transfer process. Solvents with lower reorganization energies typically facilitate faster electron transfer kinetics. Among the solvents studied, DCM exhibits the highest reorganization energy, leading to the standard rate constant of 51.6 cm/s and despite its low dielectric permittivity (7.37), which implies less charge stabilization, the complex influence of solvent properties (reorganization energy, viscosity) makes DCM the most kinetically favorable solvent in the studied list. However, its solvation effect shifts the Gibbs free energy from around 4.96 eV for MeCN, DMF and BnCN to 5.17 eV.

Summarizing the results of our kinetic model we are able to reproduce an electrochemical response of  $\text{Fc}^0$  oxidation vs. absolute potential. Figure 38 represents CV curves of  $\text{Fc}^0/\text{Fc}^+$  with 50 mM of  $n\text{-NBu}_4\text{PF}_6$ . It shows that solvation effect has huge impact on



electron transfer, influencing the peak positions and the shape of CV response. Analyzing our results, it is possible to compute the difference between the  $\Delta G_r^0$  and the absolute peak potential ( $-\tilde{\mu}_e$ ) showing the qualitative effect of solvent to the electron transfer kinetics.

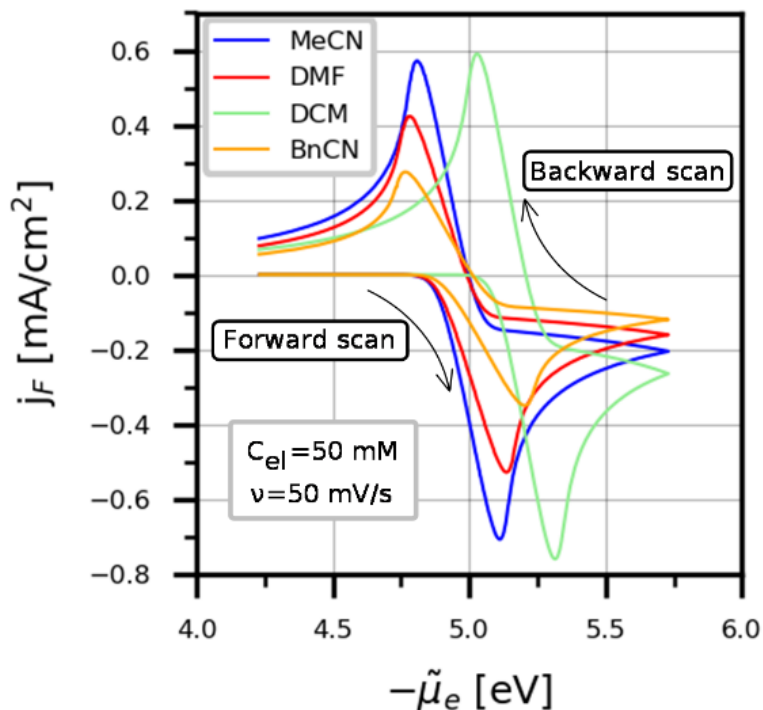


**Figure 38.** Solvent influence on the electrochemical response of  $\text{Fc}^0/\text{Fc}^+$  electron transfer with 50 mM of  $n\text{-NBu}_4\text{PF}_6$  and 50 mV/s.

Our results demonstrate that this descriptor can be used to guide the selection of a solvent for a specific reaction. In our study, we observed that the electron transfer kinetics follows the trend  $\text{DCM} > \text{MeCN} > \text{DMF} > \text{BnCN}$ , which mirrors previous experimental findings.<sup>178,362–364</sup> The peak potential intensity is related to the ions, solvent and reactant mobility in the EDL and presents a similar trend as the solvent viscosity (Table 9).<sup>365–367</sup>

Figure 39 provides an important insight into the influence of the solvent environment and the concentration on the electrochemical behavior of the ferrocene couple in three different solvents. By comparing experimental results<sup>300</sup> with our simulated data at varying concentrations of the supporting electrolyte, the figure sheds light on the strengths and limitations of the electrochemical model, particularly in different solvent systems.

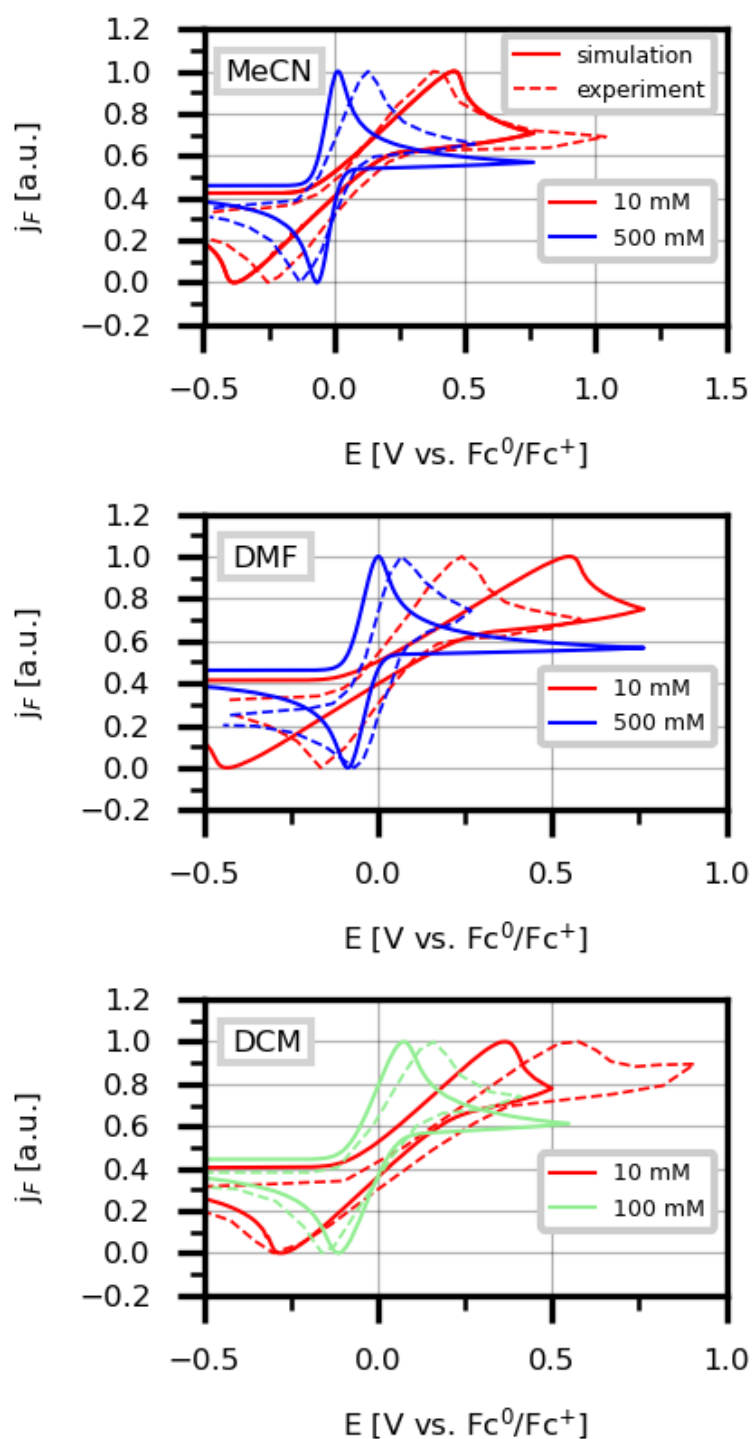


**Figure 39.** Experimental and simulated CV curves of ferrocene oxidation with 0.05 V/s scan rate for different concentrations of supporting electrolyte. Solid line represents simulated CV, dashed line represents experimental CVs

MeCN is a commonly used solvent in electrochemical studies due to its high dielectric constant and good solubility for ionic species. The electrochemical response of  $Fc^0/Fc^+$  in acetonitrile shows relatively symmetric peaks for 10 and 500 mM of  $n\text{-NBu}_4\text{PF}_6$ , reflecting a clean, quasi-reversible electron transfer process. Our results suggest that the model captures

the behavior of this system well. The deviation at a high concentration could be attributed to the concentration polarization effect. Simulation results at a lower supporting electrolyte concentration show a relatively high deviation, possibly due to specific interactions between DMF and the electroactive species. This discrepancy highlights the importance of considering solvent-specific effects beyond simple diffusion, such as changes in the solvation shell or ion pairing, which might play a more significant role in DMF. The broad, less defined peaks in both the experimental and simulated curves suggest that electron transfer kinetics may be slower in DCM, or that mass transport limitations are more significant in this solvent.

### 5.5 Supporting Electrolyte Influence to the Electron Transfer in the Reference Reactions on the Glassy Carbon Electrode

Despite the importance of this topic, many aspects of the electrolyte's influence remain ambiguous, especially in complex systems where electrolyte ions interact with reactive species and the electrode surface. This research addresses these gaps, focusing on the thermodynamic aspects of electron transfer in the presence of various supporting electrolytes. By investigating these effects systematically, this study aims to provide insights that will enable the precise tuning of electrochemical reactions through electrolyte engineering. We investigated the influence of solvent and supporting electrolyte concentration on the electron transfer thermodynamics of reference molecules (Figure 40).

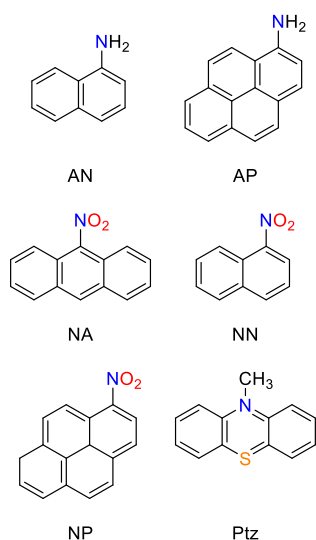


**Figure 40.** Structures of 1-naphthylamine (AN), 1-aminopyrene (AP), 9-nitroanthracene (AN), 1-nitrophenanthrene (NN), 1-nitropyrene (NP), and 10-methylphenothiazine (Ptz).

Now, we compare calculated and experimental equilibrium potentials of studied molecules to check the accuracy of our approach. Figure 41 shows the parity plot for computed and experimental equilibrium potentials in various solvents.

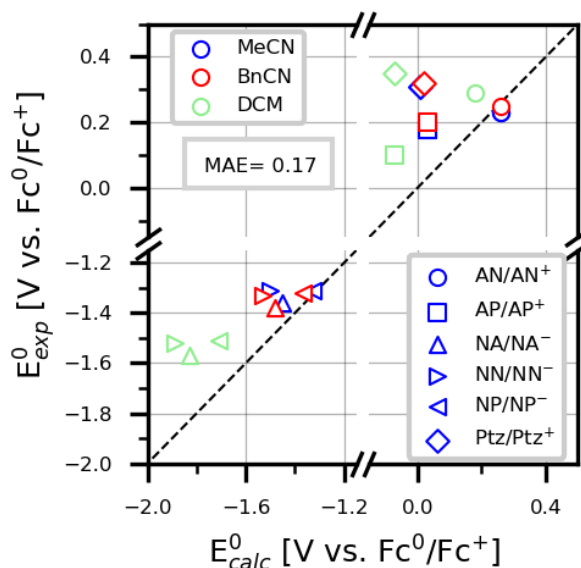


**Figure 41.** Comparison of experimental and computed standard equilibrium potentials ( $E^0$ ) of test reactions using the  $Fc^0/Fc^+$  reference with BP86 functional and def2-TZVP basis set.

Figure 41 confirms the accurate prediction of SEPs using CFE at the BP86 level of theory with the MAE of only 0.17 V. Note that this error is within the accuracy of typical DFT functionals ( $\pm 0.20$  eV). Having thermodynamic results of the test reactions, we will now use them to evaluate electron transfer kinetics in the framework of the Marcus-Hush model which was previously discussed in Section 2.4.

Now, we summarize theoretical thermodynamic and kinetic data for the reference reactions in various non-aqueous solvents (Table 12).

**Table 12.** The change in the reactions free energy, total reorganization energy and standard rate constant of the electron transfer in various aprotic solvents. Free energy change was computed according to Equation 3.2, total reorganization energy, and standard rate constants were computed via Equation 2.35.

| Reaction   | Solvent | $\Delta G_r$ [eV] | $E^0$ [V vs. $Fc^0/Fc^+$ ] | $\lambda_{tot}$ [eV] | $k^0$ [cm/s] |
|------------|---------|-------------------|----------------------------|----------------------|--------------|
| AN/ $AN^+$ | MeCN    | 5.22              | 0.26                       | 0.59                 | 17.42        |
| AP/ $AP^+$ | MeCN    | 4.99              | 0.03                       | 0.52                 | 29.76        |
| NA/ $NA^-$ | MeCN    | -3.51             | -1.45                      | 0.56                 | 18.57        |

**Table 12.** The change in the reactions free energy, total reorganization energy and standard rate constant of the electron transfer in various aprotic solvents. Free energy change was computed according to Equation 3.2, total reorganization energy, and standard rate constants were computed via Equation 2.35. (cont.)

|                      |      |       |       |      |        |
|----------------------|------|-------|-------|------|--------|
| NN/NN <sup>-</sup>   | MeCN | -3.46 | -1.50 | 0.78 | 2.52   |
| NP/NP <sup>-</sup>   | MeCN | -3.63 | -1.33 | 0.61 | 11.34  |
| Ptz/Ptz <sup>+</sup> | MeCN | 4.97  | 0.01  | 0.69 | 5.52   |
| AN/AN <sup>+</sup>   | DCM  | 5.36  | 0.18  | 0.45 | 69.89  |
| AP/AP <sup>+</sup>   | DCM  | 5.10  | -0.07 | 0.39 | 101.43 |
| NA/NA <sup>-</sup>   | DCM  | -3.34 | -1.83 | 0.55 | 22.25  |
| NN/NN <sup>-</sup>   | DCM  | -3.28 | -1.89 | 0.64 | 9.89   |
| NP/NP <sup>-</sup>   | DCM  | -3.46 | -1.71 | 0.45 | 54.98  |
| Ptz/Ptz <sup>+</sup> | DCM  | 5.10  | -0.07 | 0.56 | 20.55  |
| AN/AN <sup>+</sup>   | BnCN | 5.24  | 0.26  | 0.46 | 64.67  |
| AP/AP <sup>+</sup>   | BnCN | 5.00  | 0.03  | 0.39 | 95.60  |
| NA/NA <sup>-</sup>   | BnCN | -3.49 | -1.48 | 0.58 | 15.28  |
| NN/NN <sup>-</sup>   | BnCN | -3.44 | -1.53 | 0.65 | 9.10   |
| NP/NP <sup>-</sup>   | BnCN | -3.61 | -1.37 | 0.49 | 35.85  |
| Ptz/Ptz <sup>+</sup> | BnCN | 4.99  | 0.02  | 0.57 | 18.08  |

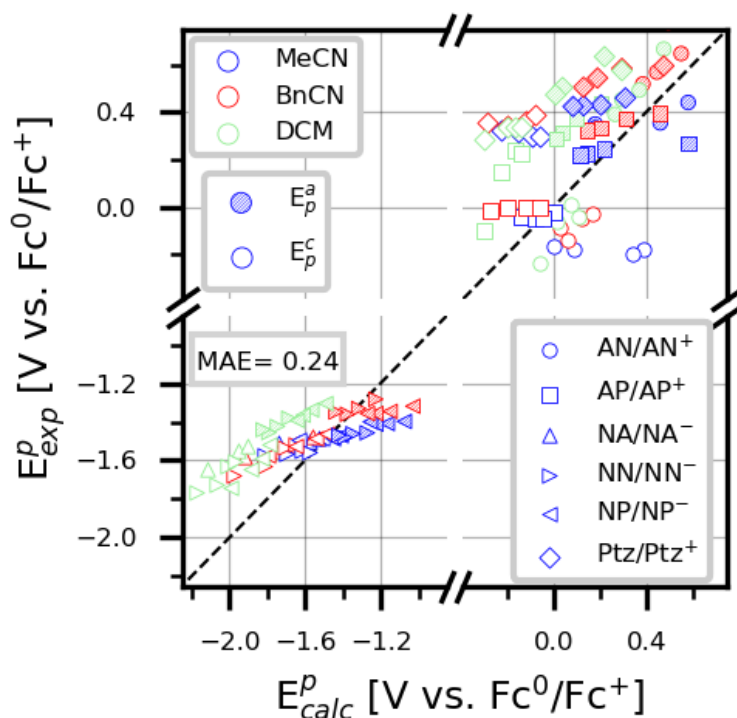


**Figure 28.** Representation of accuracy for peak potential prediction by Marcus-Hush model.  $E^p_a$  and  $E^p_c$  are anodic and cathodic peak potentials, respectively.

Figure 42 provides a visual representation of the correlation between the calculated and experimental peak potentials ( $E^p_{calc}$  and  $E^p_{exp}$ , respectively) for reference reactions in MeCN, BnCN and DCM. The general trend shows a positive correlation between experimental and our computed results. However, the scatter of points away from the diagonal line suggests that there are inherent limitations in the accuracy of the model.

## 5.6 Summary and Conclusion

In summary, this study investigates how solvents and supporting electrolytes influence the thermodynamics and kinetics of electron transfer, with a particular focus on the  $\text{Fc}^0/\text{Fc}^+$  redox couple. By examining solvent effects using solvation models, this research sheds light on how non-aqueous solvents and variations in supporting electrolyte concentrations impact electrochemical reactions, offering a more nuanced understanding of these complex systems. Additionally, the study delves into electrode reaction kinetics using the Marcus-Hush model, which enables the calculation of rate constants for the  $\text{Fc}^0/\text{Fc}^+$  system as well as other reference reactions, thereby providing detailed insights into the mechanisms governing electron transfer.

To deepen this understanding, cyclic voltammetry (CV) simulations were employed to investigate electrochemical behavior under varying conditions. The simulations enabled the observation of peak shifts and half-wave potentials, allowing for a closer examination of the effects of different solvents and electrolyte concentrations. This work also introduces the computational  $\text{Fc}^0/\text{Fc}^+$  electrode as a valuable reference point for computational studies, similar in utility to the computational hydrogen electrode widely used for modelling coupled proton-electron transfer reactions. The  $\text{Fc}^0/\text{Fc}^+$  reference demonstrates particular effectiveness for studying electron transfer processes in non-aqueous systems.

Our findings, validated by experimental data, illustrate the model's capability to predict key metrics, such as peak potentials and half-wave potentials. While some deviations were noted, especially in reduction potentials impacting peak positions, the model provides qualitative insights that enhance our understanding of the electrochemical processes. This research lays the groundwork for future studies focused on refining computational approaches to better capture subtle effects in electrochemical systems, advancing the design of predictive models and facilitating improved materials selection for various electrochemical applications.

## 6. Outlook

This research investigates the heterogeneous electron transfer between electrodes and electroactive species, aiming to clarify the complexity of this process. The thesis is structured around three main objectives. Firstly, we created a dependable reference model for the electron transfer using the  $\text{Fc}^0/\text{Fc}^+$  system that is versatile across solvents and systems. Our DFT-based Marcus-Hush kinetic model for the electron transfer allowed us to simulate CVs using the output from quantum-chemical calculations. This approach helped us avoid using any experimentally fitted parameters. Secondly, we applied our model to describe the process of electrocarboxylation of the benzyl chloride in all its details, including the multistep electron transfer and related chemical steps. Our results showed that the model can effectively catch the electrochemical behavior of the system by predicting the CV response, the concentration profiles of species and the rate determining steps of the process. Eventually, we extended our computational ferrocene electrode model to predict the influence of the supporting electrolyte and the EDL formation on the heterogeneous electron transfer. Our model captures the electrostatic potential drop at the electrode surface due to the ions adsorption and assesses its effect in the reaction kinetics and thermodynamics.

In Chapter 3, we focused on determining the absolute electrode potentials, reduction potentials, and the reaction kinetics, particularly for the ferrocene/ferrocenium reference system. An evaluation of various DFT functionals showed that UKS calculations generally underestimate ionization energies, especially in functionals with a significant Hartree-Fock exchange. The ROKS method corrects this by bringing calculated ionization energies closer to experimental values, especially when using PBE and M06 functionals. ROKS also enhances reduction potential predictions across functionals, with the M06 functional delivering the highest accuracy. The study also explores electrode reaction kinetics, computing activation energies through the Marcus-Hush model, which establishes M06 as a highly accurate functional for reduction potential and activation energy predictions.

Moreover, CV simulations were utilized to assess the electrochemical behavior of reference reactions and the  $\text{Fc}^+/\text{Fc}^0$  system. The model aligned well with experimental data in forecasting peak potentials and current density responses with minor discrepancies. This in-depth examination highlights the critical role of functional selection in achieving accurate predictions across various electrochemical scenarios, offering valuable insights for further electrochemical studies. While this model covers many aspects of real-world systems, future improvements could incorporate dynamic solvent effects and electrode-molecule interactions



for higher accuracy. Results were closely aligned with experimental data, confirming the method's validity and applicability to similar electrochemical transformations.

Chapter 4 presents a method for calculating energetics and kinetic barriers in electron transfer steps, applied to the electrochemical carboxylation of benzyl chloride (BnCl) in acetonitrile. Building on the CHE model, this approach uses the  $\text{Fc}^0/\text{Fc}^+$  redox couple as a standard for consistent comparisons. Marcus theory assessed electron transfer barriers from the electrode to the solvated molecule at the EDL.

Chapter 5 extends on the CHE model introduced in Chapter 3 to include the impact of the EDL formation and the supporting electrolyte of the electron transfer kinetics and thermodynamics. Using a combination of the COSMO-RS and the PCM solvation models, the research sheds light on the effect of non-aqueous solvents and different concentrations of  $n\text{-NBu}_4\text{PF}_6$  on electrochemical reactions. Our extended model accounts for the generalized modified Poisson-Nernst-Planck model which allows to simulate the migration of the charged species in solution and accounts for the steric properties of the chemical species. The modified Marcus-Hush model with the Frumkin's correction term was applied to compute the electron transfer rate constants, providing detailed insights into electron transfer mechanisms. Through CV simulations, we observed the effects of different solvents and electrolyte concentrations on peak shifts and half-wave potentials. The computational  $\text{Fc}^0/\text{Fc}^+$  electrode served as a valuable reference point, similar to the computational hydrogen electrode, and was validated against experimental data, offering qualitative insights to enhance the understanding of the electrochemical process.

The study proposes that the electrochemical potential at the zero charge could help to optimize electrode material selection. Future research should refine this model to include detailed electrode surface characteristics, like atomic structure and electronic properties, for a better understanding of reaction kinetics and selectivity. Expanding this framework to include proton coupled electron transfers could extend its applications in electrocatalysis and energy storage. This research establishes a foundation for advancing electrochemical transformations, providing tools and understanding that will support the development of next-generation materials and processes in sustainable chemistry and energy conversion.

## A Complete List of Publications

(1)

1. Alikina, M.; Shkodenko, L.; Kramarenko, A.; Chernyshov, I.; Belyaeva, A.; Gutsalova, A.; Krivoshapkina, E.; Koshel, E.; Vinogradov, A. ClO<sub>2</sub>-Loaded Aerogels with Biocide Effect. ACS Appl. Mater. Interfaces 2021, 13 (41), 49490–49499.

2. Kramarenko, A. S.; Chernyshov, I. Yu.; Pidko, E. A. Electric Double Layer Effect on the Outer-Sphere Benzyl Halides Electro-Reduction Mechanism. J. Phys. Chem. C 2024, 128 (23), 9462–9471.

3. Kramarenko, A. S.; Sharapa, D. I.; Pidko, E. A.; Studt, F. Ab Initio Kinetics of Electrochemical Reactions Using the Computational Fc<sup>0</sup>/Fc<sup>+</sup> Electrode. J. Phys. Chem. A 2024

4. Kramarenko, A. S.; Sharapa, D. I.; Pidko, E. A.; Studt, F. Kinetics of Dissociative Electron Transfer in Electrocarboxylation of Benzyl Chloride. 2024, *In preparation*

5. Kramarenko, A. S.; Sharapa, D. I.; Pidko, E. A.; Studt, F. Surface Charging Effect on Outer-Sphere Electron Transfer: A Strong Dependence on Supporting Electrolyte Concentration. 2024, *In preparation*

## **B Publication Associated with the Thesis**

1. Kramarenko, A. S.; Sharapa, D. I.; Pidko, E. A.; Studt, F. Ab Initio Kinetics of Electrochemical Reactions Using the Computational  $\text{Fc}^0/\text{Fc}^+$  Electrode. J. Phys. Chem. A 2024
2. Kramarenko, A. S.; Sharapa, D. I.; Pidko, E. A.; Studt, F. Kinetics of Dissociative Electron Transfer in Electrocarboxylation of Benzyl Chloride. 2024, *In preparation*
3. Kramarenko, A. S.; Sharapa, D. I.; Pidko, E. A.; Studt, F. Surface Charging Effect on Outer-Sphere Electron Transfer: A Strong Dependence on Supporting Electrolyte Concentration. 2024, *In preparation*

## **C      List of Conferences Associated with the Thesis**

1. DPG-Frühjahrstagung, 26-31 March 2023, Dresden
2. 15<sup>th</sup> European Congress on Catalysis, August 27 – September 1 2023, Prague
3. 57. Jahrestreffen Deutscher Katalytiker, 13 – 15 March 2024, Weimar
4. Workshop “New Developments in Quantum Chemistry”, 10-11 October 2024,  
Karlsruhe

## **D      Abbreviations**

MOFs – metal-organic frameworks

EC – electrocarboxylation

CVs – cyclic voltammograms

EDL – electric double layer

OHP – outer Helmholtz plane

CMH – classical Marcus-Hush model

SEP – standard equilibrium potential

DOS – Density of states

AEP – Absolute electrode potential

NIST - National Institute of Standards and Technology

MAE – Mean absolute error

UKS – unrestricted open-shell calculation

ROKS – restricted open-shell calculation

CFE – computational ferrocene electrode

IE – ionization energy

PNP – Poisson-Nernst-Planck model

DFT – Density functional theory

QSPR – quantitative-structure-property relation model

## **E      Acknowledgements**

I would like to express my sincere gratitude to Prof. Dr. Felix Studt for the invaluable opportunity to work in his research group. His relaxed yet insightful leadership approach and profound scientific expertise provided me with an exceptional foundation, not only for advancing my research but also for fostering my growth as a scientist. I am deeply grateful for his guidance, which helped me navigate both challenges and milestones throughout this journey.

Special thanks are also due to Prof. Dr. Evgeny Pidko and Dr. Dmitry Sharapa, whose expertise and dedication were instrumental in guiding me through the intricate process of the PhD. Their encouragement, constructive feedback, and patience have been invaluable, especially during pivotal stages of my research. I am fortunate to have had their mentorship, which has enriched my experience and contributed significantly to my development as a researcher.

Additionally, I would like to extend my heartfelt thanks to the German Academic Exchange Service (DAAD) for their generous financial support, which made this research possible. Their assistance enabled me to pursue this work with focus and dedication, and I am truly appreciative of the opportunities this support has provided.

Finally, I am grateful for the collaboration, insights, and support from my colleagues and friends, who have been a vital part of this journey. Their companionship and shared passion for scientific inquiry have made this experience both rewarding and memorable.

## **F Eidesstattliche Versicherung**

Bei dieser Dissertation handelt es sich um meine eigenständig erbrachte Leistung. Ich habe nur die angegebenen Quellen und Hilfsmittel benutzt und mich keiner unzulässigen Hilfe Dritter bedient. Insbesondere habe ich wörtlich oder sinngemäß aus anderen Werken übernommene Inhalte als solche kenntlich gemacht. Ich habe die "Regeln zur Sicherung guter wissenschaftlicher Praxis am Karlsruher Institut für Technologie (KIT)" beachtet. Die Arbeit oder Teile davon habe ich bislang nicht an einer Hochschule des In- oder Auslands als Bestandteil einer Prüfungs- oder Qualifikationsleistung vorgelegt. Die Richtigkeit der vorstehenden Erklärungen bestätige ich. Die Bedeutung der eidesstattlichen Versicherung die strafrechtlichen Folgen einer unrichtigen oder unvollständigen eidesstattlichen Versicherung sind mir bekannt. Ich versichere an Eides statt, dass ich nach bestem Wissen die reine Wahrheit erklärt und nichts verschwiegen habe.

## Bibliography

- (1) Mac Dowell, N.; Fennell, P. S.; Shah, N.; Maitland, G. C. The Role of CO<sub>2</sub> Capture and Utilization in Mitigating Climate Change. *Nature Clim Change* **2017**, 7 (4), 243–249. <https://doi.org/10.1038/nclimate3231>.
- (2) Ritchie, H.; Rosado, P.; Roser, M. CO<sub>2</sub> and Greenhouse Gas Emissions. *Our World in Data* **2023**.
- (3) Ou, Y.; Roney, C.; Alsalam, J.; Calvin, K.; Creason, J.; Edmonds, J.; Fawcett, A. A.; Kyle, P.; Narayan, K.; O'Rourke, P.; Patel, P.; Ragnauth, S.; Smith, S. J.; McJeon, H. Deep Mitigation of CO<sub>2</sub> and Non-CO<sub>2</sub> Greenhouse Gases toward 1.5 °C and 2 °C Futures. *Nat Commun* **2021**, 12 (1), 6245. <https://doi.org/10.1038/s41467-021-26509-z>.
- (4) Rahimi, M.; Khurram, A.; Hatton, T. A.; Gallant, B. Electrochemical Carbon Capture Processes for Mitigation of CO<sub>2</sub> Emissions. *Chem. Soc. Rev.* **2022**, 51 (20), 8676–8695. <https://doi.org/10.1039/D2CS00443G>.
- (5) Diercks, C. S.; Liu, Y.; Cordova, K. E.; Yaghi, O. M. The Role of Reticular Chemistry in the Design of CO<sub>2</sub> Reduction Catalysts. *Nature Mater* **2018**, 17 (4), 301–307. <https://doi.org/10.1038/s41563-018-0033-5>.
- (6) Huang, J. E.; Li, F.; Ozden, A.; Sedighian Rasouli, A.; García de Arquer, F. P.; Liu, S.; Zhang, S.; Luo, M.; Wang, X.; Lum, Y.; Xu, Y.; Bertens, K.; Miao, R. K.; Dinh, C.-T.; Sinton, D.; Sargent, E. H. CO<sub>2</sub> Electrolysis to Multicarbon Products in Strong Acid. *Science* **2021**, 372 (6546), 1074–1078. <https://doi.org/10.1126/science.abg6582>.
- (7) Nam, D.-H.; De Luna, P.; Rosas-Hernández, A.; Thevenon, A.; Li, F.; Agapie, T.; Peters, J. C.; Shekhah, O.; Eddaoudi, M.; Sargent, E. H. Molecular Enhancement of Heterogeneous CO<sub>2</sub> Reduction. *Nat. Mater.* **2020**, 19 (3), 266–276. <https://doi.org/10.1038/s41563-020-0610-2>.
- (8) Tian, S.; Yan, F.; Zhang, Z.; Jiang, J. Calcium-Looping Reforming of Methane Realizes in Situ CO<sub>2</sub> Utilization with Improved Energy Efficiency. *Science Advances* **2019**, 5 (4), eaav5077. <https://doi.org/10.1126/sciadv.aav5077>.
- (9) Belsa, B.; Xia, L.; Golovanova, V.; Polesso, B.; Pinilla-Sánchez, A.; San Martín, L.; Ye, J.; Dinh, C.-T.; García de Arquer, F. P. Materials Challenges on the Path to Gigatonne CO<sub>2</sub> Electrolysis. *Nat Rev Mater* **2024**, 1–15. <https://doi.org/10.1038/s41578-024-00696-9>.
- (10) Crandall, B. S.; Ko, B. H.; Overa, S.; Cherniack, L.; Lee, A.; Minnie, I.; Jiao, F. Kilowatt-Scale Tandem CO<sub>2</sub> Electrolysis for Enhanced Acetate and Ethylene Production. *Nat Chem Eng* **2024**, 1 (6), 421–429. <https://doi.org/10.1038/s44286-024-00076-8>.
- (11) Jang, J. H.; Kim, C.; Nayal, O. S.; Yeo, J. B.; Kim, G. R.; Kim, J.; Jo, Y. I.; Lee, U.; Kwon, M. S.; Nam, K. T. Electrochemically Initiated Synthesis of Ethylene Carbonate from CO<sub>2</sub>. *Nat. Synth* **2024**, 1–12. <https://doi.org/10.1038/s44160-024-00543-3>.
- (12) Lees, E. W.; Bui, J. C.; Romiluyi, O.; Bell, A. T.; Weber, A. Z. Exploring CO<sub>2</sub> Reduction and Crossover in Membrane Electrode Assemblies. *Nat Chem Eng* **2024**, 1 (5), 340–353. <https://doi.org/10.1038/s44286-024-00062-0>.
- (13) Melchionna, M.; Fornasiero, P.; Prato, M.; Bonchio, M. Electrocatalytic CO<sub>2</sub> Reduction: Role of the Cross-Talk at Nano-Carbon Interfaces. *Energy Environ. Sci.* **2021**, 14 (11), 5816–5833. <https://doi.org/10.1039/D1EE00228G>.
- (14) Rahimi, M.; Khurram, A.; Hatton, T. A.; Gallant, B. Electrochemical Carbon Capture Processes for Mitigation of CO<sub>2</sub> Emissions. *Chem. Soc. Rev.* **2022**, 51 (20), 8676–8695. <https://doi.org/10.1039/D2CS00443G>.
- (15) Xie, Y.; Ou, P.; Wang, X.; Xu, Z.; Li, Y. C.; Wang, Z.; Huang, J. E.; Wicks, J.; McCallum, C.; Wang, N.; Wang, Y.; Chen, T.; Lo, B. T. W.; Sinton, D.; Yu, J. C.; Wang, Y.; Sargent,



- E. H. High Carbon Utilization in CO<sub>2</sub> Reduction to Multi-Carbon Products in Acidic Media. *Nat Catal* **2022**, 5 (6), 564–570. <https://doi.org/10.1038/s41929-022-00788-1>.
- (16) Yang, B.; Chen, L.; Xue, S.; Sun, H.; Feng, K.; Chen, Y.; Zhang, X.; Xiao, L.; Qin, Y.; Zhong, J.; Deng, Z.; Jiao, Y.; Peng, Y. Electrocatalytic CO<sub>2</sub> Reduction to Alcohols by Modulating the Molecular Geometry and Cu Coordination in Bicentric Copper Complexes. *Nat Commun* **2022**, 13 (1), 5122. <https://doi.org/10.1038/s41467-022-32740-z>.
  - (17) Paired Electrochemical Process for the Capture and Conversion of CO<sub>2</sub> to Ethylene Carbonate. *Nat. Synth* **2024**, 1–2. <https://doi.org/10.1038/s44160-024-00544-2>.
  - (18) Navaee, A.; Salimi, A. Review on CO<sub>2</sub> Management: From CO<sub>2</sub> Sources, Capture, and Conversion to Future Perspectives of Gas-Phase Electrochemical Conversion and Utilization. *Energy Fuels* **2024**, 38 (4), 2708–2742. <https://doi.org/10.1021/acs.energyfuels.3c04269>.
  - (19) Azzi, M.; White, S. Emissions from Amine-Based Post-Combustion CO<sub>2</sub> Capture Plants. In *Absorption-Based Post-combustion Capture of Carbon Dioxide*; Feron, P. H. M., Ed.; Woodhead Publishing, 2016; pp 487–504. <https://doi.org/10.1016/B978-0-08-100514-9.00020-2>.
  - (20) Tan, L. S.; Shariff, A. M.; Lau, K. K.; Bustam, M. A. Factors Affecting CO<sub>2</sub> Absorption Efficiency in Packed Column: A Review. *Journal of Industrial and Engineering Chemistry* **2012**, 18 (6), 1874–1883. <https://doi.org/10.1016/j.jiec.2012.05.013>.
  - (21) Soo, X. Y. D.; Lee, J. J. C.; Wu, W.-Y.; Tao, L.; Wang, C.; Zhu, Q.; Bu, J. Advancements in CO<sub>2</sub> Capture by Absorption and Adsorption: A Comprehensive Review. *Journal of CO<sub>2</sub> Utilization* **2024**, 81, 102727. <https://doi.org/10.1016/j.jcou.2024.102727>.
  - (22) de Meyer, F.; Bignaud, C. The Use of Catalysis for Faster CO<sub>2</sub> Absorption and Energy-Efficient Solvent Regeneration: An Industry-Focused Critical Review. *Chemical Engineering Journal* **2022**, 428, 131264. <https://doi.org/10.1016/j.cej.2021.131264>.
  - (23) Khan, U.; Ogbaga, C. C.; Abiodun, O.-A. O.; Adeleke, A. A.; Ikubanni, P. P.; Okoye, P. U.; Okolie, J. A. Assessing Absorption-Based CO<sub>2</sub> Capture: Research Progress and Techno-Economic Assessment Overview. *Carbon Capture Science & Technology* **2023**, 8, 100125. <https://doi.org/10.1016/j.ccst.2023.100125>.
  - (24) Sanz-Pérez, E. S.; Murdock, C. R.; Didas, S. A.; Jones, C. W. Direct Capture of CO<sub>2</sub> from Ambient Air. *Chem. Rev.* **2016**, 116 (19), 11840–11876. <https://doi.org/10.1021/acs.chemrev.6b00173>.
  - (25) Wei, Y.-M.; Kang, J.-N.; Liu, L.-C.; Li, Q.; Wang, P.-T.; Hou, J.-J.; Liang, Q.-M.; Liao, H.; Huang, S.-F.; Yu, B. A Proposed Global Layout of Carbon Capture and Storage in Line with a 2 °C Climate Target. *Nat. Clim. Chang.* **2021**, 11 (2), 112–118. <https://doi.org/10.1038/s41558-020-00960-0>.
  - (26) Service, R. F. The Carbon Vault. *Science* **2020**, 369 (6508), 1156–1159. <https://doi.org/10.1126/science.369.6508.1156>.
  - (27) Zhang, C.; Ji, Y.; Li, C.; Zhang, Y.; Sun, S.; Xu, Y.; Jiang, L.; Wu, C. The Application of Biochar for CO<sub>2</sub> Capture: Influence of Biochar Preparation and CO<sub>2</sub> Capture Reactors. *Ind. Eng. Chem. Res.* **2023**, 62 (42), 17168–17181. <https://doi.org/10.1021/acs.iecr.3c00445>.
  - (28) Rajamathi, R.; Bhojaraj; Nethravathi, C. Porous CaO–MgO Nanostructures for CO<sub>2</sub> Capture. *ACS Appl. Nano Mater.* **2021**, 4 (10), 10969–10975. <https://doi.org/10.1021/acsanm.1c02428>.
  - (29) Pardakhti, M.; Jafari, T.; Tobin, Z.; Dutta, B.; Moharrer, E.; Shemshaki, N. S.; Suib, S.; Srivastava, R. Trends in Solid Adsorbent Materials Development for CO<sub>2</sub> Capture. *ACS Appl. Mater. Interfaces* **2019**, 11 (38), 34533–34559. <https://doi.org/10.1021/acsami.9b08487>.

- (30) Lv, G.; Li, S.; Zhang, H.; Qian, W.; Cheng, J.; Qian, P. CO<sub>2</sub> Adsorption on a K-Promoted MgO Surface: A DFT Theoretical Study. *Surface Science* **2024**, 749, 122575. <https://doi.org/10.1016/j.susc.2024.122575>.
- (31) Qu, T.; Zhang, J.; Song, J.; Jing, J.; Li, W.-Y. Promotional Effect of NaNO<sub>3</sub>/NaNO<sub>2</sub> on CO<sub>2</sub> Adsorption Performance of MgO Sorbents. *Chemical Engineering Science* **2024**, 299, 120503. <https://doi.org/10.1016/j.ces.2024.120503>.
- (32) Gui, C.; Wang, Z.; Ling, C.; Tang, Z. Molten Salt-Promoted MgO-Based CO<sub>2</sub> Adsorbents: Selective Adsorption on Polycrystalline Surfaces. *Journal of Environmental Chemical Engineering* **2024**, 12 (2), 111972. <https://doi.org/10.1016/j.jece.2024.111972>.
- (33) Lilian, M. J.; Bissessur, R.; Kang, K.; He, Q. S.; Hu, Y. Study of KOH-Activated Hydrochar for CO<sub>2</sub> Adsorption. *Journal of Industrial and Engineering Chemistry* **2024**. <https://doi.org/10.1016/j.jiec.2024.08.026>.
- (34) Wang, B.; Zeng, J.; He, H. Enhancing CO<sub>2</sub> Adsorption Capacity and Selectivity of UiO-67 through External Ligand Modification. *Separation and Purification Technology* **2025**, 354, 128651. <https://doi.org/10.1016/j.seppur.2024.128651>.
- (35) Ullah Khan, A.; Samuel, O.; Othman, M. H. D.; Younas, M.; Kamaludin, R.; Puteh, M. H.; Kurniawan, T. A.; Yinn Wong, K.; Kadir Khan, F.; Yoshida, N. Enhancing CO<sub>2</sub> Adsorption Selectivity of MOF-199: Investigating the Synergistic Effect of Mg Metal Doping and Polyethyleneimine Impregnation. *Separation and Purification Technology* **2024**, 347, 127511. <https://doi.org/10.1016/j.seppur.2024.127511>.
- (36) Lee, G.; Jhung, S. H. CO<sub>2</sub> Capture Using Functionalized MIL-101(Cr) Metal–Organic Frameworks: Functionality Nanoarchitectonics of Nanospace for CO<sub>2</sub> Adsorption. *Separation and Purification Technology* **2025**, 354, 129514. <https://doi.org/10.1016/j.seppur.2024.129514>.
- (37) Henrotin, A.; Heymans, N.; Duprez, M. E.; Mouchaham, G.; Serre, C.; Wong, D.; Robinson, R.; Mulrooney, D.; Casaban, J.; De Weireld, G. Lab-Scale Pilot for CO<sub>2</sub> Capture Vacuum Pressure Swing Adsorption: MIL-160(Al) vs Zeolite 13X. *Carbon Capture Science & Technology* **2024**, 12, 100224. <https://doi.org/10.1016/j.ccst.2024.100224>.
- (38) Missaoui, N.; Chrouda, A.; Bourguiba, F.; Serafin, J. Impact of Metal Precursor and Molar Ratios on Adsorption and Separation of CO<sub>2</sub> and CH<sub>4</sub> by SOD-ZIF-67 Prepared Using Green Solvent-Free Synthesis. *Fuel* **2024**, 378, 132840. <https://doi.org/10.1016/j.fuel.2024.132840>.
- (39) Giraldo, L.; Moreno-Piraján, J. C. Investigating Discrepancies in Adsorption Enthalpy Predictions: An Analysis of CO<sub>2</sub> Adsorption on HKUSTs. *Sustainable Chemistry for the Environment* **2024**, 8, 100161. <https://doi.org/10.1016/j.scenv.2024.100161>.
- (40) Aaron, D.; Tsouris, C. Separation of CO<sub>2</sub> from Flue Gas: A Review. *Separation Science and Technology* **2005**, 40 (1–3), 321–348. <https://doi.org/10.1081/SS-200042244>.
- (41) Ghasem, N. Polymeric Membranes for CO<sub>2</sub> Separation. In *Advances in Carbon Capture*; Rahimpour, M. R., Farsi, M., Makarem, M. A., Eds.; Woodhead Publishing, 2020; pp 311–329. <https://doi.org/10.1016/B978-0-12-819657-1.00014-1>.
- (42) Xu, X.; Wang, J.; Zhou, A.; Dong, S.; Shi, K.; Li, B.; Han, J.; O'Hare, D. High-Efficiency CO<sub>2</sub> Separation Using Hybrid LDH-Polymer Membranes. *Nat Commun* **2021**, 12 (1), 3069. <https://doi.org/10.1038/s41467-021-23121-z>.
- (43) Yave, W.; Car, A.; Funari, S. S.; Nunes, S. P.; Peinemann, K.-V. CO<sub>2</sub>-Philic Polymer Membrane with Extremely High Separation Performance. *Macromolecules* **2010**, 43 (1), 326–333. <https://doi.org/10.1021/ma901950u>.
- (44) Sun, S.; Wen, Y.; Huang, K. A New Ceramic–Carbonate Dual-Phase Membrane for High-Flux CO<sub>2</sub> Capture. *ACS Sustainable Chem. Eng.* **2021**, 9 (15), 5454–5460. <https://doi.org/10.1021/acssuschemeng.1c00860>.

- (45) Korelskiy, D.; Ye, P.; Fouladvand, S.; Karimi, S.; Sjöberg, E.; Hedlund, J. Efficient Ceramic Zeolite Membranes for CO<sub>2</sub>/H<sub>2</sub> Separation. *J. Mater. Chem. A* **2015**, *3* (23), 12500–12506. <https://doi.org/10.1039/C5TA02152A>.
- (46) Lei, L.; Bai, L.; Lindbråthen, A.; Pan, F.; Zhang, X.; He, X. Carbon Membranes for CO<sub>2</sub> Removal: Status and Perspectives from Materials to Processes. *Chemical Engineering Journal* **2020**, *401*, 126084. <https://doi.org/10.1016/j.cej.2020.126084>.
- (47) Chung, S. J.; Park, J. H.; Li, D.; Ida, J.-I.; Kumakiri, I.; Lin, J. Y. S. Dual-Phase Metal–Carbonate Membrane for High-Temperature Carbon Dioxide Separation. *Ind. Eng. Chem. Res.* **2005**, *44* (21), 7999–8006. <https://doi.org/10.1021/ie0503141>.
- (48) Fan, W.; Ying, Y.; Peh, S. B.; Yuan, H.; Yang, Z.; Yuan, Y. D.; Shi, D.; Yu, X.; Kang, C.; Zhao, D. Multivariate Polycrystalline Metal–Organic Framework Membranes for CO<sub>2</sub>/CH<sub>4</sub> Separation. *J. Am. Chem. Soc.* **2021**, *143* (42), 17716–17723. <https://doi.org/10.1021/jacs.1c08404>.
- (49) Hart, A.; Gnanendran, N. Cryogenic CO<sub>2</sub> Capture in Natural Gas. *Energy Procedia* **2009**, *1* (1), 697–706. <https://doi.org/10.1016/j.egypro.2009.01.092>.
- (50) Ghasem, N. CO<sub>2</sub> Removal from Natural Gas. In *Advances in Carbon Capture*; Rahimpour, M. R., Farsi, M., Makarem, M. A., Eds.; Woodhead Publishing, 2020; pp 479–501. <https://doi.org/10.1016/B978-0-12-819657-1.00021-9>.
- (51) Noble, B. B.; Norcott, P. L.; Hammill, C. L.; Ciampi, S.; Coote, M. L. Mechanism of Oxidative Alkoxyamine Cleavage: The Surprising Role of the Solvent and Supporting Electrolyte. *J. Phys. Chem. C* **2019**, *123* (16), 10300–10305. <https://doi.org/10.1021/acs.jpcc.9b01832>.
- (52) Matthessen, R.; Fransær, J.; Binnemans, K.; Vos, D. E. D. Electrocarboxylation: Towards Sustainable and Efficient Synthesis of Valuable Carboxylic Acids. *Beilstein J. Org. Chem.* **2014**, *10* (1), 2484–2500. <https://doi.org/10.3762/bjoc.10.260>.
- (53) Rau, G. H.; Willauer, H. D.; Ren, Z. J. The Global Potential for Converting Renewable Electricity to Negative-CO<sub>2</sub>-Emissions Hydrogen. *Nature Clim Change* **2018**, *8* (7), 621–625. <https://doi.org/10.1038/s41558-018-0203-0>.
- (54) Qin, Y.; Zhou, M.; Hao, Y.; Huang, X.; Tong, D.; Huang, L.; Zhang, C.; Cheng, J.; Gu, W.; Wang, L.; He, X.; Zhou, D.; Chen, Q.; Ding, A.; Zhu, T. Amplified Positive Effects on Air Quality, Health, and Renewable Energy under China's Carbon Neutral Target. *Nat. Geosci.* **2024**, *17* (5), 411–418. <https://doi.org/10.1038/s41561-024-01425-1>.
- (55) Lu, X.; Li, G.; Kim, J. Y.; Mei, D.; Lemmon, J. P.; Sprenkle, V. L.; Liu, J. Liquid-Metal Electrode to Enable Ultra-Low Temperature Sodium–Beta Alumina Batteries for Renewable Energy Storage. *Nat Commun* **2014**, *5* (1), 4578. <https://doi.org/10.1038/ncomms5578>.
- (56) Graziono, G. Homogeneous Catalysis: An Electrochemical and Spectroscopic Look at Renewable Energy. *Nat Rev Chem* **2018**, *2* (4), 1–1. <https://doi.org/10.1038/s41570-018-0130-0>.
- (57) Heard, D. M.; Lennox, A. J. J. Electrode Materials in Modern Organic Electrochemistry. *Angewandte Chemie International Edition* **2020**, *59* (43), 18866–18884. <https://doi.org/10.1002/anie.202005745>.
- (58) Medvedev, J. J.; Medvedeva, X. V.; Engelhardt, H.; Klinkova, A. Relative Activity of Metal Cathodes towards Electroorganic Coupling of CO<sub>2</sub> with Benzylic Halides. *Electrochimica Acta* **2021**, *387*, 138528. <https://doi.org/10.1016/j.electacta.2021.138528>.
- (59) Zhang, Z.; Wei, Z.; Sautet, P.; Alexandrova, A. N. Hydrogen-Induced Restructuring of a Cu(100) Electrode in Electroreduction Conditions. *J. Am. Chem. Soc.* **2022**, *144* (42), 19284–19293. <https://doi.org/10.1021/jacs.2c06188>.

- (60) Zhu, X.; Huang, J.; Eikerling, M. Electrochemical CO<sub>2</sub> Reduction at Silver from a Local Perspective. *ACS Catal.* **2021**, *11* (23), 14521–14532. <https://doi.org/10.1021/acscatal.1c04791>.
- (61) Li, J.; Tian, X.; Wang, X.; Zhang, T.; Spadaro, M. C.; Arbiol, J.; Li, L.; Zuo, Y.; Cabot, A. Electrochemical Conversion of Alcohols into Acidic Commodities on Nickel Sulfide Nanoparticles. *Inorg. Chem.* **2022**, *61* (34), 13433–13441. <https://doi.org/10.1021/acs.inorgchem.2c01695>.
- (62) Sinha, V.; Khramenkova, E.; Pidko, E. A. Solvent-Mediated Outer-Sphere CO<sub>2</sub> Electro-Reduction Mechanism over the Ag111 Surface. *Chem. Sci.* **2022**, *13* (13), 3803–3808. <https://doi.org/10.1039/D1SC07119J>.
- (63) Cheng, T.; Xiao, H.; Goddard, W. A. Free-Energy Barriers and Reaction Mechanisms for the Electrochemical Reduction of CO on the Cu(100) Surface, Including Multiple Layers of Explicit Solvent at pH 0. *J. Phys. Chem. Lett.* **2015**, *6* (23), 4767–4773. <https://doi.org/10.1021/acs.jpcllett.5b02247>.
- (64) Steinmann, S. N.; Michel, C.; Schwiedernoch, R.; Sautet, P. Impacts of Electrode Potentials and Solvents on the Electroreduction of CO<sub>2</sub>: A Comparison of Theoretical Approaches. *Phys. Chem. Chem. Phys.* **2015**, *17* (21), 13949–13963. <https://doi.org/10.1039/C5CP00946D>.
- (65) Hoekman, S. K.; Broch, A.; Robbins, C.; Purcell, R. CO<sub>2</sub> Recycling by Reaction with Renewably-Generated Hydrogen. *International Journal of Greenhouse Gas Control* **2010**, *4* (1), 44–50. <https://doi.org/10.1016/j.ijggc.2009.09.012>.
- (66) Wang, W.; Wang, S.; Ma, X.; Gong, J. Recent Advances in Catalytic Hydrogenation of Carbon Dioxide. *Chem. Soc. Rev.* **2011**, *40* (7), 3703–3727. <https://doi.org/10.1039/C1CS15008A>.
- (67) Silvestri, G.; Gambino, S.; Filardo, G.; Tiitta, M.; Sjöström, M.; Wold, S.; Berglind, R.; Karlsson, B. Use of Sacrificial Anodes in Synthetic Electrochemistry. Processes Involving Carbon Dioxide. *Acta Chem. Scand.* **1991**, *45*, 987–992. <https://doi.org/10.3891/acta.chem.scand.45-0987>.
- (68) Silvestri, G.; Scialdone, O. Recent Scientific and Technological Developments in Electrochemical Carboxylation Based on Carbon Dioxide. In *Carbon Dioxide as Chemical Feedstock*; John Wiley & Sons, Ltd, 2010; pp 317–334. <https://doi.org/10.1002/9783527629916.ch12>.
- (69) Tokuda, M. Efficient Fixation of Carbon Dioxide by Electrolysis — Facile Synthesis of Useful Carboxylic Acids —. *Journal of Natural Gas Chemistry* **2006**, *15* (4), 275–281. [https://doi.org/10.1016/S1003-9953\(07\)60006-1](https://doi.org/10.1016/S1003-9953(07)60006-1).
- (70) Neukermans, S.; Vorobjov, F.; Kenis, T.; De Wolf, R.; Hereijgers, J.; Breugelmans, T. Electrochemical Reduction of Halogenated Aromatic Compounds at Metal Cathodes in Acetonitrile. *Electrochimica Acta* **2020**, *332*, 135484. <https://doi.org/10.1016/j.electacta.2019.135484>.
- (71) Isse, A. A.; Arnaboldi, S.; Durante, C.; Gennaro, A. Electrochemical Reduction of Organic Bromides in 1-Butyl-3-Methylimidazolium Tetrafluoroborate. *Journal of Electroanalytical Chemistry* **2017**, *804*, 240–247. <https://doi.org/10.1016/j.jelechem.2017.09.023>.
- (72) Santos, E.; Schmickler, W. Models of Electron Transfer at Different Electrode Materials. *Chem. Rev.* **2022**, *122* (12), 10581–10598. <https://doi.org/10.1021/acs.chemrev.1c00583>.
- (73) Huang, Y.-F.; Wu, D.-Y.; Wang, A.; Ren, B.; Rondinini, S.; Tian, Z.-Q.; Amatore, C. Bridging the Gap between Electrochemical and Organometallic Activation: Benzyl Chloride Reduction at Silver Cathodes. *J. Am. Chem. Soc.* **2010**, *132* (48), 17199–17210. <https://doi.org/10.1021/ja106049c>.

- (74) Goodpaster, J. D.; Bell, A. T.; Head-Gordon, M. Identification of Possible Pathways for C–C Bond Formation during Electrochemical Reduction of CO<sub>2</sub>: New Theoretical Insights from an Improved Electrochemical Model. *J. Phys. Chem. Lett.* **2016**, *7* (8), 1471–1477. <https://doi.org/10.1021/acs.jpcclett.6b00358>.
- (75) Isse, A. A.; Gottardello, S.; Durante, C.; Gennaro, A. Dissociative Electron Transfer to Organic Chlorides: Electrocatalysis at Metal Cathodes. *Phys. Chem. Chem. Phys.* **2008**, *10* (17), 2409–2416. <https://doi.org/10.1039/B719936H>.
- (76) Derien, S.; Clinet, J. C.; Dunach, E.; Perichon, J. Activation of Carbon Dioxide: Nickel-Catalyzed Electrochemical Carboxylation of Diynes. *J. Org. Chem.* **1993**, *58* (9), 2578–2588. <https://doi.org/10.1021/jo00061a038>.
- (77) Derien, S.; Dunach, E.; Perichon, J. From Stoichiometry to Catalysis: Electroreductive Coupling of Alkynes and Carbon Dioxide with Nickel-Bipyridine Complexes. Magnesium Ions as the Key for Catalysis. *J. Am. Chem. Soc.* **1991**, *113* (22), 8447–8454. <https://doi.org/10.1021/ja00022a037>.
- (78) Köster, F.; Dinjus, E.; Duñach, E. Electrochemical Selective Incorporation of CO<sub>2</sub> into Terminal Alkynes and Diynes. *European Journal of Organic Chemistry* **2001**, *2001* (13), 2507–2511. [https://doi.org/10.1002/1099-0690\(200107\)2001:13<2507::AID-EJOC2507>3.0.CO;2-P](https://doi.org/10.1002/1099-0690(200107)2001:13<2507::AID-EJOC2507>3.0.CO;2-P).
- (79) Labbé, E.; Duñach, E.; Périchon, J. Ligand-Directed Reaction Products in the Nickel-Catalyzed Electrochemical Carboxylation of Terminal Alkynes. *Journal of Organometallic Chemistry* **1988**, *353* (3), C51–C56. [https://doi.org/10.1016/0022-328X\(88\)80330-9](https://doi.org/10.1016/0022-328X(88)80330-9).
- (80) Yuan, G.-Q.; Jiang, H.-F.; Lin, C.; Liao, S.-J. Efficient Electrochemical Synthesis of 2-Arylsuccinic Acids from CO<sub>2</sub> and Aryl-Substituted Alkenes with Nickel as the Cathode. *Electrochimica Acta* **2008**, *53* (5), 2170–2176. <https://doi.org/10.1016/j.electacta.2007.09.023>.
- (81) Orsini, M.; Feroci, M.; Sotgiu, G.; Inesi, A. Stereoselective Electrochemical Carboxylation: 2-Phenylsuccinates from Chiral Cinnamic Acid Derivatives. *Org. Biomol. Chem.* **2005**, *3* (7), 1202–1208. <https://doi.org/10.1039/B500570A>.
- (82) Gambino, S.; Silvestri, G. On the Electrochemical Reduction of Carbon Dioxide and Ethylene. *Tetrahedron Letters* **1973**, *14* (32), 3025–3028. [https://doi.org/10.1016/S0040-4039\(01\)96310-5](https://doi.org/10.1016/S0040-4039(01)96310-5).
- (83) Tyssee, D. A.; Baizer, M. M. Electrocarboxylation. I. Mono- and Dicarboxylation of Activated Olefins. *J. Org. Chem.* **1974**, *39* (19), 2819–2823. <https://doi.org/10.1021/jo00933a001>.
- (84) Wang, H.; Du, Y.-F.; Lin, M.-Y.; Zhang, K.; Lu, J.-X. Electrochemical Reduction and Carboxylation of Ethyl Cinnamate in MeCN. *Chinese Journal of Chemistry* **2008**, *26* (9), 1745–1748. <https://doi.org/10.1002/cjoc.200890316>.
- (85) Zhong, J.-S.; Yang, Z.-X.; Ding, C.-L.; Huang, Y.-F.; Zhao, Y.; Yan, H.; Ye, K.-Y. Desulfonylative Electrocarboxylation with Carbon Dioxide. *J. Org. Chem.* **2021**, *86* (22), 16162–16170. <https://doi.org/10.1021/acs.joc.1c01261>.
- (86) Zhang, Y.; Vanderghinste, J.; Wang, J.; Das, S. Challenges and Recent Advancements in the Synthesis of  $\alpha,\alpha$ -Disubstituted  $\alpha$ -Amino Acids. *Nat Commun* **2024**, *15* (1), 1474. <https://doi.org/10.1038/s41467-024-45790-2>.
- (87) Yao, H.; Wang, M.-Y.; Yue, C.; Feng, B.; Ji, W.; Qian, C.; Wang, S.; Zhang, S.; Ma, X. Electrocarboxylation of CO<sub>2</sub> with Organic Substrates: Toward Cathodic Reaction. *Trans. Tianjin Univ.* **2023**, *29* (4), 254–274. <https://doi.org/10.1007/s12209-023-00361-2>.
- (88) Sun, G.-Q.; Zhang, W.; Liao, L.-L.; Li, L.; Nie, Z.-H.; Wu, J.-G.; Zhang, Z.; Yu, D.-G. Nickel-Catalyzed Electrochemical Carboxylation of Unactivated Aryl and Alkyl Halides

- with CO<sub>2</sub>. *Nat Commun* **2021**, *12* (1), 7086. <https://doi.org/10.1038/s41467-021-27437-8>.
- (89) Batista, G. M. F.; Ebenbauer, R.; Day, C.; Bergare, J.; Neumann, K. T.; Hopmann, K. H.; Elmore, C. S.; Rosas-Hernández, A.; Skrydstrup, T. Efficient Palladium-Catalyzed Electrocarboxylation Enables Late-Stage Carbon Isotope Labelling. *Nat Commun* **2024**, *15* (1), 2592. <https://doi.org/10.1038/s41467-024-46820-9>.
  - (90) Wang, H.; Zhu, H.-W.; Guo, R.-R.; Hu, Q.-L.; Zeng, S.; Lu, J.-X. Computational and Experimental Study on Electrocarboxylation of Benzalacetone. *Asian Journal of Organic Chemistry* **2017**, *6* (10), 1380–1384. <https://doi.org/10.1002/ajoc.201700233>.
  - (91) Kramarenko, A. S.; Chernyshov, I. Yu.; Pidko, E. A. Electric Double Layer Effect on the Outer-Sphere Benzyl Halides Electro-Reduction Mechanism. *J. Phys. Chem. C* **2024**, *128* (23), 9462–9471. <https://doi.org/10.1021/acs.jpcc.3c08224>.
  - (92) Mena, S.; Sanchez, J.; Guirado, G. Electrocarboxylation of 1-Chloro-(4-Isobutylphenyl)Ethane with a Silver Cathode in Ionic Liquids: An Environmentally Benign and Efficient Way to Synthesize Ibuprofen. *RSC Adv.* **2019**, *9* (26), 15115–15123. <https://doi.org/10.1039/C9RA01781J>.
  - (93) Cao, Y.; He, X.; Wang, N.; Li, H.-R.; He, L.-N. Photochemical and Electrochemical Carbon Dioxide Utilization with Organic Compounds. *Chinese Journal of Chemistry* **2018**, *36* (7), 644–659. <https://doi.org/10.1002/cjoc.201700742>.
  - (94) Batanero, B.; Barba, F.; Sánchez-Sánchez, C. M.; Aldaz, A. Paired Electrosynthesis of Cyanoacetic Acid. *J. Org. Chem.* **2004**, *69* (7), 2423–2426. <https://doi.org/10.1021/jo0358473>.
  - (95) Isse, A. A.; Gennaro, A. Electrochemical Synthesis of Cyanoacetic Acid from Chloroacetonitrile and Carbon Dioxide. *J. Electrochem. Soc.* **2002**, *149* (8), D113. <https://doi.org/10.1149/1.1490358>.
  - (96) Rossi, L. Electrochemical Methodologies for the Carboxylation Reactions in Organic Synthesis. An Alternative Re-Use of Carbon Dioxide. *Current Green Chemistry* **2** (1), 77–89. <https://doi.org/10.2174/2213346101666140804222344>.
  - (97) Yan, M.; Kawamata, Y.; Baran, P. S. Synthetic Organic Electrochemical Methods Since 2000: On the Verge of a Renaissance. *Chem. Rev.* **2017**, *117* (21), 13230–13319. <https://doi.org/10.1021/acs.chemrev.7b00397>.
  - (98) Medvedev, J. J.; Medvedeva, X. V.; Li, F.; Zienchuk, T. A.; Klinkova, A. Electrochemical CO<sub>2</sub> Fixation to  $\alpha$ -Methylbenzyl Bromide in Divided Cells with Nonsacrificial Anodes and Aqueous Anolytes. *ACS Sustainable Chem. Eng.* **2019**, *7* (24), 19631–19639. <https://doi.org/10.1021/acssuschemeng.9b04647>.
  - (99) Wu, L.-X.; Sun, Q.-L.; Yang, M.-P.; Zhao, Y.-G.; Guan, Y.-B.; Wang, H.; Lu, J.-X. Highly Efficient Electrocatalytic Carboxylation of 1-Phenylethyl Chloride at Cu Foam Cathode. *Catalysts* **2018**, *8* (7), 273. <https://doi.org/10.3390/catal8070273>.
  - (100) Yang, H.-P.; Zhang, H.-W.; Wu, Y.; Fan, L.-D.; Chai, X.-Y.; Zhang, Q.-L.; Liu, J.-H.; He, C.-X. A Core–Shell-Structured Silver Nanowire/Nitrogen-Doped Carbon Catalyst for Enhanced and Multifunctional Electrofixation of CO<sub>2</sub>. *ChemSusChem* **2018**, *11* (22), 3905–3910. <https://doi.org/10.1002/cssc.201801612>.
  - (101) Yang, H.; Wu, L.; Wang, H.; Lu, J. Cathode Made of Compacted Silver Nanoparticles for Electrocatalytic Carboxylation of 1-Phenethyl Bromide with CO<sub>2</sub>. *Chinese Journal of Catalysis* **2016**, *37* (7), 994. [https://doi.org/10.1016/S1872-2067\(15\)61075-0](https://doi.org/10.1016/S1872-2067(15)61075-0).
  - (102) Yang, H.-P.; Yue, Y.-N.; Sun, Q.-L.; Feng, Q.; Wang, H.; Lu, J.-X. Entrapment of a Chiral Cobalt Complex within Silver: A Novel Heterogeneous Catalyst for Asymmetric Carboxylation of Benzyl Bromides with CO<sub>2</sub>. *Chem. Commun.* **2015**, *51* (61), 12216–12219. <https://doi.org/10.1039/C5CC04554A>.

- (103) Luo, P.-P.; Zhang, Y.-T.; Chen, B.-L.; Yu, S.-X.; Zhou, H.-W.; Qu, K.-G.; Kong, Y.-X.; Huang, X.-Q.; Zhang, X.-X.; Lu, J.-X. Electrocarboxylation of Dichlorobenzenes on a Silver Electrode in DMF. *Catalysts* **2017**, *7* (9), 274. <https://doi.org/10.3390/catal7090274>.
- (104) Scialdone, O.; Galia, A.; Belfiore, C.; Filardo, G.; Silvestri, G. Influence of the Experimental System and Optimization of the Selectivity for the Electrocarboxylation of Chloroacetonitrile to Cyanoacetic Acid. *Ind. Eng. Chem. Res.* **2004**, *43* (17), 5006–5014. <https://doi.org/10.1021/ie034275+>.
- (105) Datta, A. K.; Marron, P. A.; King, C. J. H.; Wagenknecht, J. H. Process Development for Electrocarboxylation of 2-Acetyl-6-Methoxynaphthalene. *Journal of Applied Electrochemistry* **1998**, *28* (6), 569–577. <https://doi.org/10.1023/A:1003289800341>.
- (106) van Tilborg, W. J. M.; Smit, C. J. The Electrosynthesis of Carboxylic Acids from Carbon Dioxide and Butadiene. *Recueil des Travaux Chimiques des Pays-Bas* **1981**, *100* (11), 437–438. <https://doi.org/10.1002/recl.19811001113>.
- (107) Grinberg, V. A.; Koch, T. A.; Mazin, V. M.; Mysov, E. I.; Sterlin, S. R. Electrochemical Reduction of CO<sub>2</sub> in the Presence of 1,3-Butadiene Using a Hydrogen Anode in a Nonaqueous Medium. *Russ Chem Bull* **1999**, *48* (2), 294–299. <https://doi.org/10.1007/BF02494552>.
- (108) Matthessen, R.; Fransaer, J.; Binnemans, K.; De Vos, D. E. Paired Electrosynthesis of Diacid and Diol Precursors Using Dienes and CO<sub>2</sub> as the Carbon Source. *ChemElectroChem* **2015**, *2* (1), 73–76. <https://doi.org/10.1002/celec.201402299>.
- (109) Kurchin, R.; Viswanathan, V. Marcus–Hush–Chidsey Kinetics at Electrode–Electrolyte Interfaces. *The Journal of Chemical Physics* **2020**, *153* (13), 134706. <https://doi.org/10.1063/5.0023611>.
- (110) Henstridge, M. C.; Laborda, E.; Compton, R. G. Asymmetric Marcus–Hush Model of Electron Transfer Kinetics: Application to the Voltammetry of Surface-Bound Redox Systems. *Journal of Electroanalytical Chemistry* **2012**, *674*, 90–96. <https://doi.org/10.1016/j.jelechem.2012.04.006>.
- (111) Marcus, R. A. Symmetry or Asymmetry of k<sub>ET</sub> and i<sub>STM</sub> vs. Potential Curves. *J. Chem. Soc., Faraday Trans.* **1996**, *92* (20), 3905–3908. <https://doi.org/10.1039/FT9969203905>.
- (112) Warburton, R. E.; Soudackov, A. V.; Hammes-Schiffer, S. Theoretical Modeling of Electrochemical Proton-Coupled Electron Transfer. *Chem. Rev.* **2022**, *122* (12), 10599–10650. <https://doi.org/10.1021/acs.chemrev.1c00929>.
- (113) Bard, A. J.; Faulkner, L. R. *Electrochemical Methods: Fundamentals and Applications*, 2nd ed.; Wiley, 2001.
- (114) Chen, S.; Liu, Y.; Chen, J. Heterogeneous Electron Transfer at Nanoscopic Electrodes: Importance of Electronic Structures and Electric Double Layers. *Chem. Soc. Rev.* **2014**, *43* (15), 5372–5386. <https://doi.org/10.1039/C4CS00087K>.
- (115) Huang, J.; Chen, S.; Eikerling, M. Grand-Canonical Model of Electrochemical Double Layers from a Hybrid Density–Potential Functional. *J. Chem. Theory Comput.* **2021**, *17* (4), 2417–2430. <https://doi.org/10.1021/acs.jctc.1c00098>.
- (116) Huang, J. Hybrid Density-Potential Functional Theory of Electric Double Layers. *Electrochimica Acta* **2021**, *389*, 138720. <https://doi.org/10.1016/j.electacta.2021.138720>.
- (117) Huang, J.; Li, P.; Chen, S. Potential of Zero Charge and Surface Charging Relation of Metal–Solution Interphases from a Constant-Potential Jellium–Poisson–Boltzmann Model. *Phys. Rev. B* **2020**, *101* (12), 125422. <https://doi.org/10.1103/PhysRevB.101.125422>.

- (118) Johnson, E. F.; Boutin, E.; Haussener, S. Surface Charge Boundary Condition Often Misused in CO<sub>2</sub> Reduction Models. *J. Phys. Chem. C* **2023**, *127* (37), 18784–18790. <https://doi.org/10.1021/acs.jpcc.3c05364>.
- (119) Jensen, F. *Introduction to Computational Chemistry*, 3rd ed.; Wiley: Chichester, UK ; Hoboken, NJ, 2017.
- (120) Martin, R. M. *Electronic Structure: Basic Theory and Practical Methods*, 2nd ed.; Cambridge University Press: Cambridge, United Kingdom ; New York, NY, 2020.
- (121) Frenkel, D.; Smit, B. *Understanding Molecular Simulation: From Algorithms to Applications*, 3rd ed.; Academic Press: London San Diego, CA Cambridge, MA Kidlington, 2023.
- (122) Koch, W. *A Chemist's Guide to Density Functional Theory 2e*, 2nd ed.; John Wiley & Sons: Weinheim, 2001.
- (123) Chen, J.-L.; Kaltsoyannis, N. DFT + U Study of Uranium Dioxide and Plutonium Dioxide with Occupation Matrix Control. *J. Phys. Chem. C* **2022**, *126* (27), 11426–11435. <https://doi.org/10.1021/acs.jpcc.2c03804>.
- (124) Blaško, M.; Pašteka, L. F.; Urban, M. DFT Functionals for Modeling of Polyethylene Chains Cross-Linked by Metal Atoms. DLPNO–CCSD(T) Benchmark Calculations. *J. Phys. Chem. A* **2021**, *125* (34), 7382–7395. <https://doi.org/10.1021/acs.jpca.1c04793>.
- (125) Chamkin, A. A.; Serkova, E. S. DFT, DLPNO-CCSD(T), and NEVPT2 Benchmark Study of the Reaction between Ferrocenium and Trimethylphosphine. *Journal of Computational Chemistry* **2020**, *41* (28), 2388–2397. <https://doi.org/10.1002/jcc.26398>.
- (126) Busch, M.; Ahlberg, E.; Ahlberg, E.; Laasonen, K. How to Predict the pK<sub>a</sub> of Any Compound in Any Solvent. *ACS Omega* **2022**, *7* (20), 17369–17383. <https://doi.org/10.1021/acsomega.2c01393>.
- (127) Busch, M.; Laasonen, K.; Ahlberg, E. Method for the Accurate Prediction of Electron Transfer Potentials Using an Effective Absolute Potential. *Phys. Chem. Chem. Phys.* **2020**, *22* (44), 25833–25840. <https://doi.org/10.1039/D0CP04508J>.
- (128) Gosser, D. *Cyclic Voltammetry: Simulation and Analysis of Reaction Mechanisms*; 1993.
- (129) Tanner, E. E. L.; Barnes, E. O.; Tickell, C. B.; Goodrich, P.; Hardacre, C.; Compton, R. G. Application of Asymmetric Marcus–Hush Theory to Voltammetry in Room-Temperature Ionic Liquids. *J. Phys. Chem. C* **2015**, *119* (13), 7360–7370. <https://doi.org/10.1021/acs.jpcc.5b01174>.
- (130) Brown, J. H. Development and Use of a Cyclic Voltammetry Simulator To Introduce Undergraduate Students to Electrochemical Simulations. *J. Chem. Educ.* **2015**, *92* (9), 1490–1496. <https://doi.org/10.1021/acs.jchemed.5b00225>.
- (131) Bohra, D.; Chaudhry, J. H.; Burdyny, T.; Pidko, E. A.; Smith, W. A. Modeling the Electrical Double Layer to Understand the Reaction Environment in a CO<sub>2</sub> Electrocatalytic System. *Energy Environ. Sci.* **2019**, *12* (11), 3380–3389. <https://doi.org/10.1039/C9EE02485A>.
- (132) Levey, K. J.; Edwards, M. A.; White, H. S.; Macpherson, J. V. Finite Element Modeling of the Combined Faradaic and Electrostatic Contributions to the Voltammetric Response of Monolayer Redox Films. *Anal. Chem.* **2022**, *94* (37), 12673–12682. <https://doi.org/10.1021/acs.analchem.2c01976>.
- (133) Dickinson, E. J. F.; Limon-Petersen, J. G.; Rees, N. V.; Compton, R. G. How Much Supporting Electrolyte Is Required to Make a Cyclic Voltammetry Experiment Quantitatively “Diffusional”? A Theoretical and Experimental Investigation. *J. Phys. Chem. C* **2009**, *113* (25), 11157–11171. <https://doi.org/10.1021/jp901628h>.
- (134) Wang, H.; Thiele, A.; Pilon, L. Simulations of Cyclic Voltammetry for Electric Double Layers in Asymmetric Electrolytes: A Generalized Modified Poisson–Nernst–Planck



- Model. *J. Phys. Chem. C* **2013**, *117* (36), 18286–18297. <https://doi.org/10.1021/jp402181e>.
- (135) Hou, Y.; Aoki, K. J.; Chen, J.; Nishiumi, T. Solvent Variables Controlling Electric Double Layer Capacitance at the Metal–Solution Interface. *J. Phys. Chem. C* **2014**, *118* (19), 10153–10158. <https://doi.org/10.1021/jp5018289>.
- (136) Li, S.; Yu, A.; Toledo, F.; Han, Z.; Wang, H.; He, H. Y.; Wu, R.; Ho, W. Rotational and Vibrational Excitations of a Hydrogen Molecule Trapped within a Nanocavity of Tunable Dimension. *Phys. Rev. Lett.* **2013**, *111* (14), 146102. <https://doi.org/10.1103/PhysRevLett.111.146102>.
- (137) Sprowl, L. H.; Campbell, C. T.; Árnadóttir, L. Hindered Translator and Hindered Rotor Models for Adsorbates: Partition Functions and Entropies. *J. Phys. Chem. C* **2016**, *120* (18), 9719–9731. <https://doi.org/10.1021/acs.jpcc.5b11616>.
- (138) Campbell, C. T.; Sprowl, L. H.; Árnadóttir, L. Equilibrium Constants and Rate Constants for Adsorbates: Two-Dimensional (2D) Ideal Gas, 2D Ideal Lattice Gas, and Ideal Hindered Translator Models. *J. Phys. Chem. C* **2016**, *120* (19), 10283–10297. <https://doi.org/10.1021/acs.jpcc.6b00975>.
- (139) Huber, P. *Dehydration and Decarboxylation Reactions in Brønsted and Lewis Acidic Zeolites*. <https://doi.org/10.5445/IR/1000167714>.
- (140) Laborda, E.; C. Henstridge, M.; Batchelor-McAuley, C.; G. Compton, R. Asymmetric Marcus–Hush Theory for Voltammetry. *Chemical Society Reviews* **2013**, *42* (12), 4894–4905. <https://doi.org/10.1039/C3CS35487C>.
- (141) Silverstein, T. P. Marcus Theory: Thermodynamics CAN Control the Kinetics of Electron Transfer Reactions. *J. Chem. Educ.* **2012**, *89* (9), 1159–1167. <https://doi.org/10.1021/ed1007712>.
- (142) Laborda, E.; Henstridge, M. C.; Compton, R. G. Asymmetric Marcus Theory: Application to Electrode Kinetics. *Journal of Electroanalytical Chemistry* **2012**, *667*, 48–53. <https://doi.org/10.1016/j.jelechem.2011.12.011>.
- (143) Trasatti, S. The Absolute Electrode Potential: An Explanatory Note (Recommendations 1986). *Pure and Applied Chemistry* **1986**, *58* (7), 955–966. <https://doi.org/10.1351/pac198658070955>.
- (144) Ghosh, S.; Hammes-Schiffer, S. Calculation of Electrochemical Reorganization Energies for Redox Molecules at Self-Assembled Monolayer Modified Electrodes. *J. Phys. Chem. Lett.* **2015**, *6* (1), 1–5. <https://doi.org/10.1021/jz5023784>.
- (145) Ghosh, S.; Horvath, S.; Soudackov, A. V.; Hammes-Schiffer, S. Electrochemical Solvent Reorganization Energies in the Framework of the Polarizable Continuum Model. *J. Chem. Theory Comput.* **2014**, *10* (5), 2091–2102. <https://doi.org/10.1021/ct500051e>.
- (146) Isse, A. A.; Lin, C. Y.; Coote, M. L.; Gennaro, A. Estimation of Standard Reduction Potentials of Halogen Atoms and Alkyl Halides. *J. Phys. Chem. B* **2011**, *115* (4), 678–684. <https://doi.org/10.1021/jp109613t>.
- (147) Isse, A. A.; Falcioia, L.; Mussini, P. R.; Gennaro, A. Relevance of Electron Transfer Mechanism in Electrocatalysis: The Reduction of Organic Halides at Silver Electrodes. *Chem. Commun.* **2006**, No. 3, 344–346. <https://doi.org/10.1039/B513801A>.
- (148) Isse, A. A.; Scarpa, L.; Durante, C.; Gennaro, A. Reductive Cleavage of Carbon–Chlorine Bonds at Catalytic and Non-Catalytic Electrodes in 1-Butyl-3-Methylimidazolium Tetrafluoroborate. *Phys. Chem. Chem. Phys.* **2015**, *17* (46), 31228–31236. <https://doi.org/10.1039/C5CP04142B>.
- (149) Savéant, J.-M.; Tessier, D. Variation of the Electrochemical Transfer Coefficient with Potential. *Faraday Discuss. Chem. Soc.* **1982**, *74* (0), 57–72. <https://doi.org/10.1039/DC9827400057>.

- (150) Marcus, Y. Thermodynamics of Solvation of Ions. Part 5.—Gibbs Free Energy of Hydration at 298.15 K. *J. Chem. Soc., Faraday Trans.* **1991**, 87 (18), 2995–2999. <https://doi.org/10.1039/FT9918702995>.
- (151) Marcus, R. A. On the Theory of Oxidation-Reduction Reactions Involving Electron Transfer. I. *The Journal of Chemical Physics* **2004**, 24 (5), 966–978. <https://doi.org/10.1063/1.1742723>.
- (152) Sowa, J. K.; Mol, J. A.; Gauger, E. M. Marcus Theory of Thermoelectricity in Molecular Junctions. *J. Phys. Chem. C* **2019**, 123 (7), 4103–4108. <https://doi.org/10.1021/acs.jpcc.8b12163>.
- (153) Zeng, Y.; Bai, P.; Smith, R. B.; Bazant, M. Z. Simple Formula for Asymmetric Marcus–Hush Kinetics. *Journal of Electroanalytical Chemistry* **2015**, 748, 52–57. <https://doi.org/10.1016/j.jelechem.2015.04.018>.
- (154) Andrés, G. O.; Martínez-Junza, V.; Crovetto, L.; Braslavsky, S. E. Photoinduced Electron Transfer from Tetrasulfonated Porphyrin to Benzoquinone Revisited. The Structural Volume-Normalized Entropy Change Correlates with Marcus Reorganization Energy. *J. Phys. Chem. A* **2006**, 110 (34), 10185–10190. <https://doi.org/10.1021/jp062579e>.
- (155) Neese, F. The ORCA Program System. *WIREs Computational Molecular Science* **2012**, 2 (1), 73–78. <https://doi.org/10.1002/wcms.81>.
- (156) Neese, F. Software Update: The ORCA Program System—Version 5.0. *WIREs Computational Molecular Science* **2022**, 12 (5), e1606. <https://doi.org/10.1002/wcms.1606>.
- (157) Neese, F.; Wennmohs, F.; Becker, U.; Riplinger, C. The ORCA Quantum Chemistry Program Package. *J. Chem. Phys.* **2020**, 152 (22), 224108. <https://doi.org/10.1063/5.0004608>.
- (158) Weigend, F. Accurate Coulomb-Fitting Basis Sets for H to Rn. *Phys. Chem. Chem. Phys.* **2006**, 8 (9), 1057–1065. <https://doi.org/10.1039/B515623H>.
- (159) Krack, M. Pseudopotentials for H to Kr Optimized for Gradient-Corrected Exchange-Correlation Functionals. *Theor. Chem. Acc.* **2005**, 114 (1), 145–152. <https://doi.org/10.1007/s00214-005-0655-y>.
- (160) Toma, M.; Kuvek, T.; Vrček, V. Ionization Energy and Reduction Potential in Ferrocene Derivatives: Comparison of Hybrid and Pure DFT Functionals. *J. Phys. Chem. A* **2020**, 124 (39), 8029–8039. <https://doi.org/10.1021/acs.jpca.0c06663>.
- (161) Yang, Y.; Yu, L. Theoretical Investigations of Ferrocene/Ferrocenium Solvation in Imidazolium-Based Room-Temperature Ionic Liquids. *Phys. Chem. Chem. Phys.* **2013**, 15 (8), 2669–2683. <https://doi.org/10.1039/C2CP42876H>.
- (162) Wang, Y.; Rogers, E. I.; Compton, R. G. The Measurement of the Diffusion Coefficients of Ferrocene and Ferrocenium and Their Temperature Dependence in Acetonitrile Using Double Potential Step Microdisk Electrode Chronoamperometry. *Journal of Electroanalytical Chemistry* **2010**, 648 (1), 15–19. <https://doi.org/10.1016/j.jelechem.2010.07.006>.
- (163) Warratz, R.; Aboulfadl, H.; Bally, T.; Tuzek, F. Electronic Structure and Absorption Spectra of Biferrocenyl and Bisfulvalenide Diiron Radical Cations: Detection and Assignment of New Low-Energy Transitions. *Chemistry - A European Journal* **2009**, 15, 1604. <https://doi.org/10.1002/chem.200801054>.
- (164) Tsierkezos, N. G. Cyclic Voltammetric Studies of Ferrocene in Nonaqueous Solvents in the Temperature Range from 248.15 to 298.15 K. *J. Solution Chem.* **2007**, 36 (3), 289–302. <https://doi.org/10.1007/s10953-006-9119-9>.
- (165) Smalley, J. F.; Sachs, S. B.; Chidsey, C. E. D.; Dudek, S. P.; Sikes, H. D.; Creager, S. E.; Yu, C. J.; Feldberg, S. W.; Newton, M. D. Interfacial Electron-Transfer Kinetics of

- Ferrocene through Oligophenyleneethynylene Bridges Attached to Gold Electrodes as Constituents of Self-Assembled Monolayers: Observation of a Nonmonotonic Distance Dependence. *J. Am. Chem. Soc.* **2004**, *126* (44), 14620–14630. <https://doi.org/10.1021/ja047458b>.
- (166) Smalley, J. F.; Finklea, H. O.; Chidsey, C. E. D.; Linford, M. R.; Creager, S. E.; Ferraris, J. P.; Chalfant, K.; Zawodzinski, T.; Feldberg, S. W.; Newton, M. D. Heterogeneous Electron-Transfer Kinetics for Ruthenium and Ferrocene Redox Moieties through Alkanethiol Monolayers on Gold. *J. Am. Chem. Soc.* **2003**, *125* (7), 2004–2013. <https://doi.org/10.1021/ja028458j>.
- (167) Seto, K.; Nakayama, T.; Uno, B. Formal Redox Potentials of Organic Molecules in Ionic Liquids on the Basis of Quaternary Nitrogen Cations as Adiabatic Electron Affinities. *J. Phys. Chem. B* **2013**, *117* (37), 10834–10845. <https://doi.org/10.1021/jp402457k>.
- (168) Randviir, E. P. A Cross Examination of Electron Transfer Rate Constants for Carbon Screen-Printed Electrodes Using Electrochemical Impedance Spectroscopy and Cyclic Voltammetry. *Electrochimica Acta* **2018**, *286*, 179–186. <https://doi.org/10.1016/j.electacta.2018.08.021>.
- (169) Radtke, V.; Priester, D.; Heering, A.; Müller, C.; Koslowski, T.; Leito, I.; Krossing, I. The Unified Redox Scale for All Solvents: Consistency and Gibbs Transfer Energies of Electrolytes from Their Constituent Single Ions. *Chemistry – A European Journal* **2023**, *29* (46), e202300609. <https://doi.org/10.1002/chem.202300609>.
- (170) Qu, X.; Persson, K. A. Toward Accurate Modeling of the Effect of Ion-Pair Formation on Solute Redox Potential. *J. Chem. Theory Comput.* **2016**, *12* (9), 4501–4508. <https://doi.org/10.1021/acs.jctc.6b00289>.
- (171) Pavlishchuk, V. V.; Addison, A. W. Conversion Constants for Redox Potentials Measured versus Different Reference Electrodes in Acetonitrile Solutions at 25°C. *Inorganica Chimica Acta* **2000**, *298* (1), 97–102. [https://doi.org/10.1016/S0020-1693\(99\)00407-7](https://doi.org/10.1016/S0020-1693(99)00407-7).
- (172) Nikitina, V. A.; Kislenko, S. A.; Nazmutdinov, R. R.; Bronshtein, M. D.; Tsirlina, G. A. Ferrocene/Ferrocenium Redox Couple at Au(111)/Ionic Liquid and Au(111)/Acetonitrile Interfaces: A Molecular-Level View at the Elementary Act. *J. Phys. Chem. C* **2014**, *118* (12), 6151–6164. <https://doi.org/10.1021/jp4072108>.
- (173) Namazian, M.; Lin, C. Y.; Coote, M. L. Benchmark Calculations of Absolute Reduction Potential of Ferricinium/Ferrocene Couple in Nonaqueous Solutions. *J. Chem. Theory Comput.* **2010**, *6* (9), 2721–2725. <https://doi.org/10.1021/ct1003252>.
- (174) Mugisa, J.; Chukwu, R.; Brogioli, D.; La Mantia, F. Effect of Ion-Pairing on the Kinetics of Redox Systems with Concentrated Supporting Electrolyte. *Electrochimica Acta* **2024**, *473*, 143473. <https://doi.org/10.1016/j.electacta.2023.143473>.
- (175) Makoś, M. Z.; Gurunathan, P. K.; Raugei, S.; Kowalski, K.; Glezakou, V.-A.; Rousseau, R. Modeling Absolute Redox Potentials of Ferrocene in the Condensed Phase. *J. Phys. Chem. Lett.* **2022**, *13* (42), 10005–10010. <https://doi.org/10.1021/acs.jpcllett.2c02447>.
- (176) Kim, D. Y.; Yang, J. C.; Kim, H. W.; Swain, G. M. Heterogeneous Electron-Transfer Rate Constants for Ferrocene and Ferrocene Carboxylic Acid at Boron-Doped Diamond Electrodes in a Room Temperature Ionic Liquid. *Electrochimica Acta* **2013**, *94*, 49–56. <https://doi.org/10.1016/j.electacta.2013.01.140>.
- (177) Aranzaes, J. R.; Daniel, M.-C.; Astruc, D. Metallocenes as References for the Determination of Redox Potentials by Cyclic Voltammetry — Permethylated Iron and Cobalt Sandwich Complexes, Inhibition by Polyamine Dendrimers, and the Role of

- Hydroxy-Containing Ferrocenes. *Can. J. Chem.* **2006**, *84* (2), 288–299. <https://doi.org/10.1139/v05-262>.
- (178) Bao, D.; Millare, B.; Xia, W.; Steyer, B. G.; Gerasimenko, A. A.; Ferreira, A.; Contreras, A.; Vullev, V. I. Electrochemical Oxidation of Ferrocene: A Strong Dependence on the Concentration of the Supporting Electrolyte for Nonpolar Solvents. *J. Phys. Chem. A* **2009**, *113* (7), 1259–1267. <https://doi.org/10.1021/jp809105f>.
- (179) Chatterley, A. S.; Lackner, F.; Pemmaraju, C. D.; Neumark, D. M.; Leone, S. R.; Gessner, O. Dissociation Dynamics and Electronic Structures of Highly Excited Ferrocenium Ions Studied by Femtosecond XUV Absorption Spectroscopy. *J. Phys. Chem. A* **2016**, *120* (48), 9509–9518. <https://doi.org/10.1021/acs.jpca.6b09724>.
- (180) Flores-Leonar, M. M.; Moreno-Esparza, R.; Ugalde-Saldívar, V. M.; Amador-Bedolla, C. Further Insights in DFT Calculations of Redox Potential for Iron Complexes: The Ferrocenium/Ferrocene System. *Computational and Theoretical Chemistry* **2017**, *1099*, 167–173. <https://doi.org/10.1016/j.comptc.2016.11.023>.
- (181) Takano, Y.; Houk, K. N. Benchmarking the Conductor-like Polarizable Continuum Model (CPCM) for Aqueous Solvation Free Energies of Neutral and Ionic Organic Molecules. *J. Chem. Theory Comput.* **2005**, *1* (1), 70–77. <https://doi.org/10.1021/ct049977a>.
- (182) Frisch, M. J.; Trucks, G. W.; Schlegel, H. B.; Scuseria, G. E.; Robb, M. A.; Cheeseman, J. R.; Scalmani, G.; Barone, V.; Petersson, G. A.; Nakatsuji, H.; Li, X.; Caricato, M.; Marenich, A. V.; Bloino, J.; Janesko, B. G.; Gomperts, R.; Mennucci, B.; Hratchian, H. P.; Ortiz, J. V.; Izmaylov, A. F.; Sonnenberg, J. L.; Williams-Young, D.; Ding, F.; Lipparini, F.; Egidi, F.; Goings, J.; Peng, B.; Petrone, A.; Henderson, T.; Ranasinghe, D.; Zakrzewski, V. G.; Gao, J.; Rega, N.; Zheng, G.; Liang, W.; Hada, M.; Ehara, M.; Toyota, K.; Fukuda, R.; Hasegawa, J.; Ishida, M.; Nakajima, T.; Honda, Y.; Kitao, O.; Nakai, H.; Vreven, T.; Throssell, K.; Montgomery, J. A., Jr.; Peralta, J. E.; Ogliaro, F.; Bearpark, M. J.; Heyd, J. J.; Brothers, E. N.; Kudin, K. N.; Staroverov, V. N.; Keith, T. A.; Kobayashi, R.; Normand, J.; Raghavachari, K.; Rendell, A. P.; Burant, J. C.; Iyengar, S. S.; Tomasi, J.; Cossi, M.; Millam, J. M.; Klene, M.; Adamo, C.; Cammi, R.; Ochterski, J. W.; Martin, R. L.; Morokuma, K.; Farkas, O.; Foresman, J. B.; Fox, D. J. Gaussian<sup>16</sup> Revision C.01, 2016.
- (183) Klamt, A. Chapter 2 - Dielectric Continuum Solvation Models and COSMO. In *COSMO-RS*; Klamt, A., Ed.; Elsevier: Amsterdam, 2005; pp 11–41. <https://doi.org/10.1016/B978-044451994-8/50002-X>.
- (184) Klamt, A. Chapter 3 - Fundamental Criticism of the Dielectric Continuum Approach. In *COSMO-RS*; Klamt, A., Ed.; Elsevier: Amsterdam, 2005; pp 43–47. <https://doi.org/10.1016/B978-044451994-8/50003-1>.
- (185) Klamt, A. Chapter 4 - Molecular Interactions at the North Pole: A Virtual Experiment. In *COSMO-RS*; Klamt, A., Ed.; Elsevier: Amsterdam, 2005; pp 49–58. <https://doi.org/10.1016/B978-044451994-8/50004-3>.
- (186) Klamt, A. Chapter 5 - Statistical Thermodynamics of Interacting Surfaces. In *COSMO-RS*; Klamt, A., Ed.; Elsevier: Amsterdam, 2005; pp 59–81. <https://doi.org/10.1016/B978-044451994-8/50005-5>.
- (187) Klamt, A. Chapter 6 - The Basic COSMO-RS. In *COSMO-RS*; Klamt, A., Ed.; Elsevier: Amsterdam, 2005; pp 83–107. <https://doi.org/10.1016/B978-044451994-8/50006-7>.
- (188) Klamt, A. Chapter 7 - Refinements, Parameterization, and the Complete COSMO-RS. In *COSMO-RS*; Klamt, A., Ed.; Elsevier: Amsterdam, 2005; pp 109–125. <https://doi.org/10.1016/B978-044451994-8/50007-9>.

- (189) Klamt, A. Chapter 8 - COSMO-RS for Chemical Engineering Thermodynamics. In *COSMO-RS*; Klamt, A., Ed.; Elsevier: Amsterdam, 2005; pp 127–136. <https://doi.org/10.1016/B978-044451994-8/50008-0>.
- (190) Klamt, A. Chapter 9 - The  $\sigma$ -Moment Approach. In *COSMO-RS*; Klamt, A., Ed.; Elsevier: Amsterdam, 2005; pp 137–147. <https://doi.org/10.1016/B978-044451994-8/50009-2>.
- (191) Klamt, A. Chapter 10 - The Wider Range of COSMO-RS Applicability. In *COSMO-RS*; Klamt, A., Ed.; Elsevier: Amsterdam, 2005; pp 149–165. <https://doi.org/10.1016/B978-044451994-8/50010-9>.
- (192) Klamt, A. Chapter 11 - Life Science Applications of COSMO-RS. In *COSMO-RS*; Klamt, A., Ed.; Elsevier: Amsterdam, 2005; pp 167–203. <https://doi.org/10.1016/B978-044451994-8/50011-0>.
- (193) Liang, G.; DeYonker, N. J.; Zhao, X.; Webster, C. E. Prediction of the Reduction Potential in Transition-Metal Containing Complexes: How Expensive? For What Accuracy? *Journal of Computational Chemistry* **2017**, *38* (28), 2430–2438. <https://doi.org/10.1002/jcc.24894>.
- (194) Blöchl, P. E. Projector Augmented-Wave Method. *Phys Rev B Condens Matter* **1994**, *50* (24), 17953–17979. <https://doi.org/10.1103/physrevb.50.17953>.
- (195) Kresse, G.; Joubert, D. From Ultrasoft Pseudopotentials to the Projector Augmented-Wave Method. *Phys. Rev. B* **1999**, *59*, 1758. <https://doi.org/10.1103/PhysRevB.59.1758>.
- (196) Kresse, G.; Hafner, J. Ab Initio Molecular Dynamics for Liquid Metals. *Phys. Rev. B* **1993**, *47* (1), 558–561. <https://doi.org/10.1103/PhysRevB.47.558>.
- (197) Letchworth-Weaver, K.; Arias, T. A. Joint Density Functional Theory of the Electrode-Electrolyte Interface: Application to Fixed Electrode Potentials, Interfacial Capacitances, and Potentials of Zero Charge. *Phys. Rev. B* **2012**, *86* (7), 075140. <https://doi.org/10.1103/PhysRevB.86.075140>.
- (198) Gunceler, D.; Letchworth-Weaver, K.; Sundararaman, R.; Schwarz, K. A.; Arias, T. A. The Importance of Nonlinear Fluid Response in Joint Density-Functional Theory Studies of Battery Systems. *Modelling Simul. Mater. Sci. Eng.* **2013**, *21* (7), 074005. <https://doi.org/10.1088/0965-0393/21/7/074005>.
- (199) Mathew, K.; Sundararaman, R.; Letchworth-Weaver, K.; Arias, T. A.; Hennig, R. G. Implicit Solvation Model for Density-Functional Study of Nanocrystal Surfaces and Reaction Pathways. *The Journal of Chemical Physics* **2014**, *140* (8), 084106. <https://doi.org/10.1063/1.4865107>.
- (200) Mathew, K.; Kolluru, V. S. C.; Mula, S.; Steinmann, S. N.; Hennig, R. G. Implicit Self-Consistent Electrolyte Model in Plane-Wave Density-Functional Theory. *The Journal of Chemical Physics* **2019**, *151* (23), 234101. <https://doi.org/10.1063/1.5132354>.
- (201) Steinmann, S. N.; Sautet, P. Assessing a First-Principles Model of an Electrochemical Interface by Comparison with Experiment. *J. Phys. Chem. C* **2016**, *120* (10), 5619–5623. <https://doi.org/10.1021/acs.jpcc.6b01938>.
- (202) Isse, A. A.; Gennaro, A. Absolute Potential of the Standard Hydrogen Electrode and the Problem of Interconversion of Potentials in Different Solvents. *J. Phys. Chem. B* **2010**, *114* (23), 7894–7899. <https://doi.org/10.1021/jp100402x>.
- (203) Granda-Marulanda, L. P.; McCrum, I. T.; Koper, M. T. M. A Simple Method to Calculate Solution-Phase Free Energies of Charged Species in Computational Electrocatalysis. *J. Phys.: Condens. Matter* **2021**, *33* (20), 204001. <https://doi.org/10.1088/1361-648X/abf19d>.
- (204) Busch, M.; Ahlberg, E.; Laasonen, K. From Absolute Potentials to a Generalized Computational Standard Hydrogen Electrode for Aqueous and Non-Aqueous Solvents.

- Physical Chemistry Chemical Physics* **2021**, 23 (20), 11727–11737. <https://doi.org/10.1039/D1CP00499A>.
- (205) Matsui, T.; Kitagawa, Y.; Okumura, M.; Shigeta, Y.; Sakaki, S. Consistent Scheme for Computing Standard Hydrogen Electrode and Redox Potentials. *Journal of Computational Chemistry* **2013**, 34 (1), 21–26. <https://doi.org/10.1002/jcc.23100>.
- (206) Lavagnini, I.; Antiochia, R.; Magno, F. An Extended Method for the Practical Evaluation of the Standard Rate Constant from Cyclic Voltammetric Data. *Electroanalysis* **2004**, 16 (6), 505–506. <https://doi.org/10.1002/elan.200302851>.
- (207) Islam, S.; Wang, F. A Comparative Study of Energetics of Ferrocenium and Ferrocene. Preprints August 8, 2018. <https://doi.org/10.20944/preprints201808.0166.v1>.
- (208) Huang, J.; Zhang, J.; Eikerling, M. Unifying Theoretical Framework for Deciphering the Oxygen Reduction Reaction on Platinum. *Phys. Chem. Chem. Phys.* **2018**, 20 (17), 11776–11786. <https://doi.org/10.1039/C8CP01315B>.
- (209) Zhang, Y.; Zhang, J.; Huang, J. Potential-Dependent Volcano Plot for Oxygen Reduction: Mathematical Origin and Implications for Catalyst Design. *J. Phys. Chem. Lett.* **2019**, 10 (22), 7037–7043. <https://doi.org/10.1021/acs.jpclett.9b02436>.
- (210) Kant, R.; Mishra, G. K. Theory for Heterogeneous Electron Transfer Kinetics on Nanocorrugated Atomic Stepped Metal Electrodes. *J. Phys. Chem. C* **2023**, 127 (14), 6884–6899. <https://doi.org/10.1021/acs.jpcc.2c08690>.
- (211) Isse, A. A.; Gennaro, A. Electrocatalytic Carboxylation of Benzyl Chlorides at Silver Cathodes in Acetonitrile. *Chem. Commun.* **2002**, No. 23, 2798–2799. <https://doi.org/10.1039/B206746C>.
- (212) Isse, A. A.; De Giusti, A.; Gennaro, A.; Falciola, L.; Mussini, P. R. Electrochemical Reduction of Benzyl Halides at a Silver Electrode. *Electrochimica Acta* **2006**, 51 (23), 4956–4964. <https://doi.org/10.1016/j.electacta.2006.01.039>.
- (213) Yao, H.; Wang, M.-Y.; Yue, C.; Feng, B.; Ji, W.; Qian, C.; Wang, S.; Zhang, S.; Ma, X. Electrocarboxylation of CO<sub>2</sub> with Organic Substrates: Toward Cathodic Reaction. *Trans. Tianjin Univ.* **2023**, 29 (4), 254–274. <https://doi.org/10.1007/s12209-023-00361-2>.
- (214) Kramarenko, A. S.; Sharapa, D. I.; Pidko, E. A.; Studt, F. Ab Initio Kinetics of Electrochemical Reactions Using the Computational Fc<sup>0</sup>/Fc<sup>+</sup> Electrode. *J. Phys. Chem. A* **2024**. <https://doi.org/10.1021/acs.jpca.4c04923>.
- (215) Yamanaka, S.; Kawakami, T.; Nagao, H.; Yamaguchi, K. Effective Exchange Integrals for Open-Shell Species by Density Functional Methods. *Chemical Physics Letters* **1994**, 231 (1), 25–33. [https://doi.org/10.1016/0009-2614\(94\)01221-0](https://doi.org/10.1016/0009-2614(94)01221-0).
- (216) Song, J.-W.; Hirose, T.; Tsuneda, T.; Hirao, K. Long-Range Corrected Density Functional Calculations of Chemical Reactions: Redetermination of Parameter. *The Journal of Chemical Physics* **2007**, 126 (15), 154105. <https://doi.org/10.1063/1.2721532>.
- (217) Biot, C.; Taramelli, D.; Forfar-Bares, I.; Maciejewski, L. A.; Boyce, M.; Nowogrocki, G.; Brocard, J. S.; Basilico, N.; Oliaro, P.; Egan, T. J. Insights into the Mechanism of Action of Ferroquine. Relationship between Physicochemical Properties and Antiplasmodial Activity. *Mol. Pharmaceutics* **2005**, 2 (3), 185–193. <https://doi.org/10.1021/mp0500061>.
- (218) Menon, A. S.; Radom, L. Consequences of Spin Contamination in Unrestricted Calculations on Open-Shell Species: Effect of Hartree–Fock and Møller–Plesset Contributions in Hybrid and Double-Hybrid Density Functional Theory Approaches. *J. Phys. Chem. A* **2008**, 112 (50), 13225–13230. <https://doi.org/10.1021/jp803064k>.
- (219) Kim, K.; Jordan, K. D. Comparison of Density Functional and MP2 Calculations on the Water Monomer and Dimer. *J. Phys. Chem.* **1994**, 98 (40), 10089–10094. <https://doi.org/10.1021/j100091a024>.

- (220) Schiller, C.; Sieh, D.; Lindenmaier, N.; Stephan, M.; Junker, N.; Reijerse, E.; Granovsky, A. A.; Burger, P. Cleavage of an Aromatic C–C Bond in Ferrocene by Insertion of an Iridium Nitrido Nitrogen Atom. *J. Am. Chem. Soc.* **2023**, *145* (20), 11392–11401. <https://doi.org/10.1021/jacs.3c02781>.
- (221) Wang, X.; Chai, J.; Devi, N.; Lashgari, A.; Chaturvedi, A.; Jiang, J. “Jimmy.” Two-Electron-Active Tetracyanoethylene for Nonaqueous Redox Flow Batteries. *J. Mater. Chem. A* **2021**, *9* (24), 13867–13873. <https://doi.org/10.1039/D1TA01365C>.
- (222) Daub, N.; Hendriks, K. H.; Janssen, R. A. J. Two-Electron Tetrathiafulvalene Catholytes for Nonaqueous Redox Flow Batteries. *Batteries & Supercaps* **2022**, *5* (12), e202200386. <https://doi.org/10.1002/batt.202200386>.
- (223) Astudillo Sánchez, P. D.; Evans, D. H. Effect of Hydroxylic Additives on the Electrochemical Reduction of Some Azobenzenes. *Journal of Electroanalytical Chemistry* **2010**, *638* (1), 84–90. <https://doi.org/10.1016/j.jelechem.2009.10.016>.
- (224) Chicas-Baños, D. F.; López-Rivas, M.; González-Bravo, F. J.; Sartillo-Piscil, F.; Frontana-Urbe, B. A. Access to Carbonyl Compounds *via* the Electroreduction of *N*-Benzyloxypthalimides: Mechanism Confirmation and Preparative Applications. *Heliyon* **2024**, *10* (1), e23808. <https://doi.org/10.1016/j.heliyon.2023.e23808>.
- (225) Atifi, A.; Ryan, M. D. Voltammetry and Spectroelectrochemistry of TCNQ in Acetonitrile/RTIL Mixtures. *Molecules* **2020**, *25* (2), 303. <https://doi.org/10.3390/molecules25020303>.
- (226) Harris, A. R.; Neufeld, A. K.; O’Mullane, A. P.; Bond, A. M.; Morrison, R. J. S. Voltammetric, EQCM, Spectroscopic, and Microscopic Studies on the Electrocrystallization of Semiconducting, Phase I, CuTCNQ on Carbon, Gold, and Platinum Electrodes by a Nucleation-Growth Process. *J. Electrochem. Soc.* **2005**, *152* (9), C577. <https://doi.org/10.1149/1.1955047>.
- (227) Saiki, H.; Takami, K.; Tominaga, T. Diffusion of Porphyrins and Quinones in Organic Solvents. *Phys. Chem. Chem. Phys.* **1999**, *1* (2), 303–306. <https://doi.org/10.1039/A807920J>.
- (228) Mathieu-Scheers, E.; Bouden, S.; Grillot, C.; Nicolle, J.; Warmont, F.; Bertagna, V.; Cagnon, B.; Vautrin-UI, C. Trace Anthracene Electrochemical Detection Based on Electropolymerized-Molecularly Imprinted Polypyrrole Modified Glassy Carbon Electrode. *Journal of Electroanalytical Chemistry* **2019**, *848*, 113253. <https://doi.org/10.1016/j.jelechem.2019.113253>.
- (229) Ohba, T.; Ishida, H.; Yamaguchi, T.; Horiuchi, T.; Ohkubo, K. Carbon Dioxide-Promoted Electrochemical Reduction of Aromatic Nitro Compounds to Azoxy Compounds in Acetonitrile. *J. Chem. Soc., Chem. Commun.* **1994**, No. 3, 263–264. <https://doi.org/10.1039/C39940000263>.
- (230) Tsierkezos, N. G. Investigation of the Electrochemical Reduction of Benzophenone in Aprotic Solvents Using the Method of Cyclic Voltammetry. *J. Solution Chem* **2007**, *36* (10), 1301–1310. <https://doi.org/10.1007/s10953-007-9188-4>.
- (231) Astudillo, P. D.; Valencia, D. P.; González-Fuentes, M. A.; Díaz-Sánchez, B. R.; Frontana, C.; González, F. J. Electrochemical and Chemical Formation of a Low-Barrier Proton Transfer Complex between the Quinone Dianion and Hydroquinone. *Electrochimica Acta* **2012**, *81*, 197–204. <https://doi.org/10.1016/j.electacta.2012.07.078>.
- (232) Fawcett, W. R.; Fedurco, M. Medium Effects in the Electroreduction of Benzophenone in Aprotic Solvents. *J. Phys. Chem.* **1993**, *97* (27), 7075–7080. <https://doi.org/10.1021/j100129a025>.
- (233) Vasudevan, D.; Wendt, H. Electroreduction of Oxygen in Aprotic Media. *Journal of Electroanalytical Chemistry* **1995**, *392* (1), 69–74. [https://doi.org/10.1016/0022-0728\(95\)04044-O](https://doi.org/10.1016/0022-0728(95)04044-O).

- (234) Batanero, B.; Sánchez-Sánchez, C. M.; Montiel, V.; Aldaz, A.; Barba, F. Electrochemical Synthesis of 3-Phenylcinnamionitrile by Reduction of Benzophenone in Acetonitrile. *Electrochemistry Communications* **2003**, *5* (4), 349–353. [https://doi.org/10.1016/S1388-2481\(03\)00066-3](https://doi.org/10.1016/S1388-2481(03)00066-3).
- (235) Mailu, S. N.; Waryo, T. T.; Ndagili, P. M.; Ngece, F. R.; Baleg, A. A.; Baker, P. G.; Iwuoha, E. I. Determination of Anthracene on Ag-Au Alloy Nanoparticles/Overoxidized-Polypyrrole Composite Modified Glassy Carbon Electrodes. *Sensors* **2010**, *10* (10), 9449–9465. <https://doi.org/10.3390/s101009449>.
- (236) Neukermans, S.; Hereijgers, J.; Vincent Ching, H. Y.; Samanipour, M.; Van Doorslaer, S.; Hubin, A.; Breugelmans, T. A Continuous In-Situ EPR Electrochemical Reactor as a Rapid in-Depth Mechanistic Screening Tool for Electrocatalysis. *Electrochemistry Communications* **2018**, *97*, 42–45. <https://doi.org/10.1016/j.elecom.2018.10.010>.
- (237) Chiyindiko, E.; Conradie, J. An Electrochemical and Computational Chemistry Study of Substituted Benzophenones. *Electrochimica Acta* **2021**, *373*, 137894. <https://doi.org/10.1016/j.electacta.2021.137894>.
- (238) Rees, N. V.; Clegg, A. D.; Klymenko, O. V.; Coles, B. A.; Compton, R. G. Marcus Theory for Outer-Sphere Heterogeneous Electron Transfer: Predicting Electron-Transfer Rates for Quinones. *J. Phys. Chem. B* **2004**, *108* (34), 13047–13051. <https://doi.org/10.1021/jp040382l>.
- (239) Andrieux, C. P.; Le Gorande, A.; Saveant, J. M. Electron Transfer and Bond Breaking. Examples of Passage from a Sequential to a Concerted Mechanism in the Electrochemical Reductive Cleavage of Arylmethyl Halides. *J. Am. Chem. Soc.* **1992**, *114* (17), 6892–6904. <https://doi.org/10.1021/ja00043a039>.
- (240) Parson, W. W. Reorganization Energies, Entropies, and Free Energy Surfaces for Electron Transfer. *J. Phys. Chem. B* **2021**, *125* (29), 7940–7945. <https://doi.org/10.1021/acs.jpcc.1c01932>.
- (241) Kodis, G.; Ertem, M. Z.; Newton, M. D.; Matyushov, D. V. Reorganization Energy of Electron Transfer in Ionic Liquids. *J. Phys. Chem. Lett.* **2022**, *13* (14), 3297–3303. <https://doi.org/10.1021/acs.jpclett.2c00733>.
- (242) Rajan, A. G.; Carter, E. A. Microkinetic Model for pH- and Potential-Dependent Oxygen Evolution during Water Splitting on Fe-Doped  $\beta$ -NiOOH. *Energy Environ. Sci.* **2020**, *13* (12), 4962–4976. <https://doi.org/10.1039/D0EE02292F>.
- (243) Zhang, L.; Huang, J. Understanding Surface Charge Effects in Electrocatalysis. Part I: Peroxodisulfate Reduction at Pt(111). *J. Phys. Chem. C* **2020**, *124* (31), 16951–16960. <https://doi.org/10.1021/acs.jpcc.0c02824>.
- (244) Gosser, D. K. *Cyclic Voltammetry: Simulation and Analysis of Reaction Mechanisms*; VCH, 1993.
- (245) Lehmann, K.; Yurchenko, O.; Urban, G. Carbon Nanowalls for Oxygen Reduction Reaction in Bio Fuel Cells. *J. Phys.: Conf. Ser.* **2014**, *557* (1), 012008. <https://doi.org/10.1088/1742-6596/557/1/012008>.
- (246) Palacios-Ramírez, J. I.; González, F. J. Revisiting the Electrochemical Reduction Mechanism of Nitrosobenzene in Acetonitrile. Concomitant Reactions and Voltammetric Simulation. *ChemElectroChem* **2024**, *11* (3), e202300486. <https://doi.org/10.1002/celec.202300486>.
- (247) Masnovi, J. M.; Seddon, E. A.; Kochi, J. K. Electron Transfer from Anthracenes. Comparison of Photoionization, Charge-Transfer Excitation and Electrochemical Oxidation. *Can. J. Chem.* **1984**, *62* (11), 2552–2559. <https://doi.org/10.1139/v84-436>.
- (248) Sioda, R. E. Electrolytic Oxidation of 9,10-Diphenylanthracene and Properties of Its Free Radical Cation and Anion. *J. Phys. Chem.* **1968**, *72* (7), 2322–2330. <https://doi.org/10.1021/j100853a007>.



- (249) Kotani, H.; Ohkubo, K.; Fukuzumi, S. Photocatalytic Oxygenation of Anthracenes and Olefins with Dioxygen via Selective Radical Coupling Using 9-Mesityl-10-Methylacridinium Ion as an Effective Electron-Transfer Photocatalyst. *J. Am. Chem. Soc.* **2004**, *126* (49), 15999–16006. <https://doi.org/10.1021/ja048353b>.
- (250) Niu, D.-F.; Xiao, L.-P.; Zhang, A.-J.; Zhang, G.-R.; Tan, Q.-Y.; Lu, J.-X. Electrocatalytic Carboxylation of Aliphatic Halides at Silver Cathode in Acetonitrile. *Tetrahedron* **2008**, *64* (46), 10517–10520. <https://doi.org/10.1016/j.tet.2008.08.093>.
- (251) Wu, L.-X.; Deng, F.-J.; Wu, L.; Wang, H.; Chen, T.; Guan, Y.-B.; Lu, J.-X. Nickel-Catalyzed Electrocarboxylation of Allylic Halides with CO<sub>2</sub>. *New J. Chem.* **2021**, *45* (29), 13137–13141. <https://doi.org/10.1039/D1NJ02006D>.
- (252) Sun, G.-Q.; Zhang, W.; Liao, L.-L.; Li, L.; Nie, Z.-H.; Wu, J.-G.; Zhang, Z.; Yu, D.-G. Nickel-Catalyzed Electrochemical Carboxylation of Unactivated Aryl and Alkyl Halides with CO<sub>2</sub>. *Nat Commun* **2021**, *12* (1), 7086. <https://doi.org/10.1038/s41467-021-27437-8>.
- (253) Bazzi, S.; Schulz, E.; Mellah, M. Electrogenated Sm(II)-Catalyzed CO<sub>2</sub> Activation for Carboxylation of Benzyl Halides. *Org. Lett.* **2019**, *21* (24), 10033–10037. <https://doi.org/10.1021/acs.orglett.9b03927>.
- (254) Anandhakumar, S.; Sripriya, R.; Chandrasekaran, M.; Govindu, S.; Noel, M. Electrocarboxylation and Related Radical Coupling Processes of Aryl and Benzyl Halides in Microemulsion. *J Appl Electrochem* **2009**, *39* (3), 463–465. <https://doi.org/10.1007/s10800-008-9692-2>.
- (255) Mazin, V. M.; Mysov, E. I.; Sterlin, S. R.; Grinberg, V. A. Electrocarboxylation of  $\alpha,\omega$ -Dihaloperfluoroalkanes and of Perfluoroalkylhalides in a near-Critical and Supercritical CO<sub>2</sub>-Methanol Medium. *Journal of Fluorine Chemistry* **1998**, *88* (1), 29–35. [https://doi.org/10.1016/S0022-1139\(97\)00131-0](https://doi.org/10.1016/S0022-1139(97)00131-0).
- (256) Wang, H.-M.; Sui, G.-J.; Wu, D.; Feng, Q.; Wang, H.; Lu, J.-X. Selective Electrocarboxylation of Bromostyrene at Silver Cathode in DMF. *Tetrahedron* **2016**, *72* (7), 968–972. <https://doi.org/10.1016/j.tet.2015.12.066>.
- (257) Santiago, S.; Richart, C.; Mena, S.; Gallardo, I.; Hernando, J.; Guirado, G. Electrocarboxylation of Spiropyran Switches through Carbon-Bromide Bond Cleavage Reaction. *ChemElectroChem* **2022**, *9* (8), e202101559. <https://doi.org/10.1002/celec.202101559>.
- (258) Savéant, J.-M. Dissociative Electron Transfer and the Principle of Microscopic Reversibility. *Journal of Electroanalytical Chemistry* **2000**, *485* (1), 86–88. [https://doi.org/10.1016/S0022-0728\(00\)00078-4](https://doi.org/10.1016/S0022-0728(00)00078-4).
- (259) Cukier, R. I. A Theory for the Rate Constant of a Dissociative Proton-Coupled Electron-Transfer Reaction. *J. Phys. Chem. A* **1999**, *103* (30), 5989–5995. <https://doi.org/10.1021/jp990329a>.
- (260) Antonello, S.; Formaggio, F.; Moretto, A.; Toniolo, C.; Maran, F. Intramolecular, Intermolecular, and Heterogeneous Nonadiabatic Dissociative Electron Transfer to Peresters. *J. Am. Chem. Soc.* **2001**, *123* (39), 9577–9584. <https://doi.org/10.1021/ja010799u>.
- (261) Bass, A. D.; Sanche, L. Dissociative Electron Attachment and Charge Transfer in Condensed Matter. *Radiation Physics and Chemistry* **2003**, *68* (1), 3–13. [https://doi.org/10.1016/S0969-806X\(03\)00244-5](https://doi.org/10.1016/S0969-806X(03)00244-5).
- (262) Stringle, D. L. B.; Campbell, R. N.; Workentin, M. S. Radical Anion Chain Process Initiated by a Dissociative Electron Transfer to a Monocyclic Endoperoxide. *Chem. Commun.* **2003**, No. 11, 1246–1247. <https://doi.org/10.1039/B301909H>.

- (263) Zhou, Z. Y.; Xing, Y. M. Kinetics of Dissociative Electron Transfer for Homogeneous and Heterogeneous Reductive Bond-Breaking Reactions. *Journal of Molecular Structure: THEOCHEM* **2000**, 532 (1), 87–93. [https://doi.org/10.1016/S0166-1280\(00\)00504-2](https://doi.org/10.1016/S0166-1280(00)00504-2).
- (264) Kuznetsov, A. M.; German, E. D.; Masliy, A. N.; Korshin, G. V. A Density Functional Study of Dissociative Electron Transfer Reactions with Participation of Halogenated Methanes. *Journal of Electroanalytical Chemistry* **2004**, 573 (2), 315–325. <https://doi.org/10.1016/j.jelechem.2004.07.018>.
- (265) Uozumi, Y.; Hattori, S. Electrocarboxylation of Aryl Bromide with CO<sub>2</sub> by Bifunctional Cu/Ag Catalysts. *Synfacts* **2023**, 19, 1238. <https://doi.org/10.1055/s-0043-1763585>.
- (266) Olloqui-Sariego, J. L.; Molina, V. M.; González-Arjona, D.; Roldán, E.; Domínguez, M. Electrolytic Synthesis of Chloroacetic Acids in a Filter-Press Reactor from Polychloromethanes. *Electrochemistry Communications* **2010**, 12 (7), 952–954. <https://doi.org/10.1016/j.elecom.2010.04.030>.
- (267) Zhang, K.; Liu, X.-F.; Zhang, W.-Z.; Ren, W.-M.; Lu, X.-B. Electrocarboxylation of N-Acylimines with Carbon Dioxide: Access to Substituted  $\alpha$ -Amino Acids. *Org. Lett.* **2022**, 24 (19), 3565–3569. <https://doi.org/10.1021/acs.orglett.2c01267>.
- (268) Wang, Y.; Tang, S.; Yang, G.; Wang, S.; Ma, D.; Qiu, Y. Electrocarboxylation of Aryl Epoxides with CO<sub>2</sub> for the Facile and Selective Synthesis of  $\beta$ -Hydroxy Acids. *Angewandte Chemie International Edition* **2022**, 61 (38), e202207746. <https://doi.org/10.1002/anie.202207746>.
- (269) Singh, K.; Sohal, H. S.; Singh, B. Synthesis of  $\alpha$ -Hydroxycarboxylic Acids from Various Aldehydes and Ketones by Direct Electrocarboxylation: A Facile, Efficient and Atom Economy Protocol. *ajc* **2021**, 33 (4), 839–845. <https://doi.org/10.14233/ajchem.2021.23090>.
- (270) Zhao, S.-F.; Wang, H.; Lan, Y.-C.; Liu, X.; Lu, J.-X.; Zhang, J. Influences of the Operative Parameters and the Nature of the Substrate on the Electrocarboxylation of Benzophenones. *Journal of Electroanalytical Chemistry* **2012**, 664, 105–110. <https://doi.org/10.1016/j.jelechem.2011.11.001>.
- (271) Li, C.; Yuan, G.; Jiang, H. Electrocarboxylation of Alkynes with Carbon Dioxide in the Presence of Metal Salt Catalysts. *Chinese Journal of Chemistry* **2010**, 28 (9), 1685–1689. <https://doi.org/10.1002/cjoc.201090285>.
- (272) Bandeira, M. C. E.; Maia, G. Electrocarboxylation of 2-Methylhalogen-9,10-Anthraquinones. *Electrochimica Acta* **2008**, 53 (13), 4512–4519. <https://doi.org/10.1016/j.electacta.2008.01.019>.
- (273) Wang, H.; Zhang, G.; Liu, Y.; Luo, Y.; Lu, J. Electrocarboxylation of Activated Olefins in Ionic Liquid BMIMBF<sub>4</sub>. *Electrochemistry Communications* **2007**, 9 (9), 2235–2239. <https://doi.org/10.1016/j.elecom.2007.06.031>.
- (274) Lin, C. Y.; Coote, M. L.; Gennaro, A.; Matyjaszewski, K. Ab Initio Evaluation of the Thermodynamic and Electrochemical Properties of Alkyl Halides and Radicals and Their Mechanistic Implications for Atom Transfer Radical Polymerization. *J. Am. Chem. Soc.* **2008**, 130 (38), 12762–12774. <https://doi.org/10.1021/ja8038823>.
- (275) Isse, A. A.; Lin, C. Y.; Coote, M. L.; Gennaro, A. Estimation of Standard Reduction Potentials of Halogen Atoms and Alkyl Halides. *J. Phys. Chem. B* **2011**, 115 (4), 678–684. <https://doi.org/10.1021/jp109613t>.
- (276) Andrieux, C. P.; Blocman, C.; Savéant, J. M. Characterization of Electrochemical Reactions Hidden in the Background Discharge the Redox Catalyzed Reduction of Fluorobenzene. *Journal of Electroanalytical Chemistry and Interfacial Electrochemistry* **1979**, 105 (2), 413–417. [https://doi.org/10.1016/S0022-0728\(79\)80139-4](https://doi.org/10.1016/S0022-0728(79)80139-4).

- (277) Costentin, C.; Robert, M.; Savéant, J.-M. Stepwise and Concerted Electron-Transfer/Bond Breaking Reactions. Solvent Control of the Existence of Unstable Pi Ion Radicals and of the Activation Barriers of Their Heterolytic Cleavage. *J Am Chem Soc* **2004**, *126* (51), 16834–16840. <https://doi.org/10.1021/ja045294t>.
- (278) Costentin, C.; Robert, M.; Savéant, J.-M. Fragmentation of Aryl Halide Pi Anion Radicals. Bending of the Cleaving Bond and Activation vs Driving Force Relationships. *J Am Chem Soc* **2004**, *126* (49), 16051–16057. <https://doi.org/10.1021/ja045989u>.
- (279) Yang, D.-T.; Zhu, M.; Schiffer, Z. J.; Williams, K.; Song, X.; Liu, X.; Manthiram, K. Direct Electrochemical Carboxylation of Benzylic C–N Bonds with Carbon Dioxide. *ACS Catal.* **2019**, *9* (5), 4699–4705. <https://doi.org/10.1021/acscatal.9b00818>.
- (280) Muchez, L.; De Vos, D. E.; Kim, M. Sacrificial Anode-Free Electrosynthesis of  $\alpha$ -Hydroxy Acids via Electrocatalytic Coupling of Carbon Dioxide to Aromatic Alcohols. *ACS Sustainable Chem. Eng.* **2019**, *7* (19), 15860–15864. <https://doi.org/10.1021/acssuschemeng.9b04612>.
- (281) Senboku, H.; Nagakura, K.; Fukuhara, T.; Hara, S. Three-Component Coupling Reaction of Benzylic Halides, Carbon Dioxide, and N,N-Dimethylformamide by Using Paired Electrolysis: Sacrificial Anode-Free Efficient Electrochemical Carboxylation of Benzylic Halides. *Tetrahedron* **2015**, *71* (23), 3850–3856. <https://doi.org/10.1016/j.tet.2015.04.020>.
- (282) Sen Gupta, S. K. Proton Transfer Reactions in Apolar Aprotic Solvents. *Journal of Physical Organic Chemistry* **2016**, *29* (5), 251–264. <https://doi.org/10.1002/poc.3524>.
- (283) Ji, C.; Peters, D. G. Electrochemical Reduction of Benzyl Iodide, Benzal Bromide, and Benzal Chlorobromide at Carbon Cathodes in the Presence of Nitric Oxide in Acetonitrile. *Journal of Electroanalytical Chemistry* **2001**, *516* (1), 39–49. [https://doi.org/10.1016/S0022-0728\(01\)00650-7](https://doi.org/10.1016/S0022-0728(01)00650-7).
- (284) Sinha, V.; Khramenkova, E.; Pidko, E. A. Solvent-Mediated Outer-Sphere CO<sub>2</sub> Electro-Reduction Mechanism over the Ag<sub>111</sub> Surface. *Chem. Sci.* **2022**, *13* (13), 3803–3808. <https://doi.org/10.1039/D1SC07119J>.
- (285) Rybkin, V. V. Mechanism of Aqueous Carbon Dioxide Reduction by the Solvated Electron. *J. Phys. Chem. B* **2020**, *124* (46), 10435–10441. <https://doi.org/10.1021/acs.jpcc.0c07859>.
- (286) Wu, J. Understanding the Electric Double-Layer Structure, Capacitance, and Charging Dynamics. *Chem. Rev.* **2022**, *122* (12), 10821–10859. <https://doi.org/10.1021/acs.chemrev.2c00097>.
- (287) Favaro, M.; Jeong, B.; Ross, P. N.; Yano, J.; Hussain, Z.; Liu, Z.; Crumlin, E. J. Unravelling the Electrochemical Double Layer by Direct Probing of the Solid/Liquid Interface. *Nat Commun* **2016**, *7* (1), 12695. <https://doi.org/10.1038/ncomms12695>.
- (288) Levey, K. J.; Edwards, M. A.; White, H. S.; Macpherson, J. V. Simulation of the Cyclic Voltammetric Response of an Outer-Sphere Redox Species with Inclusion of Electrical Double Layer Structure and Ohmic Potential Drop. *Phys. Chem. Chem. Phys.* **2023**, *25* (11), 7832–7846. <https://doi.org/10.1039/D3CP00098B>.
- (289) Moraes, C. V.; Kelly, R. G. A Comparison of FEM Results from the Use of Different Governing Equations in a Galvanic Cell Part II: Impact of Low Supporting Electrolyte Concentration. *Electrochimica Acta* **2023**, *468*, 143153. <https://doi.org/10.1016/j.electacta.2023.143153>.
- (290) Veloso, W. B.; Paixão, T. R. L. C.; Meloni, G. N. 3D Printed Electrodes Design and Voltammetric Response. *Electrochimica Acta* **2023**, *449*, 142166. <https://doi.org/10.1016/j.electacta.2023.142166>.
- (291) Liu, T.; Carneiro-Neto, E. B.; Pereira, E.; Taylor, J. E.; Fletcher, P. J.; Marken, F. Paired Electrosynthesis at Interdigitated Microband Electrodes: Exploring Diffusion and

- Reaction Zones in the Absence of a Supporting Electrolyte. *ACS Meas. Sci. Au* **2024**. <https://doi.org/10.1021/acsmeasuresciau.4c00009>.
- (292) Pendergast, A. D.; Levey, K. J.; Macpherson, J. V.; Edwards, M. A.; White, H. S. Electric Potential-Driven Acid/Base Chemistry: Kinetics of Electrochemical Interfacial Proton Transfer and Transport. *J. Phys. Chem. C* **2024**, *128* (17), 7127–7136. <https://doi.org/10.1021/acs.jpcc.4c01114>.
- (293) Blinder, S. M.; Nordman, C. E. Collision Theory of Chemical Reactions. *J. Chem. Educ.* **1974**, *51* (12), 790. <https://doi.org/10.1021/ed051p790>.
- (294) Grampp, G.; Mureşanu, C.; Landgraf, S. Photomodulated Voltammetry Investigations on the Benzyl Radical. *Electrochimica Acta* **2008**, *53* (7), 3149–3155. <https://doi.org/10.1016/j.electacta.2007.11.012>.
- (295) Huang, J.; Chen, S. Interplay between Covalent and Noncovalent Interactions in Electrocatalysis. *J. Phys. Chem. C* **2018**, *122* (47), 26910–26921. <https://doi.org/10.1021/acs.jpcc.8b07534>.
- (296) Sha, M.; Dou, Q.; Luo, F.; Zhu, G.; Wu, G. Molecular Insights into the Electric Double Layers of Ionic Liquids on Au(100) Electrodes. *ACS Appl. Mater. Interfaces* **2014**, *6* (15), 12556–12565. <https://doi.org/10.1021/am502413m>.
- (297) Feng, G.; Huang, J.; Sumpter, B. G.; Meunier, V.; Qiao, R. Structure and Dynamics of Electrical Double Layers in Organic Electrolytes. *Phys. Chem. Chem. Phys.* **2010**, *12* (20), 5468–5479. <https://doi.org/10.1039/C000451K>.
- (298) Shin, S.-J.; Kim, D. H.; Bae, G.; Ringe, S.; Choi, H.; Lim, H.-K.; Choi, C. H.; Kim, H. On the Importance of the Electric Double Layer Structure in Aqueous Electrocatalysis. *Nat Commun* **2022**, *13* (1), 174. <https://doi.org/10.1038/s41467-021-27909-x>.
- (299) Hasan, M. M.; Islam, T.; Shah, S. S.; Aziz, Md. A.; Awal, A.; Hossain, Md. D.; Ehsan, M. A.; Ahammad, A. J. S. Supporting Electrolyte Interaction with the AACVD Synthesized Rh Thin Film Influences the OER Activity. *International Journal of Hydrogen Energy* **2022**, *47* (67), 28740–28751. <https://doi.org/10.1016/j.ijhydene.2022.06.212>.
- (300) Bao, D.; Millare, B.; Xia, W.; Steyer, B. G.; Gerasimenko, A. A.; Ferreira, A.; Contreras, A.; Vullev, V. I. Electrochemical Oxidation of Ferrocene: A Strong Dependence on the Concentration of the Supporting Electrolyte for Nonpolar Solvents. *J. Phys. Chem. A* **2009**, *113* (7), 1259–1267. <https://doi.org/10.1021/jp809105f>.
- (301) Zhu, X.; Huang, J. Modeling Electrocatalytic Oxidation of Formic Acid at Platinum. *J. Electrochem. Soc.* **2019**, *167* (1), 013515. <https://doi.org/10.1149/2.0152001JES>.
- (302) Huang, J.; Eikerling, M. Modeling the Oxygen Reduction Reaction at Platinum-Based Catalysts: A Brief Review of Recent Developments. *Current Opinion in Electrochemistry* **2019**, *13*, 157–165. <https://doi.org/10.1016/j.coelec.2019.01.004>.
- (303) Ringe, S.; Clark, E. L.; Resasco, J.; Walton, A.; Seger, B.; Bell, A. T.; Chan, K. Understanding Cation Effects in Electrochemical CO<sub>2</sub> Reduction. *Energy Environ. Sci.* **2019**, *12* (10), 3001–3014. <https://doi.org/10.1039/C9EE01341E>.
- (304) Chen, L. D.; Urushihara, M.; Chan, K.; Nørskov, J. K. Electric Field Effects in Electrochemical CO<sub>2</sub> Reduction. *ACS Catal.* **2016**, *6* (10), 7133–7139. <https://doi.org/10.1021/acscatal.6b02299>.
- (305) Deng, B.; Huang, M.; Zhao, X.; Mou, S.; Dong, F. Interfacial Electrolyte Effects on Electrocatalytic CO<sub>2</sub> Reduction. *ACS Catal.* **2022**, *12* (1), 331–362. <https://doi.org/10.1021/acscatal.1c03501>.
- (306) Isse, A. A.; Arnaboldi, S.; Durante, C.; Gennaro, A. Reprint of “Electrochemical Reduction of Organic Bromides in 1-Butyl-3-Methylimidazolium Tetrafluoroborate.” *Journal of Electroanalytical Chemistry* **2018**, *819*, 562–569. <https://doi.org/10.1016/j.jelechem.2018.05.002>.

- (307) Bao, D.; Ramu, S.; Contreras, A.; Upadhyayula, S.; Vasquez, J. M.; Beran, G.; Vullev, V. I. Electrochemical Reduction of Quinones: Interfacing Experiment and Theory for Defining Effective Radii of Redox Moieties. *J. Phys. Chem. B* **2010**, *114* (45), 14467–14479. <https://doi.org/10.1021/jp101730e>.
- (308) Guo, R.; Georganopoulou, D.; Feldberg, S. W.; Donkers, R.; Murray, R. W. Supporting Electrolyte and Solvent Effects on Single-Electron Double Layer Capacitance Charging of Hexanethiolate-Coated Au140 Nanoparticles. *Anal. Chem.* **2005**, *77* (8), 2662–2669. <https://doi.org/10.1021/ac048218h>.
- (309) Han, X.; Ke, J.; Suleiman, N.; Levason, W.; Pugh, D.; Zhang, W.; Reid, G.; Licence, P.; George, M. W. Phase Behaviour and Conductivity of Supporting Electrolytes in Supercritical Difluoromethane and 1,1-Difluoroethane. *Phys. Chem. Chem. Phys.* **2016**, *18* (21), 14359–14369. <https://doi.org/10.1039/C6CP00466K>.
- (310) Collinson, M. M.; Higgins, D. A.; Kommidi, R.; Campbell-Rance, D. Electrodeposited Silicate Films: Importance of Supporting Electrolyte. *Anal. Chem.* **2008**, *80* (3), 651–656. <https://doi.org/10.1021/ac7017124>.
- (311) O'Mari, O.; Vullev, V. I. Optical Window to Polarity of Electrolyte Solutions. *Molecules* **2023**, *28* (11), 4360. <https://doi.org/10.3390/molecules28114360>.
- (312) Winkler, K.; de Bettencourt-Dias, A.; Balch, A. L. Charging Processes in Electroactive C60/Pd Films: Effect of Solvent and Supporting Electrolyte. *Chem. Mater.* **1999**, *11* (8), 2265–2273. <https://doi.org/10.1021/cm990227x>.
- (313) Szymanska, J.; Palys, M. J.; Van den Bossche, B. Neutral Reagents in Solutions with Low Content of Supporting Electrolyte: How To Determine the Steady-State Conditions. *Anal. Chem.* **2004**, *76* (19), 5937–5944. <https://doi.org/10.1021/ac049515p>.
- (314) Schley, L.; Vibhu, V.; Nohl, L.; Vinke, I. C.; de Haart, L. G. J. (Bert); Eichel, R.-A. A Highly Stable Pr<sub>2</sub>NiO<sub>4</sub>+  $\delta$  Oxygen Electrode in Electrolyte Supported Protonic Ceramic Electrolysis Cells (PCECs) for Hydrogen Production with High Faradaic Efficiency. *Energy Advances* **2024**, *3* (4), 861–873. <https://doi.org/10.1039/d3ya00542a>.
- (315) Lee, W.; In Shim, K.; Park, G.; Han, J. W.; Kwon, Y. Rational Design of Composite Supporting Electrolyte Required for Achieving High Performance Aqueous Organic Redox Flow Battery. *Chemical Engineering Journal* **2023**, *464*, 142661. <https://doi.org/10.1016/j.cej.2023.142661>.
- (316) Forster, R. J.; Walsh, D. A.; Mano, N.; Mao, F.; Heller, A. Modulating the Redox Properties of an Osmium-Containing Metallopolymer through the Supporting Electrolyte and Cross-Linking. *Langmuir* **2004**, *20* (3), 862–868. <https://doi.org/10.1021/la035229h>.
- (317) Cassady, H. J.; Rochow, M. F.; Hickner, M. A. Describing the Permeability of Permanganate Co-Ions in a CEM with Varying Supporting Electrolyte Concentrations. *Journal of Membrane Science* **2024**, *694*, 122381. <https://doi.org/10.1016/j.memsci.2023.122381>.
- (318) Zhao, Y.; Chen, X.; Tu, S.; Zhang, X.; Zhang, S.; Zhang, H.; Zhang, X.; Chen, L. Electro-Optical Performance of Solid-State Electrochromic Device Based on Self-Supporting Electrolyte. *Optical Materials* **2024**, *149*, 114991. <https://doi.org/10.1016/j.optmat.2024.114991>.
- (319) Zhang, W.; Guan, W.; Wang, Y.; Lin, S.; See, K. A. Enabling Al Sacrificial Anodes in Tetrahydrofuran Electrolytes for Reductive Electrosynthesis. *Chem. Sci.* **2023**, *14* (45), 13108–13118. <https://doi.org/10.1039/D3SC04725C>.
- (320) Yan, Y.; Sitaula, P.; Odom, S. A.; Vaid, T. P. High Energy Density, Asymmetric, Nonaqueous Redox Flow Batteries without a Supporting Electrolyte. *ACS Appl. Mater. Interfaces* **2022**, *14* (44), 49633–49640. <https://doi.org/10.1021/acsami.2c10072>.

- (321) Zhang, J.; Ying, H.; Zhang, Y.; Yao, J.; Li, H. Possibility of Using Ferrocene as the Cyclic Voltammetry Probe to Investigate the Polarities of Ionic Liquids. *J. Phys. Chem. B* **2023**, *127* (26), 5899–5904. <https://doi.org/10.1021/acs.jpcc.3c02630>.
- (322) Yun, J.; Lee, J. G.; Oh, K.; Kang, K.; Chung, T. D. Aqueous Ionic Effect on Electrochemical Breakdown of Si-Dielectric–Electrolyte Interface. *Sci Rep* **2020**, *10* (1), 16795. <https://doi.org/10.1038/s41598-020-73880-w>.
- (323) Cho, K.; Qu, Y.; Kwon, D.; Zhang, H.; Cid, C. A.; Aryanfar, A.; Hoffmann, M. R. Effects of Anodic Potential and Chloride Ion on Overall Reactivity in Electrochemical Reactors Designed for Solar-Powered Wastewater Treatment. *Environ. Sci. Technol.* **2014**, *48* (4), 2377–2384. <https://doi.org/10.1021/es404137u>.
- (324) R. Finney, A.; J. McPherson, I.; R. Unwin, P.; Salvalaglio, M. Electrochemistry, Ion Adsorption and Dynamics in the Double Layer: A Study of NaCl(Aq) on Graphite. *Chemical Science* **2021**, *12* (33), 11166–11180. <https://doi.org/10.1039/D1SC02289J>.
- (325) Peshkova, T. V.; Minkov, I. L.; Tsekov, R.; Slavchov, R. I. Adsorption of Ions at Uncharged Insoluble Monolayers. *Langmuir* **2016**, *32* (35), 8858–8871. <https://doi.org/10.1021/acs.langmuir.6b02349>.
- (326) Goldfarb, D. L.; Longinotti, M. P.; Corti, H. R. Electrical Conductances of Tetrabutylammonium and Decamethylferrocenium Hexafluorophosphate in Organic Solvents. *Journal of Solution Chemistry* **2001**, *30* (4), 307–322. <https://doi.org/10.1023/A:1010334021934>.
- (327) Hibbits, J. O.; Cooper, S. S. Polarographic Study of Lead in Potassium Thiocyanate Supporting Electrolyte. *Anal. Chem.* **1954**, *26* (7), 1119–1120. <https://doi.org/10.1021/ac60091a005>.
- (328) Kiessling, A.; Fornaciari, J. C.; Anderson, G.; Peng, X.; Gerstmayr, A.; Gerhardt, M.; McKinney, S.; Serov, A.; Weber, A. Z.; Kim, Y. S.; Zulevi, B.; Danilovic, N. Influence of Supporting Electrolyte on Hydroxide Exchange Membrane Water Electrolysis Performance: Catholyte. *J. Electrochem. Soc.* **2022**, *169* (2), 024510. <https://doi.org/10.1149/1945-7111/ac4fed>.
- (329) Lee, M.-Y.; Ringe, S.; Kim, H.; Kang, S.; Kwon, Y. Electric Field Mediated Selectivity Switching of Electrochemical CO<sub>2</sub> Reduction from Formate to CO on Carbon Supported Sn. *ACS Energy Lett.* **2020**, *5* (9), 2987–2994. <https://doi.org/10.1021/acsenenergylett.0c01387>.
- (330) Tang, W.; Zhao, S.; Huang, J. Origin of Solvent Dependency of the Potential of Zero Charge. *JACS Au* **2023**, *3* (12), 3381–3390. <https://doi.org/10.1021/jacsau.3c00552>.
- (331) Adesokan, B. J.; Quan, X.; Evgrafov, A.; Heiskanen, A.; Boisen, A.; Sørensen, M. P. Experimentation and Numerical Modeling of Cyclic Voltammetry for Electrochemical Micro-Sized Sensors under the Influence of Electrolyte Flow. *Journal of Electroanalytical Chemistry* **2016**, *763*, 141–148. <https://doi.org/10.1016/j.jelechem.2015.12.029>.
- (332) van Soestbergen, M. Diffuse Layer Effects on the Current in Galvanic Cells Containing Supporting Electrolyte. *Electrochimica Acta* **2010**, *55* (5), 1848–1854. <https://doi.org/10.1016/j.electacta.2009.10.078>.
- (333) Kaur, J.; Kant, R. Curvature-Induced Anomalous Enhancement in the Work Function of Nanostructures. *J. Phys. Chem. Lett.* **2015**, *6* (15), 2870–2874. <https://doi.org/10.1021/acs.jpcclett.5b01197>.
- (334) Huang, J. Density-Potential Functional Theory of Electrochemical Double Layers: Calibration on the Ag(111)-KPF<sub>6</sub> System and Parametric Analysis. *J. Chem. Theory Comput.* **2023**, *19* (3), 1003–1013. <https://doi.org/10.1021/acs.jctc.2c00799>.
- (335) Saxena, R. R.; Bragg, R. H. Electrical Conduction in Glassy Carbon. *Journal of Non-Crystalline Solids* **1978**, *28* (1), 45–60. [https://doi.org/10.1016/0022-3093\(78\)90073-X](https://doi.org/10.1016/0022-3093(78)90073-X).

- (336) Schueller, O. J. A.; Brittain, S. T.; Marzolin, C.; Whitesides, G. M. Fabrication and Characterization of Glassy Carbon MEMS. *Chem. Mater.* **1997**, *9* (6), 1399–1406. <https://doi.org/10.1021/cm960639v>.
- (337) Sohda, Y.; Tanenbaum, D. M.; Turner, S. W.; Craighead, H. G. Fabrication of Arrayed Glassy Carbon Field Emitters. *Journal of Vacuum Science & Technology B: Microelectronics and Nanometer Structures Processing, Measurement, and Phenomena* **1997**, *15* (2), 343–348. <https://doi.org/10.1116/1.589318>.
- (338) Glukhova, O. E.; Slepchenkov, M. M. Electronic Properties of the Functionalized Porous Glass-like Carbon. *J. Phys. Chem. C* **2016**, *120* (31), 17753–17758. <https://doi.org/10.1021/acs.jpcc.6b05058>.
- (339) Zebardast, H. R.; Rogak, S.; Asselin, E. Potential of Zero Charge of Glassy Carbon at Elevated Temperatures. *Journal of Electroanalytical Chemistry* **2014**, *724*, 36–42. <https://doi.org/10.1016/j.jelechem.2014.03.030>.
- (340) Tran, R.; Li, X.-G.; Montoya, J. H.; Winston, D.; Persson, K. A.; Ong, S. P. Anisotropic Work Function of Elemental Crystals. *Surface Science* **2019**, *687*, 48–55. <https://doi.org/10.1016/j.susc.2019.05.002>.
- (341) Tran, R.; Xu, Z.; Radhakrishnan, B.; Winston, D.; Sun, W.; Persson, K. A.; Ong, S. P. Surface Energies of Elemental Crystals. *Sci Data* **2016**, *3* (1), 160080. <https://doi.org/10.1038/sdata.2016.80>.
- (342) Zheng, H.; Li, X.-G.; Tran, R.; Chen, C.; Horton, M.; Winston, D.; Persson, K. A.; Ong, S. P. Grain Boundary Properties of Elemental Metals. *Acta Materialia* **2020**, *186*, 40–49. <https://doi.org/10.1016/j.actamat.2019.12.030>.
- (343) Hinsch, J. J.; White, J. J.; Wang, Y. Theoretical Investigation on Potential of Zero Free Charge of (111) and (100) Surfaces of Group 10 and 11 Metals. *Computational and Theoretical Chemistry* **2024**, *1232*, 114462. <https://doi.org/10.1016/j.comptc.2024.114462>.
- (344) Shatla, A. S.; Landstorfer, M.; Baltruschat, H. On the Differential Capacitance and Potential of Zero Charge of Au(111) in Some Aprotic Solvents. *ChemElectroChem* **2021**, *8* (10), 1817–1835. <https://doi.org/10.1002/celec.202100316>.
- (345) Ludwig, T.; Singh, A. R.; Nørskov, J. K. Acetonitrile Transition Metal Interfaces from First Principles. *J. Phys. Chem. Lett.* **2020**, *11* (22), 9802–9811. <https://doi.org/10.1021/acs.jpcllett.0c02692>.
- (346) Le, J.; Iannuzzi, M.; Cuesta, A.; Cheng, J. Determining Potentials of Zero Charge of Metal Electrodes versus the Standard Hydrogen Electrode from Density-Functional-Theory-Based Molecular Dynamics. *Phys. Rev. Lett.* **2017**, *119* (1), 016801. <https://doi.org/10.1103/PhysRevLett.119.016801>.
- (347) Chen, J.; Nie, L.; Yao, S. A New Method for Rapid Determination of the Potential of Zero Charge for Gold. *Journal of Electroanalytical Chemistry* **1996**, *414* (1), 53–59. [https://doi.org/10.1016/0022-0728\(96\)04646-3](https://doi.org/10.1016/0022-0728(96)04646-3).
- (348) Fröhlich, N. L.; Eggebeen, J. J. J.; Koper, M. T. M. Measurement of the Double-Layer Capacitance of Pt(111) in Acidic Conditions near the Potential of Zero Charge. *Electrochimica Acta* **2024**, *494*, 144456. <https://doi.org/10.1016/j.electacta.2024.144456>.
- (349) Álvarez, B.; Climent, V.; Rodes, A.; Feliu, J. M. Potential of Zero Total Charge of Palladium Modified Pt(111) Electrodes in Perchloric Acid Solutions. *Phys. Chem. Chem. Phys.* **2001**, *3* (16), 3269–3276. <https://doi.org/10.1039/B100482O>.
- (350) Ludwig, T.; Singh, A. R.; Nørskov, J. K. Nonaqueous Solvent Adsorption on Transition Metal Surfaces with Density Functional Theory: Interaction of N,N-Dimethylformamide (DMF), Tetrahydrofuran (THF), and Dimethyl Sulfoxide (DMSO) with Ag, Cu, Pt, Rh, and Re Surfaces. *J. Phys. Chem. C* **2021**, *125* (40), 21943–21957. <https://doi.org/10.1021/acs.jpcc.1c05724>.

- (351) Doubova, L. M.; Trasatti, S.; Valcher, S. Adsorption of Acetonitrile on Polycrystalline Ag Electrodes: Comparison with Hg Electrodes. *Journal of Electroanalytical Chemistry* **1993**, 349 (1), 187–195. [https://doi.org/10.1016/0022-0728\(93\)80172-E](https://doi.org/10.1016/0022-0728(93)80172-E).
- (352) Łukomska, A.; Sobkowski, J. Potential of Zero Charge of Monocrystalline Copper Electrodes in Perchlorate Solutions. *Journal of Electroanalytical Chemistry* **2004**, 567 (1), 95–102. <https://doi.org/10.1016/j.jelechem.2003.11.063>.
- (353) Gritzner, G. Polarographic Half-Wave Potentials of Cations in Nonaqueous Solvents. *Pure and Applied Chemistry* **1990**, 62 (9), 1839–1858. <https://doi.org/10.1351/pac199062091839>.
- (354) Abeed, F. A.; Al-Allaf, T. A. K.; Sulaiman, S. T. Electroanalytical Studies of Ferrocene and Substituted Ferrocene in Non-Aqueous Solvents by Rotating Disc Voltammetry. *Analyst* **1988**, 113 (2), 333–336. <https://doi.org/10.1039/AN9881300333>.
- (355) Bond, A. M.; Oldham, K. B.; Snook, G. A. Use of the Ferrocene Oxidation Process To Provide Both Reference Electrode Potential Calibration and a Simple Measurement (via Semiintegration) of the Uncompensated Resistance in Cyclic Voltammetric Studies in High-Resistance Organic Solvents. *Anal. Chem.* **2000**, 72 (15), 3492–3496. <https://doi.org/10.1021/ac000020j>.
- (356) Bond, A. M.; McLennan, E. A.; Stojanovic, R. S.; Thomas, F. G. Assessment of Conditions under Which the Oxidation of Ferrocene Can Be Used as a Standard Voltammetric Reference Process in Aqueous Media. *Anal. Chem.* **1987**, 59 (24), 2853–2860. <https://doi.org/10.1021/ac00151a007>.
- (357) Oldham, K. B. Steady-State Voltammetry at a Rotating Disk Electrode in the Absence of Supporting Electrolyte. *J. Phys. Chem. B* **2000**, 104 (19), 4703–4706. <https://doi.org/10.1021/jp994442c>.
- (358) Mayther, M. F.; O'Mari, O.; Flacke, P.; Bhatt, D.; Andrews, S.; Vullev, V. I. How Do Liquid-Junction Potentials and Medium Polarity at Electrode Surfaces Affect Electrochemical Analyses for Charge-Transfer Systems? *J. Phys. Chem. B* **2023**, 127 (6), 1443–1458. <https://doi.org/10.1021/acs.jpcc.2c07983>.
- (359) Benjamin, I.; Kharkats, Yu. I. Reorganization Free Energy for Electron Transfer Reactions at Liquid/Liquid Interfaces. *Electrochimica Acta* **1998**, 44 (1), 133–138. [https://doi.org/10.1016/S0013-4686\(98\)00161-3](https://doi.org/10.1016/S0013-4686(98)00161-3).
- (360) Wang, J.; Ma, J.; Li, X.; He, F.; Fu, K. Solvent Reorganization Energy and Electronic Coupling for Intramolecular Electron Transfer in Biphenyl-Acceptor Anion Radicals. *Chinese Journal of Chemical Physics* **2008**, 21 (1), 45–54. <https://doi.org/10.1088/1674-0068/21/01/45-54>.
- (361) Gupta, S.; Matyushov, D. V. Effects of Solvent and Solute Polarizability on the Reorganization Energy of Electron Transfer. *J. Phys. Chem. A* **2004**, 108 (11), 2087–2096. <https://doi.org/10.1021/jp036388c>.
- (362) Janisch, J.; Klinkhammer, R.; Ruff, A.; Schäfer, J.; Speiser, B.; Wolff, C. Two-Electron-Transfer Redox Systems. Part 8. Proving the Electron Stoichiometry for the Electrochemical Two-Electron Oxidation of *N,N'*-Bis(Ferrocenoyl)-1,2-Diaminoethane. *Electrochimica Acta* **2013**, 110, 608–618. <https://doi.org/10.1016/j.electacta.2013.05.036>.
- (363) Konishi, H.; Takekawa, R.; Minato, T.; Ogumi, Z.; Abe, T. Interactions among Solvent, Anion Acceptor, and Supporting Electrolyte Salt in Fluoride Shuttle Battery Electrolyte Based on Nuclear Magnetic Resonance. *Energy Storage* **2022**, 4 (6), e403. <https://doi.org/10.1002/est2.403>.
- (364) Caram, J. A.; Suárez, J. F. M.; Gennaro, A. M.; Mirífico, M. V. ELECTROCHEMICAL BEHAVIOUR OF METHYLENE BLUE IN NON-AQUEOUS SOLVENTS.



- Electrochimica Acta* **2015**, *164*, 353–363.  
<https://doi.org/10.1016/j.electacta.2015.01.196>.
- (365) Bezruchko, M. M.; Tsventarnyi, E. G.; Malev, V. V. Effect of the Supporting-Electrolyte Cation on the Chloroplatinite Ion Reduction at a Dropping Mercury Electrode. *Russian Journal of Electrochemistry* **2001**, *37* (11), 1189–1196.  
<https://doi.org/10.1023/A:1012719716782>.
- (366) Ivanov, V. D.; Alieva, A. R. Electrochemical Behavior of Electrode Modified with a Cobalt Hexacyanoferrate Film: Effect of the Supporting Electrolyte Cation. *Russ J Electrochem* **2000**, *36* (8), 852–860. <https://doi.org/10.1007/BF02757058>.
- (367) Yue, G.; Zeng, Q.; Huang, J.; Wang, L. Mechanism Studies of Hydrazine Electro-Oxidation by a Platinum Ultramicroelectrode: Effects of Supporting Electrolytes. *Journal of Electroanalytical Chemistry* **2018**, *818*, 19–25.  
<https://doi.org/10.1016/j.jelechem.2018.04.012>.